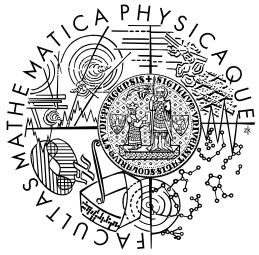

FACULTY
OF MATHEMATICS
AND PHYSICS
Charles University

MASTER THESIS

Lenka Kubíčková

Relaxivity of magnetic iron oxide nanoparticles containing diamagnetic cations

Department of Low-Temperature Physics

Supervisor of the master thesis:	doc. Mgr. Jaroslav Kohout, Dr.
Study programme:	Physics
Study branch:	Physics of Condensed Matter and Materials

Prague 2017

I declare that I carried out this master thesis independently, and only with the cited sources, literature and other professional sources.

I understand that my work relates to the rights and obligations under the Act No. 121/2000 Sb., the Copyright Act, as amended, in particular the fact that the Charles University has the right to conclude a license agreement on the use of this work as a school work pursuant to Section 60 subsection 1 of the Copyright Act.

In Prague, 9 May 2017

Title: Relaxivity of magnetic iron oxide nanoparticles containing diamagnetic cations

Author: Lenka Kubíčková

Department: Department of Low-Temperature Physics

Supervisor: doc. Mgr. Jaroslav Kohout, Dr., Department of Low-Temperature Physics

Abstract: Magnetic nanoparticles have received extensive attention in the biomedical research, e.g. as prospective contrast agents for T_2-weighted magnetic resonance imaging. The ability of a contrast agent to enhance the relaxation rate of ^{1}H in its vicinity is quantified by relaxivity. The main aim of this thesis is to evaluate the transversal relaxivity of ε-$Fe_{2-x}Al_xO_3$ nanoparticles coated with amorphous silica or citrate — its dependence on external magnetic field, temperature and thickness of silica coating — by means of nuclear magnetic resonance. The aluminium content $x = 0.23(1)$ was determined from XRF, the material was further characterised by XRPD, Mössbauer spectroscopy, DLS, TEM and magnetic measurements. The size of magnetic cores was $\sim$ 21 nm, the thickness of silica coating $\sim 6, 10, 17$ and 21 nm. Magnetization of the ε-$Fe_{2-x}Al_xO_3$ nanoparticles increased by $\sim$ 30 % when compared to ε-Fe_2O_3. The saturating dependence of relaxivity on external magnetic field and on the linear decrease with increase of thickness of silica coating contravene the theoretical model of motional averaging regime (MAR); nevertheless, the temperature dependence acquired in 0.47 T and 11.75 T may be explained by MAR. In comparison to ε-Fe_2O_3 nanoparticles, the relaxivity of examined samples was higher for particles with silica coating thinner than 10 nm; no considerable difference in relaxivity for thicker coatings is in contradiction to the prediction of MAR. The relaxivity was comparable to commercial superparamagnetic iron oxide contrast agents. The thesis provides experimental data still rare in the literature, showing thus the shortcomings of theoretical models of relaxivity available at present. Very low cytotoxicity enables the future use of examined nanoparticles for *in vivo* studies and prospectively in human medicine.

Keywords: relaxometry, spin-spin relaxation time, magnetocrystalline anisotropy, log-normal distribution, iron(III) oxide, cell viability

I would like to express my gratitude to my supervisor doc. Mgr. Jaroslav Kohout, Dr. for his patient guidance and willingness to devote his time to me. I would also like to thank Ing. Mgr. Ondřej Kaman, Ph.D. from the Institute of Physics of the Czech Academy of Sciences (FZÚ AV ČR) for his kind assistance, valuable practical advices, help during measurements and his readiness to answer my questions at any hour, to Mgr. Vít Herynek, Ph.D. from the Institute for Clinical and Experimental Medicine for his help with experiments on MRI tomoghraphs and for providing data from the cytotoxicity study, to Mgr. Tomáš Kmječ for initiating me into XRF and providing me with the XRF data, and to Mgr. Petr Dvořák for teaching me how to operate the NMR spectrometer. Apart from Ing. Mgr. Ondřej Kaman, Ph.D., I would like to acknowledge also Mgr. Petr Brázda, Ph.D. and Ing. Pavel Veverka, Ph.D. from FZÚ ČR for synthesis and coating of the nanoparticles. I am indebted to RNDr. Karel Závěta, CSc. for his conscientious reading-through the manuscript and providing valuable comments. I would like to thank to Martin for useful discussions on the formal aspects of the thesis and his willingness to offer his support if needed. Last but not least, my deepest thanks belong to my loving family who are there for me, always...

Contents

Introduction

Magnetic nanoparticles have been in focus of material research for decades due to their unique properties significantly different from the bulk material. One of the main fields of interest represent their potential applications in medicine enhancing particular diagnostic and therapeutic methods, especially in cancer treatment. The cutting-edge is to join both diagnostic and therapeutic functions in one object, a so called theranostic tool particularly eligible to detect and kill tumour cells. Magnetic nanoparticles provide suitable carriers for therapeutic drugs since they can be easily manipulated by external magnetic field. Moreover, they can simultaneously act as an imaging probe.

Magnetic resonance imaging (MRI) is one of the leading non-invasive imaging techniques both in clinical praxis and in research. The contrast in MRI is generated by the difference in proton density and the T_1 and $T_2^{(*)}$ relaxation times of tissues. In order to achieve local enhancement in contrast and hereby in the resolution, magnetic nanoparticles can be employed as appropriate contrast agents, reducing the relaxation times of ^{1}H in the surrounding tissue. To assess the efficacy of a contrast agent, the concept of relaxivity as a quantity characterising the ability of the contrast agent to increase the relaxation rates of surrounding ^{1}H was introduced.

The main aim of this thesis it to evaluate the relaxivity of ε-$Fe_{2-x}Al_xO_3$ nanoparticles coated with amorphous silica. This material was chosen as a follow-up of my bachelor thesis dealing with the relaxivity of ε-Fe_2O_3 nanoparticles. Since ε-Fe_2O_3 is a ferrimagnetic material, our idea was to substitute a diamagnetic cation — aluminium in this case — for a fraction of iron cations. We assumed that the Al atoms would preferentially occupy tetrahedral sites, which partially compensate the magnetic moment of the other sites, then the substitution would result in the increase of the overall magnetic moment of the nanoparticles and hereby in enhancement of their relaxivity, as predicted by the theory. Therefore, we aimed also at verifying this assumption.

Outline

This thesis is obliquely divided into two sections: the theoretical background (first three chapters) and the experimental part (last two chapters). Chapter 1 overviews the most common synthesis methods of nanoparticles along with some of the magnetic properties emerging at nanoscale. Chapter 2 provides a brief introduction to Nuclear magnetic resonance and MRI methods and the relaxation mechanisms. Furthermore, it summarises the theory of relaxivity including the most recent theoretical models. Chapter 3 outlines the properties of ε-Fe_2O_3 as an initial material for this study. Experimental details and techniques are described in chapter 4, while experimental results on the characterisation of the material and its relaxivity along with the discussion are summarised in chapter 5.

1. Magnetic nanoparticles

The term magnetic nanoparticles (MNPs) usually refers to materials responding to an applied magnetic field with the dimensions typically 1–100 nm, i.e. they contain from several hundreds to 10^5 atoms. Not only are MNPs prepared artificially but they can be also found worldwide in nature — in rocks, living organisms, even in the interstellar space — and intrinsically embedded in the cultural heritage of the mankind (Sattler, 2011a). Due to their unique properties different from the bulk materials, MNPs have been in focus of the material research for decades. They have found broad applications in biomedicine as theranostic agents in cancer treatment, or in industry e.g. as constituents of magnetic fluids (ferrofluids), permanent magnets, catalysts, gas sensors, toners for xenography, storage media or pollutant-removal agents (Huber, 2005; Stanicki et al., 2015; Laurent et al., 2008).

The extraordinary phenomena observed in a system of nanoparticles (NPs) arise from the delicate interplay among the intrinsic properties, finite-size effects, size distribution of the NPs and the interparticle interactions (Batlle and Labarta, 2002). As the size of NPs decreases, the surface-to-volume ratio increases along with the importance of both surface and finite-size effects. When discussing the influence of the size reduction on magnetic properties of nanomaterials, it is necessary to distinguish whether one considers *intrinsic* or *extrinsic* properties. *Intrinsic* properties, e.g. the saturation magnetization M_s, the anisotropy or the exchange stiffness A, are established on the atomic scale and therefore tend to approach their bulk values within the length of a few interatomic distances. In contrast, *extrinsic* properties as the remanent magnetization M_r or coercivity H_c (the hysteresis effects) are nonequilibrium phenomena and depend on the state of the system as a whole (Skomski, 2003).

In this chapter, a brief overview of selected preparation methods of MNPs is given, and specific magnetic properties arising from reduced size are discussed in more detail.

1.1 Synthesis of magnetic nanoparticles

Many pathways to produce MNPs have been developed so far. However, meeting main requirements as a narrow size distribution of the system of NPs, their homogeneous composition, preventing the aggregation and also the possibility of industrialization of the process still remains challenging.

The methods of preparation of MNPs can be categorised into two types: *top-down* and *bottom-up*. The *top-down* approach relies on the reduction of bulk materials to the desired sizes and includes mechanical machining, laser beam and electron beam processing or photolithography. On the other hand, the *bottom-up* approach uses molecular reagents to build up nanosized structures. The bottom-up methods are usually preferred due to a better control over the shape and size distribution of prepared NPs (Stanicki et al., 2015). Among the most broadly used methods belong the sol-gel method, coprecipitation, thermal decomposition or gas phase preparation which are elaborated below. (Sattler, 2011a).

Sol-gel preparation

Sol-Gel reactions provide a convenient wet pathway to prepare metal oxide NPs (Feldmann and Jungk, 2001). This synthesis builds on the hydroxylation and condensation of precursors in solution, where a *sol* of nanosized particles is formed. As a result of further condensation and inorganic polymerization at room temperature, a wet *gel* composed of metal oxide network is created. This gel must be treated at elevated temperature in order to reach the desired level of crystallinity (Laurent et al., 2008).

Coprecipitation

The coprecipitation method is probably the simplest and the most efficient chemical route to prepare NPs (Laurent et al., 2008). It is widely used to produce oxides of magnetic 3d transition metals (e.g. γ-Fe_2O_3 or Fe_3O_4) from aqueous salt solutions under the inert atmosphere in the room temperature or higher. Typically, to prepare iron oxide NPs, an alkaline base (NaOH or NH_4OH) is added to a mixture of ferric and ferrous salts (Kim et al., 2001). The stability of the suspension is enhanced by introducing anionic surfactants as dispersive agents, or by coating the particles with various protective substances (Kim et al., 2003). The composition, size and shape of prepared MNPs result from the type of salt used (sulphates, chlorides, nitrates etc.), stoichiometry, pH value, reaction temperature, and the ionic strength of the media (Sattler, 2011a).

The coprecipitation process occurs in two phases: a short burst of nucleation, when the solution reaches a certain supersaturation value, and a subsequent slow growth of the nuclei by diffusion of the solutes to the surface of the crystal (LaMer and Dinegar, 1950). Monodisperse iron oxide suspensions can be obtained only by a strict separation of these two phases (Laurent et al., 2008). However, due to the rapid nucleation it is difficult to reach a well defined crystallinity in the samples.

Thermal decomposition

Small monodisperse MNPs can be synthesised through the thermal decomposition of organometallic compounds in organic solvents with high boiling temperature. Stabilizing surfactants as long hydrocarbon chains are used, enabling also the size and shape control (Dumestre et al., 2004). The reaction is performed either by warming a mixture of organometallic precursors and surfactants in the solvent, or by injecting the precursor into a hot solution of solvent and surfactants (a.k.a. *hot injection*; Stanicki et al., 2015). Because of the high temperature used during the synthesis process, it is possible to obtain well crystalline NPs.

Gas phase preparation

Gas phase preparation method is based on a condensation of a supersaturated vapour of the material in the inert gas environment (Gleiter, 1989). Particle nuclei are formed by a homogeneous nucleation process, and grow by successive aggregation. Modified ultra high vacuum (UHV) evaporation or sputtering systems are usually used, enabling preparation of metal NPs which do not suffer from oxidation.

With this method, systems with narrow size distribution can be produced, though only in small amounts (Sattler, 2011a).

1.2 Isolated magnetic nanoparticle

Magnetic properties of fine particles are strongly determined by the combination of finite-size effects, resulting from a cut-off of some characteristic length due to geometrical constraints of a finite volume, and surface effects, originating from the increase of the fraction of atoms at the surface of particles with reducing size. In reality, both kinds of effects are mixed and sometimes hardly distinguishable.

1.2.1 Finite-size effects

It is well known that magnetic bulk materials are composed of many domains with collinear spin structure separated by domain walls. This structure results from the balance of exchange, magnetostatic (or dipolar) and anisotropy energy. Although the magnetostatic energy endeavours to minimize the overall magnetization in the material, below a certain critical volume the energy cost to create domain walls is higher than the corresponding energy reduction. In that case, a **single domain state** is preferred. The critical radius R_c for e.g. spherical MNPs can be calculated from (Petracic, 2010)

$$R_c = \frac{36\sqrt{AK}}{\mu_0 M_s^2},$$

where A — the exchange stiffness — is a material constant related to the critical temperature of magnetic ordering, K is the anisotropy constant (see below), M_s the saturation magnetization of the particle, μ_0 the permeability of free space. Typical value of R_c ranges from 10 to 800 nm (Batlle and Labarta, 2002), being e.g. ~ 50 nm for Fe_3O_4 (Petracic, 2010). When trying to reverse the magnetization direction, for small NPs all atom spins tend to rotate simultaneously (*coherent rotation*). The NP can be thus described by one huge moment $\mathbf{m_{NP}}$ with similar behaviour as the atomic one, often referred to as a *superspin*. It is proportional to the NP volume and saturation magnetization $|\mathbf{m_{NP}}| \approx M_s V$, and reaches the order of $1000\,\mu_B$ (Petracic, 2010).

The direction of atomic moments (or the superspin) in relation to the crystal lattice is controlled by the **magnetocrystalline anisotropy**, which reflects the symmetry of the neighbours of each atom. Nonetheless, microscopic mechanisms leading to anisotropy can be diverse — apart from the *magnetocrystalline anisotropy* also the *stress anisotropy* caused by the inner stress in the sample, the *shape anisotropy* from the balance between demagnetising and external fields, or the *surface anisotropy* discussed later (Sattler, 2011a). The resulting anisotropy energy is a combination of all contributions present at the atom site. Therefore, it is usually considered uniaxial in this context and characterized by a single effective anisotropy constant K_{eff}. In the thermal equilibrium, the resulting magnetization of a single domain NP points in the direction minimizing the anisotropy energy of the particle, which is also called the *easy axis*. The **anisotropy energy** of a particle in zero external magnetic field can be thus expressed as

$$E(\theta) = K_{\text{eff}} V \sin^2\theta, \tag{1.1}$$

with θ being the angle between the magnetization direction and the easy axis, and $K_{\text{eff}}V$ the energy barrier between the magnetic orientational energy minima. The energy barrier (further labelled E_B to consider general case) can be overcome as a result of thermal excitations, and consequently, the magnetization can flip from one easy direction to another one. The dynamics of this process is characterised by the **Néel relaxation time** τ_N and sufficiently described by the *Néel-Brown model* based on the Arrhenius law

$$\tau_N = \tau_0 e^{\frac{E_B}{k_B T}}, \tag{1.2}$$

the prefactor τ_0 is of the order 10^{-13}–10^{-9} s (Sattler, 2011b) and generally depends on many parameters: the anisotropy energy, temperature, saturation magnetization etc. (Batlle and Labarta, 2002).

If the energy barrier is higher than the energy of thermal excitations ($E_B \gg k_B T$), the particle is in a **frozen state** and τ_N in the high anisotropy case can exceed centuries. Nevertheless, above certain temperature T_B, the thermal excitations become comparable to the E_B and induce rapid switching of the particle superspin when compared to the observation time t. From the experimental point of view, the particles are in a **superparamagnetic regime**, the temperature T_B is called the **blocking temperature** and characterises the temperature when the time scale of the experiment and superspin fluctuations match:

$$T_B = \frac{E_B}{k_B \ln \frac{t}{\tau_0}} \quad . \tag{1.3}$$

Consequently, whether we see the NP system in the frozen or superparamagnetic regime strongly depends on the type of experiment we employ — the time scale of SQUID magnetometry is typically 10–100 s, while in Mössbauer spectroscopy 10^{-9}–10^{-7} s (Papaefthymiou, 2009; Sattler, 2011a).

For small NPs in a colloidal suspension, another rotational mode is also important: brownian motion characterised by the **Brown relaxation time**

$$\tau_B = \frac{3V\eta}{k_B T}, \tag{1.4}$$

where η is the viscosity of the carrier medium. The total magnetic relaxation time derived from equations 1.2 and 1.4 is then

$$\frac{1}{\tau_{\text{eff}}} = \frac{1}{\tau_N} + \frac{1}{\tau_B}. \tag{1.5}$$

Both of these relaxation mechanisms directly affect not only the magnetization curves, but also two biomedical applications of MNPs — magnetic resonance imaging (MRI) and magnetic hyperthermia.

1.2.2 Surface effects

The origins of surface effects lie in the lack of translational symmetry at the boundaries of the particle resulting from the missing nearest neighbours of the surface atoms and the subsequent contraction of surface layers due to structure relaxation. As a consequence, the magnetic exchange bonds are broken, which leads to surface spin frustration and misalignment, often generating an approximate ferromagnetic

(FM) ordering of surface spins. It is the surface effects which dominate the magnetic properties of smallest NPs and cause the superspin approximation not to be valid any more (Batlle and Labarta, 2002).

The symmetry breaking at the boundaries of the particle along with the presence of vacancies and some degree of a structural disorder give rise to the **surface anisotropy**, which induces the increase of the particle anisotropy with its reducing size (Batlle and Labarta, 2002). An effective anisotropy per unit volume can be thus modelled by separate contributions of the bulk K_b and the surface K_s and following phenomenological expression can be used (Bødker et al., 1994)

$$K_{\text{eff,sph}} = K_b + \frac{S}{V} K_s \quad .$$

An interesting fact is that the surface effects can result in both increase and decrease in the magnetization of the NPs in certain cases. The magnetization of some metal oxide NPs was reported to decrease, and several scenarios were proposed: the existence of a magnetically dead layer at the surface, the existence of canted spins or the presence of a spin-glass-like behaviour of surface spins (Kodama, 1999). In contrast, the magnetization of some metallic NPs was observed to increase (Respaud et al., 1998).

For above mentioned reasons, the total magnetization can be considered consisting of two components — the contributions of core and surface spins, described by the **core-shell model**. In this model, the magnetically ordered state in the core is assumed, while a surface layer of canted spins undergoing a spin-glass-like transition to a frozen state at certain temperature T_F is expected in the shell (Martínez et al., 1998). The interaction occurring at the core-shell interface is called the *exchange bias* or *exchange coupling* and provides an additional magnetic anisotropy. In particles of antiferromagnetic (AFM) and ferrimagnetic (FIM) materials (as most metal oxides), the interaction appears between the AFM/FIM core and the FM surface. On the other hand, in some FM metallic NPs, the surface layer oxidises and the exchange bias occurs between the FM core and the AFM oxide shell (Issa et al., 2013). The presence of the exchange bias belongs to the leading factors increasing the coercivity of MNPs and also the external magnetic field that needs to be applied to achieve the saturation magnetization.

As the temperature increases, the magnetization of the surface decreases more rapidly than the one of the core, i.e. the surface spins are demagnetized by thermal excitations more easily (Herr et al., 1987). Moreover, it was found that owing to both surface and finite-size effects, the critical temperature when the spontaneous magnetization vanishes is reduced with the decrease in size of the NPs (Batlle and Labarta, 2002).

1.3 Ensembles of interacting nanoparticles

Firstly, it must be emphasised that when measuring any macroscopic property of a system of NPs, it is necessary to consider the size distribution of particles in the ensemble. For most cases (NPs growing in the presence of a significant drift and/or diffusion), the system follows the **log-normal distribution** (Kiss et al., 1999)

$$P(d) = \frac{1}{\sqrt{2\pi}\sigma d} e^{-\frac{\ln^2\left(\frac{d}{d_0}\right)}{2\sigma^2}}, \tag{1.6}$$

where d is the particle diameter and σ the standard deviation of $\ln d$. When magnetic interactions between particles in the system can be neglected, it is possible to treat the system as an assembly of randomly oriented particles with volume-dependent properties driven by the distribution 1.6. Nevertheless, in the case of non-negligible interactions, the behaviour of the ensemble is markedly complicated.

The main magnetic interaction present in the NP assemblies is the **dipole-dipole interaction**, which always exists and dominates for MNPs embedded in an insulating and diamagnetic matrix (SiO_2 or Al_2O_3, solvents of ferrofluids; Batlle and Labarta, 2002; Petracic, 2010).

In MNP ensembles, different magnetic behaviours may develop depending on the strength of the interaction. The types of behaviours can be classified according to the corresponding relaxation time τ (Dormann et al., 1997; Batlle and Labarta, 2002) as follows (sorted from the weakest to the strongest interactions):

- *superparamagnetism*
  NPs in the ensemble are independent, described by the Néel-Brown model 1.2
  $$\tau = \tau_0 e^{\frac{E_B}{k_B T}}.$$

- *modified superparamagnetism*
  Again, the NPs in the ensemble are independent, described by the Néel-Brown model; however, the energy barrier E_B is modified by the interparticle interactions
  $$\tau = \tau_0 e^{\frac{E_B^*}{k_B T}}.$$

- *glass-like freezing*
  As the interparticle interactions grow stronger, a *collective* behaviour occurs. In this case, one encounters a glass-like freezing of the superspins with a "glass temperature" T_0, yet it is not a true phase transition. The relaxation time is accordingly modified (Vogel-Fulcher law; Shtrikman and Wohlfarth, 1981):
  $$\tau = \tau_0 e^{\frac{E_B*}{k_B(T-T_0)}}.$$

- *superspin glass*
  For MNPs randomly arranged in space and even stronger interactions (especially when the interparticle distance reduced), the ensemble undergoes a phase transition into a superspin glass phase bellow the critical temperature T_g. Such MNP assemblies share some features with spin glasses, as the aging effect, memory or slow relaxation (Sasaki et al., 2005). The relaxation time is then given by a power law with the critical exponent $z\nu$, where ν is the critical exponent of the correlation length $\xi \propto \left[(T - T_g)/T_g\right]^{-\nu}$ and z connects the relaxation time and the correlation length $\tau \propto \xi^z$ (Ogielski, 1985)
  $$\tau = \tau_0^* \left(\frac{T - T_g}{T_g} \right)^{-z\nu}.$$

- *superferromagnetism*
  For MNPs regularly arranged in space and the dipolar interactions strong

enough, an analogue of ferromagnetic ordering for superspins can be generated

$$\tau = \tau_0^* \left(\frac{T - T_c}{T_c} \right)^{-z\nu} .$$

Nevertheless, it is difficult to distinguish the particular behaviour of an examined ensemble of NPs. A rough estimate can be made by a "successful" or "unsuccessful" fit of experimental data based on how reasonable the obtained parameters (e.g. critical temperature or τ_0) seem to be.

2. Relaxation induced by magnetic nanoparticles in MRI

This chapter is intended to provide a very brief introduction to the principles of nuclear magnetic resonance (NMR) and MRI, detailed information can be found elsewhere (e.g. Slichter, 1990; Brown et al., 2014) in order to deliver background for the main focus of the chapter, the introduction to relaxation mechanisms and relaxivities of magnetic nanoparticle contrast agents used in MRI.

2.1 Basic principles of NMR

The phenomenon of NMR results from nuclear spin dynamics under the influence of static and oscillating magnetic fields. For the purpose of this work only the nuclei with spin quantum number of $1/2$ will be considered. If the static magnetic field B_0 is applied on the spin, the energy difference between the two eigenstates corresponding to two projections $\pm\hbar/2$ of the angular momentum into the quantization axis defined by B_0 is

$$\Delta E = \hbar\gamma B_0 = \hbar\omega_0, \tag{2.1}$$

where $\hbar$ is the reduced Planck constant, γ the nuclear gyromagnetic ratio, which equals to 42.58 MHz.T^{-1} for the most widely used nucleus ^{1}H, and ω_0 the transition Larmor frequency. The ratio of population numbers of these two eigenstates reaches

$$\frac{N_1}{N_2} = e^{-\frac{\hbar\omega_0}{k_B T}} \tag{2.2}$$

at thermal equilibrium at temperature T. By applying a transversal oscillating magnetic field B_1 with frequency ω, the transitions between the eigenstates may be induced, with the probability of the system being at time t at its initial state described by Rabi formula

$$\mathscr{P}(t) = 1 - \frac{\omega_1^2}{\omega_1^2 + (\omega-\omega_0)^2}\sin^2\left(\frac{t}{2}\sqrt{\omega_1^2 + (\omega-\omega_0)^2}\right), \tag{2.3}$$

where ω_1 characterises the amplitude of the field B_1 and $\omega-\omega_0$ the detuning from resonance.

Nuclei with nonzero spin have their own magnetic moment $\boldsymbol{\mu_I} = \gamma \boldsymbol{I}$. For a macroscopic ensemble it is relevant to sum up the nuclei magnetic moments in a classical vector of magnetization density $\boldsymbol{M}$, which follows **Bloch's equation** Bloch (1946). When introducing the interspin interactions and diffusion into the Bloch's equation, one gets its complete form

$$\frac{d\boldsymbol{M}}{dt} = \gamma \boldsymbol{M} \times \boldsymbol{B}_{\text{eff}} - R_{1,2}\boldsymbol{M} - D\boldsymbol{\Delta M}. \tag{2.4}$$

When written in the rotating frame $(\hat{x}, \hat{y}, \hat{z})$ synchronised with the oscillating field, the effective field at the nucleus is given by

$$\boldsymbol{B}_{\text{eff}} = -\frac{\omega_1 \hat{x}}{\gamma} - \frac{\omega-\omega_0\hat{z}}{\gamma}. \tag{2.5}$$

The second term in equation 2.4 introduces the spin-lattice relaxation rate $R_1 = 1/T_1$ and the spin-spin relaxation rate $R_2 = 1/T_2$ for the longitudinal component M_z and for the transversal component $\boldsymbol{M}_\perp$ respectively. The last term reflects the irreversibility of diffusion described by the spin diffusion coefficient D. Both $\boldsymbol{B_0}$ and $\boldsymbol{B_1}$ are considered to be local fields affecting the nucleus in the studied system (Nacher, 2009).

2.2 Relaxation

When a pulse of an oscillating radiofrequency magnetic field is applied on the system, $\boldsymbol{M}$ simply rotates around the direction of the effective field, and at resonance rotation by any desired angle with respect to M_z can be achieved by a properly timed radiofrequency pulse (e.g. π or $\frac{\pi}{2}$ pulses). On the other hand, after the pulse when the system is exposed only to a uniform static field, spins precess around the direction of $\boldsymbol{B_0}$, the longitudinal magnetization exponentially recovers with a rate R_1 and the transversal component exponentially decays with a rate R_2. In a non-uniform field $\boldsymbol{B_0}$ the third term in 2.4 is pronounced leading to an additional decay of the transversal component $\boldsymbol{M}_\perp$ (Nacher, 2009).

2.2.1 Spin-lattice relaxation

After the excitation of the system of spins by a radiofrequency pulse, the magnetization M_z returns exponentially back to the Boltzmann equilibrium M_0 with time t

$$M_z = M_0\left(1 - e^{-\frac{t}{T_1}}\right). \tag{2.6}$$

The **longitudinal relaxation** is described by the longitudinal relaxation time T_1 or its inverse value, the longitudinal relaxation rate R_1.

Nuclear spins in the high energy state (antiparallel to the static magnetic field in the case of ^{1}H) can undergo transitions to a low energy state (parallel to the magnetic field) via spontaneous or stimulated emission of energy quanta. Since the probability of a spontaneous emission is very low, relaxation processes are dominated by emission stimulated by fluctuating local magnetic fields, which induce precession of protons at the Larmor frequency and originate in the intra- and intermolecular dipole-dipole interactions between nuclei of neighbouring molecules (lattice). For this reason, the longitudinal relaxation is also referred to as the **spin-lattice relaxation**. However, the dipolar field is significantly lower and can be thus treated as a small perturbation to the static magnetic field (e.g. for hydrogen nuclei the magnitude of a dipolar field at a distance 0.2 nm is $2{\cdot}10^{-4}$ T). For better understanding it is useful to define a classical scalar magnetic field $B_e(t)$ affecting the resonating nucleus and bearing information on random rotational and translational movements (Brownian motion). For large time scales there is no correlation of the movement; however, for shorter time scales the level of correlation with previous time points is high. To capture this behaviour, it is convenient to define the *autocorrelation function*

$$G(\tau) = \langle B_e(t), B_e(t+\tau)\rangle, \tag{2.7}$$

representing the mean time variation of the fluctuations of $B_e(t)$. For rotational and diffusional molecular motions it is usually well described by an exponential decay

with correlation time τ_c

$$G(\tau) = G(0)e^{-\frac{\tau}{\tau_c}}. \tag{2.8}$$

Considering that correlation times of various types of motions differ, the autocorrelation function can exhibit multi-exponential behaviour. Performing Fourier transformation on $G(\tau)$ we obtain the frequency distribution of the time variations in the effective field, i.e. the *spectral density function*

$$J(\omega, \tau_c) = \int_{-\infty}^{+\infty} G(\tau)e^{-i\omega t}\,\mathrm{d}\tau. \tag{2.9}$$

For the autocorrelation function given by equation 2.8 and the spectral density function normalized as $J(0, \tau_c) = \tau_c$, the Lorenzian distribution of angular frequencies can be derived

$$J(\omega, \tau_c) = \frac{\tau_c}{1 + (\omega\tau_c)^2}. \tag{2.10}$$

If we consider a system of two identical spins with four possible configurations in the external magnetic field, either one or both spins can change their own orientation from antiparallel to parallel by emission of an energy quantum of Larmor frequency ω_0 or $2\omega_0$, respectively. By a fully quantum-mechanical calculation of spin-lattice relaxation rate for dipolar interaction of two equal spins one can attain

$$R_1 = \frac{1}{T_1} = \frac{3\gamma^4\hbar^2\mu_0^2}{160\pi^2 r^6}\left(J(\omega_0, \tau_c) + 4J(2\omega_0, \tau_c)\right), \tag{2.11}$$

r being the distance between the two nuclei (Sattler, 2011b).

2.2.2 Spin-spin relaxation

After the rotation of nuclear magnetization to a transversal plane by a radiofrequency pulse, the spins are considered to precess coherently at Larmor frequency around the direction of static magnetic field. However, due to a modulation of local dipolar fields $B_e(t)$ in their surroundings the spins precess at slightly different Larmor frequencies, which results in their dephasing and exponential decay of the transversal component of magnetization

$$M_\perp = M_{\perp 0}e^{-\frac{t}{T2}}. \tag{2.12}$$

T_2 is the transversal relaxation time.

Contrary to the longitudinal relaxation, not only stimulated transitions are allowed, but also transitions keeping the energy of the system unchanged, i.e. when the two spins pointing in opposite direction swap their respective orientations. For this reason, the transversal relaxation depends on the spectral density function at $\omega = 0$ as well and is also referred to as the **spin-spin relaxation**. By the full quantum-mechanical derivation of transversal relaxation rate it can be shown that

$$R_2 = \frac{1}{T_2} = \frac{3\gamma^4\hbar^2\mu_0^2}{320\pi^2 r^6}\left(3J(0, \tau_c) + 5J(\omega_0, \tau_c) + 2J(2\omega_0, \tau_c)\right). \tag{2.13}$$

Nevertheless, the transversal relaxation rate can be further enhanced by inhomogeneities of macroscopic magnetic field (e.g. improper shimming of magnet coils or

differences in susceptibility between various tissues). The **accelerated transversal relaxation time** is denoted $\boldsymbol{T_2}^*$ and can be expressed as

$$\frac{1}{T_2^*} = \frac{1}{T_2} + \frac{1}{T_2'}, \tag{2.14}$$

where T_2 and T_2' stand for microscopic (dipolar) and macroscopic contributions, respectively (Sattler, 2011b).

Methods of measuring transversal relaxation time T_2

The detected decaying signal induced by $\boldsymbol{M}_\perp$ after the pulse applied on the system of spins is denoted as **free induction decay (FID)** and decreases with t as $\propto e^{\frac{t}{T_2^*}}$. When the FID fades away with dephasing of spins and if a π-pulse is applied at time t_e after the initiating pulse, spins are refocused at time $2t_e$ giving rise to the **spin echo**. The signal of spin echo takes the same form as FID; nevertheless, its intensity evolves following equation 2.12 and can be thus applied for measuring the T_2 relaxation time.

The study of the decaying intensity of spin echoes induced by a series of π-pulses after the initiating excitation $\frac{\pi}{2}$-pulse underlies the most extensively used methods for studying T_2: **Carr-Purcell** (Carr and Purcell, 1954) and the further enhanced **Carr-Purcell-Meiboom-Gill (CPMG)** (Meiboom and Gill, 1958). The difference between these two methods originates in the choice of the axis of spin rotation during the π-pulses. Let us assume that the spins are rotated by the $\frac{\pi}{2}$-pulse from the initial position parallel to z' to the $x'y'$ plane so that $\boldsymbol{M} \parallel y'$ (primes label the coordination system in the rotating reference frame). While the Carr-Purcell sequence employs π-pulses rotating around the y'-axis and cumulates thus errors caused by imprecise setting of pulses, the CPMG sequence rotates spins around the x'-axis and thereby eliminates the error from incorrect setting with every second pulse.

Another widely used method employed in MRI is the **gradient echo** sequence. The spins are dephased and rephased through a set of opposite magnetic gradient fields producing an echo. Since the rephasing π-pulse is missing, the gradient echo sequence depends on T_2^* instead of T_2.

2.3 Magnetic resonance imaging

MRI has become one of the most important non-invasive imaging techniques for diagnostics in the clinical praxis. Not only is it able to provide detailed anatomical information on living organisms with high resolution, but it is also suited for functional and physiological research.

The main idea forming the difference between NMR and MRI is employing gradient magnetic fields during the aquisition of data. In general, linear gradient field alongside any axis can be applied to modify the static field, resulting thus in corresponding linear spatial dependence of resonance frequencies of spins. If we assume the direction of the static field parallel to z-axis, the magnetic field applied during the performance of MRI can be written as

$$B_0(\mathbf{r}) = B_0(0) + \mathbf{G_z} \cdot \mathbf{r}, \tag{2.15}$$

where $\mathbf{G_z}$ denotes the gradient magnetic field $\partial B_z/\partial \mathbf{r}$. As a result, one can excite any selected layer of spins by applying a pulse of the radiofrequency field B_1 with the carrier frequency ω_0 and bandwidth $\Delta\omega$, with layer thickness corresponding to change in Larmor frequency by field gradient by $\pm\frac{\Delta\omega}{2}$. The standard two-dimensional imaging technique then consists of a series of gradient echoes obtained in an applied *readout gradient* $\mathbf{G_r}$ while using a variable *phase-encoding gradient* $\mathbf{G_e}$ applied along a perpendicular direction before the echo is obtained. If we assume for simplicity $\mathbf{G_r}$ parallel with x- and $\mathbf{G_e}$ with y-axis, the recorded signal modulated by relaxation is given by the following expression

$$S(t > \tau) = \int_{\text{sample}} M(x,y) e^{i\gamma\tau_e G_e y} e^{i\gamma(2\tau - t)G_r x} e^{-\frac{t}{T_2}} \,\mathrm{d}x\mathrm{d}y, \tag{2.16}$$

which represents the sum of contributions from all parts of the sample, τ being the time of the gradient inversion in the gradient echo sequence and τ_e the time duration of gradient G_e. After acquiring a two-dimensional array of data (a k-space) where for each phase-encoding parameter $\tau_e G_e$ the Fourier component of the magnetization modulation along y-axis is recorded, it is possible to compute a two-dimensional image by discrete inverse Fourier transformation of the data (Nacher, 2009).

2.3.1 Contrast mechanisms

The resulting image obtained by any MRI method always reflects the actual ^{1}H magnetization distribution in the sample, in other words, the distribution of proton density (PD). Since both water and fat contain high amount of ^{1}H, the contrast generated solely by tissues is poor. However, the differences in composition of diverse tissues result in various relaxation times T_1 and T_2, which open up new possibilities for image contrast in MRI. The amplitude of the signal induced by the spin echo depends on relaxation times as

$$S(t) \propto k\rho \left(1 - e^{-\frac{\mathrm{TR}}{T_1}}\right) e^{-\frac{\mathrm{TE}}{T_2}}, \tag{2.17}$$

where k is an instrumental proportionality factor and ρ is the proton density. By choosing the right combination of the echo time (TE) and the repetition time (TR), it is possible to extract the desired information from the image.

When using a short TE (less than 25 ms) and TR of the order of the longitudinal relaxation time, the **T_1-weighting** is achieved. The values of T_1 typically range from 40 ms in the liver to $\sim$ 100 ms in brain grey matter (Sattler, 2011b). For fat has shorter T_1 than water in normal tissues, it appears brighter in the image.

On the other hand, by applying a sequence with a sufficiently long TR (more than 1500 ms) and long TE (more than 50 ms), **T_2-weighted** image is generated. When compared to the T_1-weighted image, it appears to be inverted with water brighter than fat.

For a basic overview of ^{1}H density, both longitudinal and transversal magnetization ought to be approaching the equilibrium values; therefore a long TR and a short TE are used to acquire the **PD-weighted** image. For demonstrative examples of different types of image weighting along with the pictorial explanation of contrast which stems from the difference in relaxation times see 2.1.

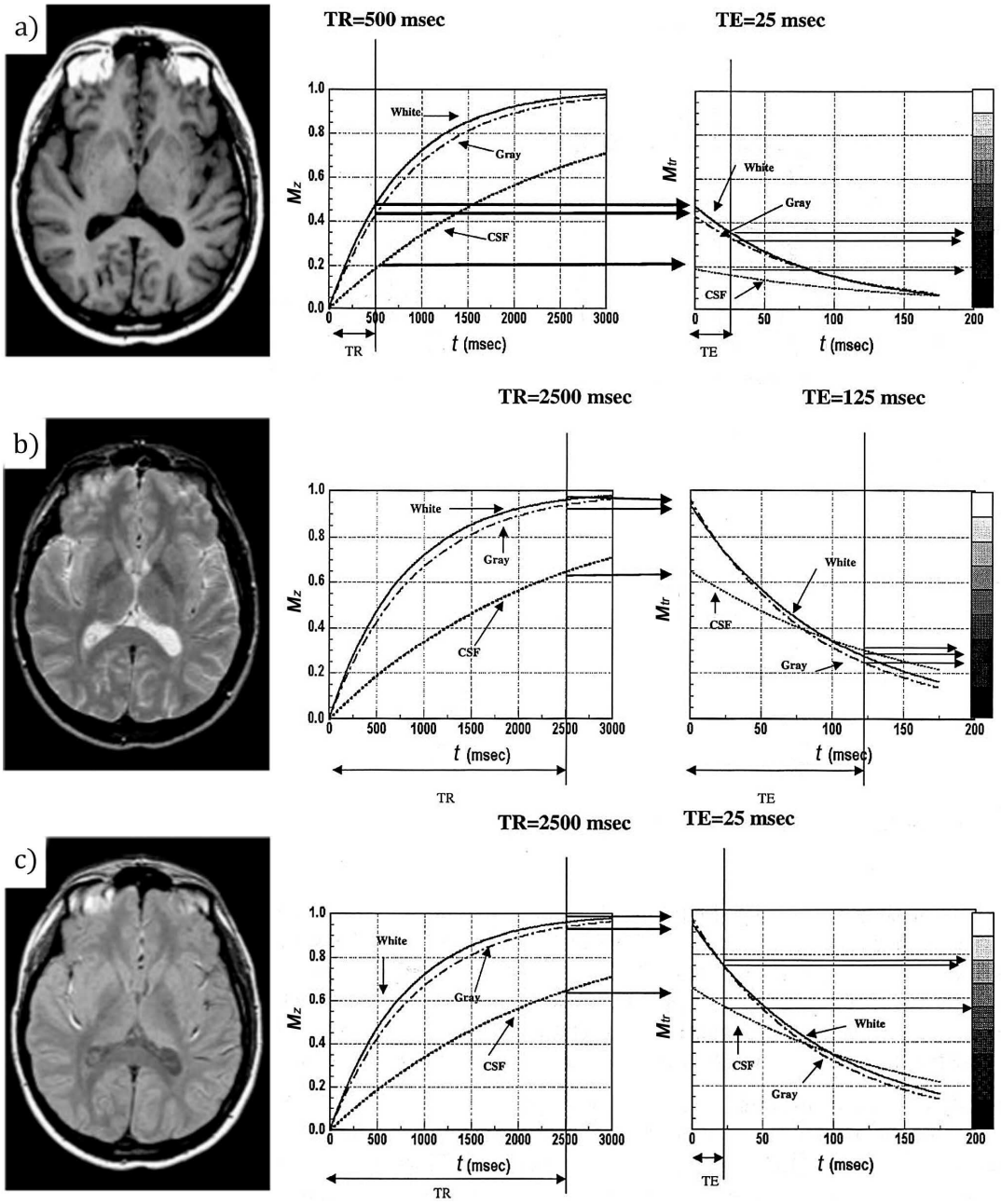

Figure 2.1: The section of brain in the transversal plane - demonstration of various types of MRI contrast: a) T_1-weighted image, b) T_2-weighted image, c) PD-weighted image (weighted by proton density). The graphs indicate the origin of contrast between the white and grey matter, and the cerebrospinal fluid (CSF), showing the evolution of their respective longitudinal (in the middle) and transversal (right) components of magnetization with time. Brain images were adapted from Brown et al. (2014), graphs from Prince and Links (2006).

2.4 Relaxivity of MRI contrast agents

Although it is possible to distinguish various types of tissues in MRI images, the contrast resulting solely from the composition of tissues is not always sufficient. Therefore, contrast agents are introduced to the organism prior to the examination, which

enhances image contrast through shortening of T_1 or T_2 relaxation times of ^{1}H in their surroundings. Considering the different types of weighting of MRI images, shortening of relaxation times leads to positive contrast — increase in signal intensity — in the case of T_1-weighted imaging, and to negative contrast in T_2-weighted imaging. Contrast agents facilitate thus not only early detection of various pathological changes in the body or better definition of tumour delineation (Toy et al., 2014), but they also enable tracking of labelled cells *in vivo* through cellular or molecular imaging (Ahrens and Bulte, 2013; Vuong et al., 2012) or indication of biological processes in the tissue (Tu et al., 2011; Louie, 2013).

To the most widely studied materials for MRI contrast enhancement appertain organic molecules containing a paramagnetic metal ion (e.g. chelate complexes containing Gd^{3+}, Dy^{3+}, Mn^{2+} or Fe^{3+}; Xiao et al., 2011) particularly successful in T_1-weighted imaging, and superparamagnetic nanoparticles based on γ-Fe_2O_3/Fe_3O_4 (superparamagnetic iron oxide – SPIO, ultra-small superparamagnetic iron oxide – USPIO; Gupta and Gupta, 2005) suited for T_2-weighted imaging. The acceleration of proton relaxation near the contrast agent is usually attributed to fluctuations of magnetic dipolar interaction between proton spins and electronic spins of the paramagnetic contrast agent, or the magnetic moment of a nanoparticle (Vuong et al., 2012).

The use of contrast agents in clinical praxis raises considerable safety concern since most magnetic compounds artificially introduced to the organism are toxic. For this reason, a delicate balance between the toxicity and image enhancement needs to be found. Despite the iron-based nanoparticles being relatively safe, it is disputable for examining specialists whether the negative contrast appeared in the T_2-weighted image was induced by them or had any other (e.g. instrumental) cause (Sattler, 2011b). For this reason, Gd-based contrast agents keep their popularity among the specialists for they induce unequivocal positive contrast in the T_1-weighted images, even though gadolinium is highly toxic and accumulates in the brain of examined subjects (Kanda et al., 2015) as well as in the environment (Kulaksiz and Bau, 2011).

2.4.1 Concept of relaxivity

The contrast agent efficacy is quantified by its **relaxivity** r_i, describing how the original relaxation rate $R_{i,0}$ of ^{1}H in pure medium (usually water) was changed by introducing the contrast agent at given concentration c:

$$R_i = R_{i,0} + r_i c, \tag{2.18}$$

where $i \in \{1, 2\}$ for longitudinal and transversal relaxation, respectively. Relaxivity is expressed in units $s^{-1}.mmol^{-1}.dm^3$ (often abbreviated as $s^{-1}.mM^{-1}$) and is usually recalculated to concentration of the corresponding magnetic ion in the contrast agent (for example to c_{Fe} in the case of γ-Fe_2O_3). As a parameter characterising both the material properties of the contrast agent and its interaction with surrounding protons, the relaxivity depends on numerous factors: the temperature and composition of solvent, magnitude of the external magnetic field, concentration range of the contrast agent, further on the size, magnetic moment, aggregation and the type and thickness of coating of the nanoparticles or the number of water ^{1}H nuclei bound to the compound containing paramagnetic ion etc.

From the magnitude of the r_2/r_1 ratio it is possible to assess, whether the contrast agent is applicable for T_1-weighted imaging ($r_2/r_1 < 5$) or T_2-weighted imaging ($r_2/r_1 > 5$).

Due to the primary focus of this study on analysis of the relaxivity of magnetic nanoparticles, i.e. contrast agents suited for T_2-weighted imaging, further text deals with models aiming at describing the influence of MNPs on T_2-relaxation of surrounding protons.

2.4.2 Transversal relaxivity of magnetic particles

When studying the relaxivity of particles, it is appropriate to formulate certain assumptions. Firstly, under the assumption that the diffusion of water molecules is much faster than the Brownian motion of the MNP, it is possible to define the **diffusion correlation time** τ_D of water near the nanoparticle as

$$\tau_D = \frac{d^2}{4D} = \frac{r^2}{D}, \tag{2.19}$$

d and r being the diameter and the radius of the nanoparticle including its coating material, respectively, and D the self-diffusion coefficient of water. τ_D denotes the time needed for the water molecule to diffuse a distance equal to $\frac{\sqrt{2}}{2}d$ in any direction (in three-dimensional space). Secondly, to describe the change in the Larmor frequency of ^{1}H in the surroundings of the nanoparticle, let us consider the z-component of the particle dipolar field (in spherical coordinates R, θ):

$$\Delta B_z(\theta, R) = \frac{\mu_0 M r_c^3}{3} \frac{3\cos^2\theta - 1}{R^3}, \tag{2.20}$$

M the volume magnetization of the magnetic core and r_c its radius. The shift in Larmor frequency of ^{1}H caused by the particle is then $\Delta\omega(\theta, R) = \gamma \Delta B_z(\theta, R)$. For a rough estimate of $\Delta\omega$ it is convenient to calculate its value

$$\Delta\omega = \left|\Delta\omega\left(\frac{\pi}{2}, r_c\right)\right| = \frac{\mu_0 \gamma M}{3} \tag{2.21}$$

at the equator of the magnetic core, or its value at the equator of a coated particle, i.e. rescaled by r_c^3/R^3 from relation 2.20 with $R = r$. Based on the comparison of $\Delta\omega$ and the characteristic frequency associated with the diffusion correlation time $\frac{1}{\tau_D}$, following relaxation regimes for protons near superparamagnetic contrast agents are discussed in the literature (Carroll et al., 2010):

1. **Motional averaging regime (MAR)** (only when the Redfield condition $\Delta\omega \ll \frac{1}{\tau_D}$ is fulfilled; Roch et al., 1999). Water molecules diffuse rapidly around the particle, experiencing thus a broad range of fast changing magnetic fields, which are effectively time averaged. The contribution of MNP to the transversal relaxation rate of ^1H is then

$$R^*_{2,\mathrm{MAR}} = R_{2,\mathrm{MAR}} = \frac{16}{45} f \tau_D (\Delta\omega)^2 \tag{2.22}$$

where $f = V(\text{particles}/V)$ is the volume fraction occupied by the particles in the suspension After recalculation to the metal ion concentration c_M using

the molar mass of the material per formula unit M_{mat} and its density ρ_{mat}

$$\frac{f}{c_{\mathrm{M}}} = \nu_{\mathrm{mat}} = \frac{M_{\mathrm{mat}}}{\upsilon \rho_{\mathrm{mat}}}, \tag{2.23}$$

where $\upsilon = c_{\mathrm{M}}/c_{\mathrm{f.u.}}$ denotes the number of magnetic metal atoms (usually Fe) in the formula unit, the relaxivity yields

$$r_{2,\mathrm{MAR}} = \frac{R_{2,\mathrm{MAR}}}{c_{\mathrm{M}}} = \frac{4d^2(\Delta\omega)^2 \nu_{\mathrm{mat}}}{45D} = \frac{4d^2\gamma^2\mu_0^2 M^2 \nu_{\mathrm{mat}}}{405D}. \tag{2.24}$$

This model is inspired by the outer-sphere relaxation developed for the paramagnetic contrast agents.

2. **Static dephasing regime (SDR)** (for larger particles where $\Delta\omega > \frac{\sqrt{3}\pi}{2}\frac{1}{\tau_D}$; Yablonskiy and Haacke, 1994; Roch et al., 2005). In this regime, any water molecule explores only a small space in comparison to the hydrodynamic volume of the particle. Since water protons can be considered virtually quasistatic, they experience non-averaged variations in local magnetic fields. The transversal relaxation rate is derived under the assumption of its proportionality to the dephasing induced by Larmor frequency dispersion of water protons

$$R^*_{2,\mathrm{SDR}} = \frac{2\pi}{3\sqrt{3}} f \Delta\omega, \tag{2.25}$$

the corresponding relaxivity is then

$$r^*_{2,\mathrm{SDR}} = \frac{2\pi}{9\sqrt{3}} \gamma\mu_0 M \nu_{\mathrm{mat}}. \tag{2.26}$$

The SDR model intended for MRI does not take into consideration the effect of refocusing pulses used in all T_2 measurement sequences. For this reason, equations 2.25 and 2.26 are exact only for R^*_2 and r^*_2, respectively. Nonetheless, they provide a good approximation of R_2 and r_2 for $\frac{5}{\tau_D} < \Delta\omega < \frac{20}{\tau_D}$ (Vuong et al., 2012). Moreover, the rates predicted by SDR yield the highest achievable values for a given volume fraction and a particle equatorial field.

3. **Partial refocusing model (PRM)** (Gillis et al., 2002). If the diffusion correlation time of water molecules is shorter than the echo time $\tau_D < 2\tau_{CP}$ in the employed measurement sequence, the refocusing of proton magnetic moments is inefficient, R^*_2 and R_2 are equivalent. However, if it is not the case, one encounters partial refocusing of proton moments, resulting in decrease of R_2 with respect to R^*_2. PRM, also referred to as echo limited regime (ELR) is based on a spatial division of the outer region relatively far from the particle, where the refocusing pulses are efficient and the Redfield condition is fulfilled, and the inner region, where the magnetic field gradients are too strong for refocusing to occur. The model results in the analytical formula for R_2 in the form (Carroll et al., 2010)

$$R_{2,\mathrm{PRM}} = \frac{7.2 f D x^{\frac{1}{3}} (1.52 + f x)^{\frac{5}{3}}}{d^2}, \qquad \text{where} \qquad x = \Delta\omega\tau_{CP}, \tag{2.27}$$

while R^*_2 is given by the same expression as in SDR 2.25.

As indicated by these three regimes, for a given volume fraction of superparamagnetic particles the transversal relaxation rate is expected to initially increase with increasing particle size (MAR for $\tau_D < 2\tau_{CP}$), reaching maximum d_{SDR} at the transition to SDR

$$d_{\mathrm{SDR}} = \left(\frac{5\pi D\sqrt{3}}{2\Delta\omega} \right)^{\frac{1}{2}}. \tag{2.28}$$

With further increase in the particle diameter, the relaxation rate keeps this value up to another critical diameter

$$d_{\mathrm{PRM}} = \left(\frac{1.49 f D x^{\frac{1}{3}} (1.52 + f x)^{\frac{5}{3}}}{\Delta\omega} \right)^{\frac{1}{2}}, \qquad \text{with} \qquad x = \Delta\omega\tau_{CP}. \tag{2.29}$$

In the case of bigger particles with $d > d_{\mathrm{PRM}}$, R_2 decreases as $\propto 1/d^2$. The behaviour of the relaxivity r_2 predicted by these models was nicely depicted in the paper by Carroll et al. (2010), see figure 2.2.

Moreover, further extensions of the discussed models have been proposed, dealing mostly with the aggregation of particles (e.g. Roch et al., 2005; Matsumoto and Jasanoff, 2008; Vuong et al., 2011) or the shape of clusters (Vuong et al., 2011).

Nevertheless, even theoretical models striving for capturing the r_2 relaxivity were adopted from paramagnetic models focusing on describing r_1 of Gd-chelates. No satisfactory quantitative agreement between theory and experimental data has been achieved yet, despite the fact, that data of r_1 relaxivity are well described by the same models (Gossuin et al., 2016). Another aspect complicating the analysis of r_2 relaxivities is the experimental difficulty to acquire the R_2 data, in contrast to experimentally accessible and widely available R_1 data from the nucear magnetic relaxation dispersion (NMRD) profiles.

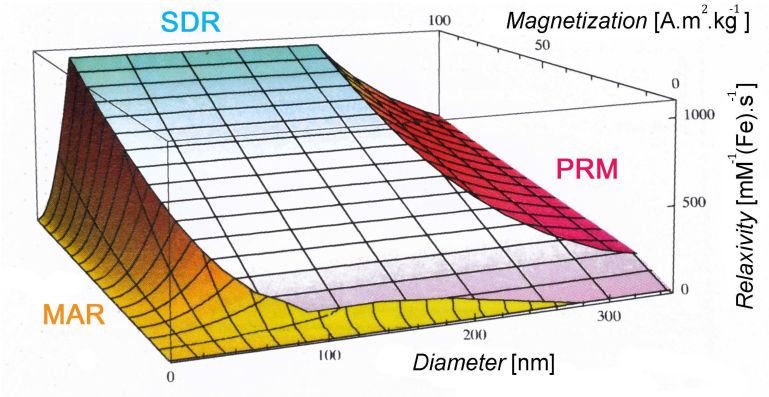

Figure 2.2: Plot of the transverse relaxivity r_2 predicted by MAR, SDR and PRM models, versus particle diameter and specific magnetization. The boundary between SDR and PRM corresponds to $\tau_{CP} = 1$ ms. In the plot of r_2^*, the relaxivity in the range of diameters lying within the PRM regime would keep the same value as in SDR. Adapted from Carroll et al. (2010).

New models considering magnetocrystalline anisotropy

Almost all investigators modelling the effect of MNPs on proton transversal relaxation times considered exclusively superparamagnetic nanoparticles. Nevertheless,

new attempts to describe the relaxation induced by MNPs with high magnetocrystalline anisotropy have been recently presented (Lévy et al., 2013; Rollet et al., 2016). In contrast to the previous models, the general model developed by these authors considers a classical magnetic moment of the MNP and takes into account its dynamical behaviour. Moreover, the model is expected to describe the relaxation induced not only by MNP in the superparamagnetic regime, but also in the frozen state (*rigid dipole regime*). For the calculations are presented in detail in the above-mentioned papers, let us focus on main points of the model.

Let us assume a magnetic particle with diameter d, classical magnetic moment $\boldsymbol{\mu}$ characterised by a solid angle Ω_μ, and uniaxial magnetic anisotropy (constant K) with the anisotropy axis $\mathbf{n_p}$ associated with a solid angle Ω_n, as depicted in figure 2.3.

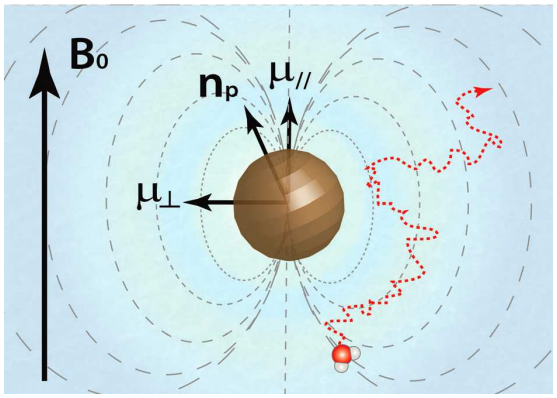

Figure 2.3: Illustration of a water molecule diffusing in the vicinity of a magnetic particle, experiencing various magnitudes of the fluctuating magnetic field created by the particle. Adapted from Rollet et al. (2016)

The hamiltonian coupling $\mathbf{n_p}$ and $\boldsymbol{\mu}$ in an external magnetic field $\mathbf{B_0}$ is then

$$U(\Omega_\mu, \Omega_n) = -\boldsymbol{\mu}\cdot\mathbf{B_0} - KV_m\frac{(\boldsymbol{\mu}\cdot\mathbf{n_p})^2}{|\boldsymbol{\mu}|^2}, \tag{2.30}$$

V_m being the volume of magnetic portion of the particle (i.e. without non-magnetic coating). Dipolar interaction of ^{1}H magnetic moment μ_H with moment of the MNP is considered as a stationary perturbation to the interaction of μ_H with $\mathbf{B_0}$. After protracted calculation, the formula for transversal relaxation rate can be written as follows:

$$\begin{aligned}
R_2(\omega_I) &= C + V(\omega_I)\\
C &= \frac{(\mu_0\gamma)^2}{135\pi}\left(\frac{2N}{Dd}\right)\left\{\overline{3\mu_\perp{}^2\,\mathrm{Re}\left[g\left(\sqrt{\frac{\tau_D}{\tau_\perp}}\right)\right]} + \right.\\
&\quad \left. + \overline{4\left(\mu_\parallel{}^2 - \overline{\mu_\parallel}^2\right)\mathrm{Re}\left[g\left(\sqrt{\frac{\tau_D}{\tau_\parallel}}\right)\right]} + 4\overline{\mu_\parallel}^2\right\}\\
V(\omega_I) &= \frac{(\mu_0\gamma)^2}{135\pi}\left(\frac{2N}{Dd}\right)\left\{\overline{\frac{7}{2}\mu_\perp{}^2\,\mathrm{Re}\left[g\left(\sqrt{i\omega_I\tau_D + \frac{\tau_D}{\tau_\perp}}\right)\right]} + \right.\\
&\quad \left. + \overline{3\left(\mu_\parallel{}^2 - \overline{\mu_\parallel}^2\right)\mathrm{Re}\left[g\left(\sqrt{i\omega_I\tau_D + \frac{\tau_D}{\tau_\parallel}}\right)\right]} + 3\overline{\mu_\parallel}^2\,\mathrm{Re}\left[g\left(\sqrt{i\omega_I\tau_D}\right)\right]\right\}
\end{aligned} \tag{2.31}$$

where the upper line represents the classical average over a statistical ensemble (or equivalently over all possible system histories), N denotes the number of particles

in a unit volume, $\mu_\parallel$ and $\mu_\perp$ are the longitudinal and transversal component of particle magnetic moment at the initial statistical time $t = 0$, respectively, whose relaxation is characterised by relaxation times $\tau_\parallel$ and $\tau_\perp$ associated with the initial configuration; g is a function of complex variable

$$g(x) = \mathrm{Re}\left[\frac{1+\frac{x^{\frac{1}{2}}}{4}}{1+x^{\frac{1}{2}}+\frac{4x}{9}+\frac{x^{\frac{3}{2}}}{9}}\right].$$

For MNP with hamiltonian 2.30, three typical correlation times are to be taken into consideration: apart from the Néel relaxation time τ_N (see equation 1.2, $E_B = KV_m$) and the Brown relaxation time τ_B (see eq. 1.4), this model considers also the **damping time** τ_p associated with the precession of $\boldsymbol{\mu}$ around the effective magnetic field $\boldsymbol{B_e}$

$$\mathbf{B_e} = -\frac{\partial U}{\partial \boldsymbol{\mu}} = \mathbf{B_0} + 2KV_m \frac{(\boldsymbol{\mu}\cdot\mathbf{n_p})\cdot\mathbf{n_p}}{|\boldsymbol{\mu}|^2}. \tag{2.32}$$

The damping time is a function of the initial configuration (Ω_μ, Ω_n at time $t = 0$) and reads

$$\tau_p = \frac{2\pi}{\alpha|\gamma_e||\mathbf{B_e}|} \tag{2.33}$$

with α is the damping factor used in the MNP Landau-Lifschitz-Gilbert equation (for more details see Raĭkher and Shliomis, 1994) and $|\gamma_e|$ the absolute value of electronic gyromagnetic ratio. The damping factor takes account of fluctuations of magnetic moment orientation in the crystal lattice and related energy dissipation through vibrational modes.

The appropriate choice of transversal and longitudinal correlation times then results from the mutual comparison of the magnetic anisotropy energy of MNP and the energy of thermal fluctuations. Let us consider following asymptotic cases (Raĭkher and Shliomis, 1994):

(a) **Weak anisotropy** ($KV_m \gtrapprox k_BT$). Magnetic anisotropy is comparable to thermal fluctuations — thermal fluctuations can either overcome the energy barrier inducing Néel relaxation, or are too small and merely move the magnetic moment from the equilibrium in its potential well, causing $\boldsymbol{\mu}$ to relax with the damping time τ_p. In such case, $\mathbf{n_p}$ and $\boldsymbol{\mu}$ are weakly coupled, τ_N and τ_B are in the same order of magnitude and

$$\tau_\parallel = \frac{\tau_N\tau_B}{(\tau_N+\tau_B)} \quad \text{and} \quad \tau_\perp = \frac{\tau_p\tau_B}{(\tau_p+\tau_B)} \tag{2.34}$$

(b) **Strong anisotropy** ($KV_m \gg k_BT$). MNP is in the frozen state, then $\tau_N \gg \tau_B$. Furthermore, $\mathbf{n_p}$ and $\boldsymbol{\mu}$ are strongly coupled resulting in sharing the same Brownian dynamics. In this case,

$$\tau_\parallel = \frac{\mathrm{d}\ln\mathscr{L}(\xi)}{\mathrm{d}\ln\xi}\tau_B \quad \text{and} \quad \tau_\perp = \frac{2\mathscr{L}(\xi)}{\xi-\mathscr{L}(\xi)}\tau_B, \tag{2.35}$$

where $\mathscr{L}(\xi) = \coth(\xi) - 1/\xi$ is the Langevin function and $\xi = \mu B_0/k_BT$ its argument.

To discriminate between the aforementioned cases, it is useful to assess the magnitude of the ratio $P = \tau_N/\tau_B$. More precisely, one considers the relations 2.34 for $P < 10$ and rel. 2.35 for $P > 10$.

For a MNP in a high magnetic field (i.e. for a high value of ω_I), the only important contribution to $R_2(\omega_I)$ in eq. 2.31 is the third term of C:

$$R_2(\omega_I) = \frac{(\mu_0\gamma)^2}{135\pi}\left(\frac{2N}{Dd}\right)[4\mu^2]. \tag{2.36}$$

Considering the molar concentration of metal c_{M}, the ratio $r_2(\omega_I) = R_2(\omega_I)/c_{\mathrm{M}}$ can be rewritten as

$$r_2(\omega_I) = \frac{4d^2\mu_0^2\gamma^2M^2\nu_{\mathrm{mat}}}{405D}. \tag{2.37}$$

This asymptotic evolution yields the same result as $r_{2,\mathrm{MAR}}$ (see eq. 2.24).

3. ε-Fe_2O_3

3.1 Polymorphs of iron(III) oxide

Iron(III) oxide is a polymorphic compound, which means that it can exist in various solid phases with the same chemical composition but different crystal structure resulting in distinct physical properties. Until now, five crystalline polymorphs have been identified under ambient conditions (structural information adapted from Machala et al., 2011, unless otherwise stated):

(i) α-Fe_2O_3 (haematite), the most common and stable polymorph with a rhombohedrally centred hexagonal crystal structure of corundum type, $R\bar{3}c$ space group and lattice parameters $a = 5.036\,\text{Å}$ and $c = 13.749\,\text{Å}$;

(ii) β-Fe_2O_3, a rare polymorph existing only in a nanosized form, with a cubic body-centred crystal structure of bixbyite type, crystallizing in $Ia\bar{3}$ space group with $a = 9.393\,\text{Å}$;

(iii) γ-Fe_2O_3 (maghemite), the second most common polymorph with a cubic crystal structure of an inverse spinel type, $P4_132$ space group with $a = 8.351\,\text{Å}$ and vacancies disordered over the octahedral cation sites in the crystal lattice;

(iv) ε-Fe_2O_3, similarly to β-Fe_2O_3 a nanosized polymorph with rare natural occurrence, orthorhombic crystal structure, crystallizing in $Pna2_1$ space group with lattice parameters $a = 5.102\,\text{Å}$, $b = 8.781\,\text{Å}$ and $c = 9.466\,\text{Å}$ (Sakurai et al., 2005);

(v) the recently reported ζ-Fe_2O_3, the first monoclinic polymorph of iron(III) oxide stable under ambient conditions, formed during high pressure treatment of β-Fe_2O_3, with $I2/a$ space group and lattice parameters $a = 9.683\,\text{Å}$, $b = 10.00\,\text{Å}$ and $c = 8.949\,\text{Å}$ (Tuček et al., 2015).

All iron(III) oxide polymorphs easily transform in response to heating or pressure treatment, usually forming α-Fe_2O_3 which is the most thermodynamically stable phase of Fe_2O_3 under ambient conditions. While α-Fe_2O_3 and γ-Fe_2O_3 can be widely found in nature (hence the mineralogical names), and due to their stability it is possible to select the suitable synthetic route to prepare the desired morphological form, the stability of the rare metastable polymorphs β-Fe_2O_3 and ε-Fe_2O_3 depends on the nanodimensional character of their particles (Tuček et al., 2015).

3.2 ε-Fe_2O_3

For its low surface energy, the dark brown polymorph ε-Fe_2O_3 exists only in nanocrystalline forms. It has been prepared in three morphological forms (Tuček et al., 2010): nanoparticles (in sizes $\sim 10 - 200\,\text{nm}$), nanorods and nanowires with typical width $\sim 10 - 120\,\text{nm}$ and length more than $200 - 800\,\text{nm}$ (Jin et al., 2004; Sakurai et al., 2008; Ohkoshi et al., 2016); or epitaxial films with thickness $\sim 100\,\text{nm}$ (Gich et al., 2010). Nanorods of ε-Fe_2O_3 were recently reported to behave as rod magnets (Ohkoshi et al., 2016). The character of the size distribution

of nanoparticles and nanorods is tightly connected with the employed synthesis route. Due to its thermodynamic metastability, it is difficult to prepare ε-Fe_2O_3 in a pure form without admixtures of other iron(III) oxide polymorphs. A widely respected synthesis method to achieve high phase purity employs the mesoporous silica template, which prevents the aggregation of particles and provides the space confinement during their growth enhancing thus their thermal stability (Brázda et al., 2014).

In the ε-Fe_2O_3 structure (see figure 3.1), the iron atoms occupy four crystallographically inequivalent cation sites: three different octahedral sites (Fe_{D01}, Fe_{D02}, Fe_{RO}) and one tetrahedral site (Fe_T), determining the magnetic behaviour of the material. Each of the four inequivalent magnetic sublattices exhibits different temperature dependence (Tuček et al., 2010). The material is ferrimagnetic at room temperature, with relatively low saturation magnetization $\sim 17\,\mathrm{A.m^2.kg^{-1}}$ and giant coercive field $\sim 2\,\mathrm{T}$ ascribed to its high magnetocrystalline anisotropy $\sim (2-5).10^5\,\mathrm{J.m^{-3}}$ (Jin et al., 2004; Tseng et al., 2009). It undergoes a transition to the paramagnetic state at Curie temperature $\sim 490\,\mathrm{K}$, and a two step magnetic transition in the temperature range 100—150 K accompanied by a small change in lattice parameters and high decrease in coercive field (Kohout et al., 2015; Popovici et al., 2004). When cooled to 150 K, a spin reorientation transition occurs in ε-Fe_2O_3, followed by the transition of Fe^{3+} ion from the high spin to the intermediate spin state (Kohout et al., 2015). Also, coupling of the magnetic and dielectric properties of ε-Fe_2O_3 was reported (Gich et al., 2006a), demonstrating thus its multiferroic character.

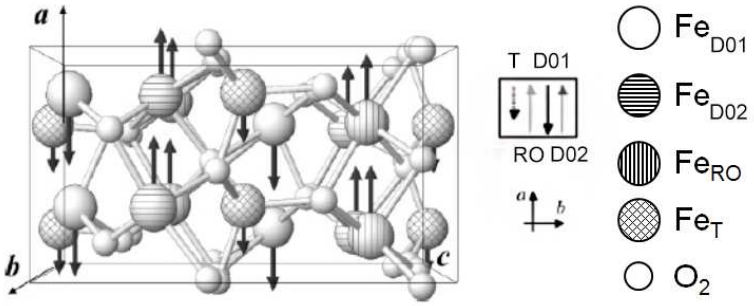

Figure 3.1: The crystal and magnetic structure of ε-Fe_2O_3. The cation sites are distinguished by various patterns, the size and orientation of the magnetic moment related to each site is indicated by an arrow. Adapted from Gich et al. (2006b).

The high coercive field and multiferroic behaviour suggest the enormous application potential of ε-Fe_2O_3 as a functional magnetic material, especially for applications in need of materials with considerable magnetic hardness (e.g. in storage media, or devices controlled by external magnetic or electric field Tuček et al., 2010).

3.2.1 Other materials derived from ε-Fe_2O_3

The magnetic and electric properties of ε-Fe_2O_3 can be further modified by substituting various trivalent ions for a fraction of iron atoms.

Rhodium-substituted ε-Fe_2O_3 (ε-$Rh_xFe_{2-x}O_3$) exhibits the coercive field up to $\sim 3.1\,\mathrm{T}$, the largest value among metal-oxide-based magnets which is comparable

to those of rare-earth magnets (Namai et al., 2012). Moreover, it manifests electromagnetic wave absorption with the highest resonance frequency (up to 209 GHz) among the known magnetic materials (Namai et al., 2012). Indium-substituted ε-$In_xFe_{2-x}O_3$ is the first example of a pyroelectric material displaying a phase transition between ferrimagnetism and antiferromagnetism (Sakurai et al., 2007). Gallium-substituted ε-$Ga_{0.5}Fe_{1.5}O_3$ has attracted considerable attention since its absorption frequency in the range of millimetre waves corresponds well to the automotive radar frequency of 76 GHz (Ohkoshi et al., 2017).

Another material studied for its high-frequency resonance with electromagnetic waves of millimetre wavelengths is aluminium-substituted ε-$Al_xFe_{2-x}O_3$. Owing to the smaller ionic radius of Al, the lattice parameters decrease with increasing concentration of Al atoms. Furthermore, the Curie temperature and room-temperature coercive field were found to decrease, while the room-temperature magnetization was enhanced. As the third most abundant element, aluminum represents a very economical substituent, making thus this class of materials favourable for industrial applications (Namai et al., 2009; Yoshikiyo et al., 2012; Tuček et al., 2010).

4. Experimental details

The examined samples are labelled according to the following key:

- The formula ε-$Fe_{2-x}Al_xO_3$ reflecting the chemical composition of the samples is shortened to "ε-FeAl".
- The type of surface modification is specified after the hyphen "-". Samples coated with silica are labelled by "s" followed by the thickness of silica coating in nanometers as determined from the transmission electron microscopy analysis (i.e. ε-FeAl-s06 denotes nanoparticles of ε-$Fe_{2-x}Al_xO_3$ encapsulated in silica of thickness $\sim$ 6 nm). Citrated sample can be recognized by "cit", while particles without any type of coating are labelled by "bare".

4.1 Preparation of samples

4.1.1 Synthesis of nanoparticles

Our synthesis of ε-$Fe_{2-x}Al_xO_3$ nanoparticles was based on published procedures for preparation of mesoporous silica (Zhao et al., 1998) and its impregnation by iron nitrate solution (Delahaye et al., 2006). It was aimed to achieve chemical composition with $x = 0.25$. Briefly, it consisted of following steps:

1. **Preparation of the mesoporous silica SBA-15 template.** In total 12.0 g of PEG-PPG-PEG triblock co-polymer consisting of poly(ethylene oxide) – PEO and poly(propylene oxide) – PPO (P123) (average relative molecular mass $M_r \approx 5800$) was dissolved in 360 ml of 2 M HCl and 90 ml of water at 40 °C. After a day of stirring, 25.5 g of tetraethoxysilane (TEOS) was added dropwise during one hour. The following day, the temperature was raised to 75 °C, and the reaction was kept proceeding for three more days. The product was filtered and washed eight times. The white solid was dried for two days at 60 °C and then calcined at 500 °C for 10 hours. The period of the hexagonal packing of the pores was 11.1 nm.

2. **Impregnation of the silica template with the solutions of iron and aluminium nitrate.** The impregnation solution had concentration of metal ions equal to 2 M with molar ratio Al:Fe equal to 1:7. The sources of metal ions ($Fe(NO_3)_3 \cdot 9\,H_2O$ and $Al(NO_3)_3 \cdot 9\,H_2O$) were dissolved in water at 50 °C. 3.2 ml of the impregnation solution was introduced dropwise into the stirred suspension of 4.0 g of SBA-15 matrix in hexane heated to 50 °C. After a day, the stirring was terminated, the product was decanted and evaporation of the remaining hexane was carried out. The product was dried overnight at 80 °C.

3. **Thermal treatment.** The sample was annealed at 1100 °C for four hours.

4. **Removal of the template and preparation of water suspension.** The silica template was removed by alkaline hydrolysis in concentrated solution of NaOH. The particles were collected by centrifugation and were thoroughly washed by the same NaOH solution and thereafter by water. The purified

product was dispersed in water at a concentration of particles $\sim 9\,\mathrm{mg.ml^{-1}}$ (further denoted as "parent" suspension).

4.1.2 Coating of nanoparticles with silica

A part of ε-$Fe_{2-x}Al_xO_3$ nanoparticles prepared as described in section 4.1.1 was further coated with amorphous $SiO_x(OH)_y$ (silica) according to following steps (dereived from the synthesis of silica partricles by Stöber et al., 1968):

1. **Calculation of TEOS volume.**The calculated total mass of nanoparticles in suspensions for subsequent encapsulation was used to determine the amount of TEOS to obtain the desired thickness of silica coating. The following volumes of TEOS were used to obtain various thickness of silica coating (for ~ 47.5 mg of particles, i.e. ~ 5.3 ml of parent suspension):

Sample	**TEOS [μl]**	**Silica[a] [nm]**
ε-FeAl-s06	160	5.5
ε-FeAl-s10	400	9.8
ε-FeAl-s17	820	16.7
ε-FeAl-s21	1640	20.6

[a] Resulting thickness of silica coating determined from transmission electron microscopy, as mentioned later.

2. **Stabilization of nanoparticles by citrate.** After centrifugation of the parent suspension (14 000 rpm with centrifuge rotor radius 7.7 cm, 30 min, supernatant removed), the particles were dispersed in ice-cold 0.1 M citric acid and treated by ultrasound for 10 min. Again, separation by centrifugation followed (14 000 rpm, 5 min, sup. removed).

3. **Washing cycle I.** The particles were washed in water using ultrasound bath until the dispersion of particles, and separated by centrifugation (14 000 rpm, 15 min, sup. removed).

4. **Preparation of reaction mixture.** The particles were dispersed in water (10 ml) and alkalised with three drops of ammonia by means of a probe-like ultrasonicator. The suspension after sonication was then added dropwise to the flask with reactive mixture (10 ml of 24 % ammonium hydroxide, 150 ml of 96 % ethanol, 40 ml of water) equipped with a Teflon stirrer and tempered in an ultrasound bath at 47 °C. After 5 min, the volume of TEOS calculated in step 1 was added to the mixture. The ultrasound was turned off after 45 min and the reaction mixture was kept in the tempered bath for approximately 18 hours.

5. **Washing cycle II.** The reaction mixture was centrifuged in 5 × 50 ml tubes (7750 rpm with centrifuge rotor radius 10.4 cm, 90 min, sup. removed). The particles were dispersed in 96 % ethanol using ultrasound and transferred

into 2 tubes. A few washing cycles followed: 2× by 40 ml of ethanol and 3× by 40 ml of water, centrifuged after each treatment (7750 rpm, 60 min).

6. **Fractionation.** The particles were diluted by 120 ml of water and shortly sonicated. The removal of heavy fraction was carried out by differential centrifugation in 3 × 50 ml tubes at 2000 rpm for 15 min. The supernatant was collected as the final product, whereas the residue was discarded.

4.1.3 Stabilization of nanoparticles with citrate

Sample labelled ε-FeAl-cit was stabilised solely by chemisorption of citric acid which was subsequently converted to citrate. The stabilisation procedure was similar to the one described in the previous section 4.1.2:

1. **Stabilization by citrate.** After separation of bare particles from 1 ml of the parent suspension (14 000 rpm with centrifuge rotor radius 7.7 cm, 30 min, sup. removed), the particles were dispersed in ice-cold 0.1 M citric acid and treated by ultrasound for 5 min.

2. **Washing cycle.** After separation (14 000 rpm, 5 min, sup. removed), the particles were washed in water using ultrasound bath, and another separation followed (14 000 rpm, 15 min, sup. removed).

3. **Alkalization.** 20 ml of water and three drops of ammonium were added to the sediment and the mixture was dispersed by probe-like ultrasonicator for 30 min.

4. **Size fractionation.** The removal of heavy fraction was carried out by differential centrifugation in 2 × 50 ml tubes at 2000 rpm with centrifuge rotor radius 10.4 cm for 15 min. The supernatant was collected as the final product, whereas the residue was discarded.

4.2 Fundamental characterisations

4.2.1 Composition and concentration of nanoparticles

The chemical composition of bare magnetic cores, i.e. the ratio of Fe : Al was determined by means of X-ray fluorescence spectroscopy (XRF) on Eagle III μ-Probe spectrometer with Rh-tube.

The X-ray powder diffraction (XRPD) using Cu K_α radiation was employed to obtain the phase composition, crystal structure. The XRD patterns were measured using the Bruker D8 Advance diffractometer in the Bragg-Brentano geometry and analysed by the Rietveld method using FullProf.2k (Version 5.9) software (Rodríguez-Carvajal, 2001; Roisnel and Rodríquez-Carvajal, 2001). The instrumental profile was ascertained from a strain-free tungsten powder with a crystallite size of 9.4 μm.

The concentration of iron in aqueous solutions was derived from inductively coupled plasma mass spectrometry (ICP-MS) analysis using an Elan DRC-e (Perkin-Elmer). Aliquots of suspensions weighed on analytical scales were successively

Table 4.1: Overview of the parameters computed from the log-normal fit 1.6 of equivalent particle diameter distributions (adapted from Zender, 2015)

Symbol	Value	Comments
$\bar{d}$	$d_0\, e^{\frac{\sigma^2}{2}}$	mean diameter
SD	$\bar{d}\,\sqrt{(e^{\sigma^2}-1)}$	standard deviation of the mean diameter
RSD	$\frac{\mathrm{SD}}{\bar{d}} = \sqrt{(e^{\sigma^2}-1)}$	relative standard deviation of the mean, coefficient of variation
PDI	$\mathrm{RSD}^2 = e^{\sigma^2} - 1$	polydispersity index, dispersivity
$\hat{d}$	$d_0\, e^{-\sigma^2}$	mode diameter (maximum of the distribution)
$\bar{d}_V$	$d_0\, e^{\frac{7}{2}\sigma^2}$	volume-weighted mean diameter

treated by HF, the mixture of HF and HNO_3, and finally to HNO_3. Silicon was removed during decomposition of sample as volatile SiF_4. The final solution for the ICP-MS measurement was prepared in 2 % HNO_3 matrix. The determined concentrations were verified through analysis of iron by the atomic absorption spectroscopy (AAS) with flame atomization at wavelength 248.3 nm using the standard addition method.

4.2.2 Nanoparticle sizes

Transmission electron microscopy (TEM) was carried out on Philips CM 120 with accelerating voltage of 120 kV and LaB_6 cathode to assess the morphology and size of the particles. The samples were prepared on carbon-coated copper grids by evaporation of a thin film of diluted suspension of particles. Bright field TEM images shown later in figure 5.5 were analysed using NIS-Elements software (Nikon Instruments Inc., Melville, USA). The sizes of magnetic cores, coated nanoparticles as a whole and the thickness of silica were collected and analysed separately, a cutout from an analysed image is given in figure 4.1 as an example. The *log-normal distribution* of particle sizes was assumed

$$P(d) = \frac{1}{\sqrt{2\pi}\sigma d} e^{-\frac{\ln^2\left(\frac{d}{d_0}\right)}{2\sigma^2}}, \tag{1.6}$$

where d denotes the equivalent diameter, i.e. the diameter of a spherical particle having the 2D projection of the same area as the corresponding particle in the analysed TEM image; d_0 is the median of equivalent diameters, σ the standard deviation of $\ln d$. To enhance the understanding of the system, other statistical parameters were computed from d_0 and σ; for employed formulas see Table 4.1.

The thickness of silica coating l was fitted by the *normal distribution* with parameters l_0 (mean thickness) and σ_g (standard deviation of the mean):

$$P(l) = \frac{1}{\sqrt{2\pi}\sigma_g} e^{-\frac{(l-l_0)^2}{2\sigma_g^2}}. \tag{4.1}$$

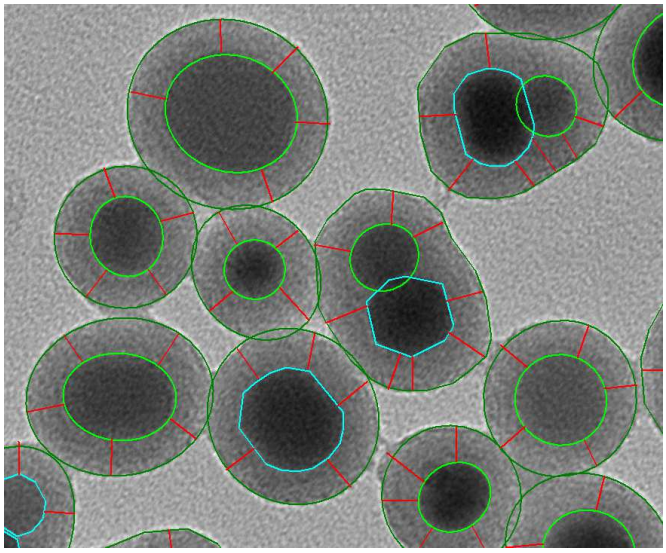

Figure 4.1: Detail of a TEM image of ε-FeAl-s10 analyzed manually with NIS software; light green and blue lines circumscribe magnetic cores of the particles, dark green lines surround coated particles and their clusters, and red line segments show the silica thickness.

The hydrodynamic size of coated particles d_{DLS} was probed by dynamic light scattering (DLS) in water suspension at 25 °C on Malvern Zetasizer Nano S with 4 mW laser of wavelength 633 nm. Although no dependence of d_{DLS} on the concentration of suspensions was found (checked for the sample ε-FeAl-s21 in the range of concentrations from 0.002 mM to 2.41 mM), the probed samples were diluted to similar concentrations $\sim$ 0.25 mM.

4.2.3 Magnetic properties and hyperfine interactions

Magnetic properties of bare and coated particles were studied in DC fields by SQUID magnetometry using a Quantum Design MPMS XL 7T and VSM module of PPMS 14T system. Before the measurements, coated samples were subjected to an identical drying procedure at 105 °C under normal pressure. For most magnetic measurements, the samples were prepared in the form of compacted powders; however, the measurement of hysteresis curves of bare sample was carried out on highly compacted dispersions of particles in superglue to prevent the particles from rotational movements in the magnetic field. Careful demagnetization of the magnet MPMS XL 7T was carried out by repeatedly using the reset function prior to the zero-field-cooled/field-cooled (ZFC/FC) measurements. Since this option is not possible for PPMS 14T, the residual field was minimized by applying the so called oscillate mode of approach to zero field, typically starting at 0.5 T. The samples were demagnetized in 250 °C prior to the ZFC/FC measurements in SQUID.

Hyperfine interactions in iron and the influence of aluminium doping were examined by Mössbauer spectroscopy (MS). Transmission spectra were acquired with a ^{57}Co/Rh source with constant acceleration in zero external magnetic field, calibration of velocities and isomer shifts were related to α-Fe at room temperature 23 °C. Spectra were analysed using CONFIT software (Žák and Jirásková, 2006).

4.3 Relaxometry

To obtain relaxivities r_2 of the samples in various external magnetic fields, spin-spin relaxation times T_2 of the suspensions were measured employing several NMR and

MRI instruments, and thence various methods and parameters of the measurements (for a basic overview of the instruments see table 4.2).

Table 4.2: Overview of instruments used in the relaxometric study

Instrument	**Type**	**B_0 [T]**	**^{1}H ω_0 [MHz]**
Bruker Minispec 20mq	relaxometer	0.47	20
Bruker Minispec 40mq	relaxometer	0.94	40
Siemens Magnetom Avanto	MRI scanner	1.5	64
Siemens Magnetom Trio	MRI scanner	3.0	128
Bruker Biospec 47/40 USR	MRI experimental scanner	4.7	200
Bruker Avance III HD 500MHz	NMR spectrometer	11.75	500

B_0 – the external magnetic field; ω_0 – the Larmor frequency of ^{1}H nuclei in corresponding magnetic field

4.3.1 Magnetic field dependence

The procedure to obtain the relaxivity is lengthy and must be repeated for each magnetic field. It can be summarised in following points:

1. For each examined sample, five aqueous suspensions of different concentrations were prepared (further referred to as "subsamples" to facilitate the understanding).

2. The CPMG sequences were applied successively on all subsamples of examined suspensions. The signal from the subsample was collected in dependence on the time t passed since the initial 90°pulse; the intensity of the signal being proportional to the amplitude of the transversal spin magnetization.

3. The experimental points related to the decreasing transversal magnetization and consequently to the spin-spin relaxation time were fitted by the relation

$$A(t) = C + De^{-\frac{t}{T_2}}. \tag{4.2}$$

   to obtain the T_2 values. C and D are parameters of the fit in this case.

4. The spin-spin relaxation rates $R_2 = \frac{1}{T_2}$ were calculated and then plotted as a function of concentration $R_2(c)$ for each sample.

5. The relaxivity r_2 was received from the linear regression of the $R_2(c)$ data as its slope.

The magnetic field dependence of relaxivity was measured at 23 °C and 40 °C, although sometimes precise determination of temperature was hardly possible. All suspensions were stirred and placed in an ultrasound bath prior to their measurements.

In both relaxometers, the CPMG sequence was employed with echo time TE = 2 ms, repetition time TR = 5 s and number of acquisitions (scans) equal to 16.

The relaxation time was obtained by automatic fitting procedure implemented in Minispec operating software. In Bruker Minispec 20mq relaxometer, the temperature was controlled by an external water bath and probed directly in the suspension before and after each measurement. On the other hand, in Bruker Minispec 40mq the default temperature was set to 40 °C, therefore the experiments in 23 °C was performed with preliminary cooling the subsamples to 19 °C in an external water bath, measuring in the relaxometer with shorter duration of the experiment (4 scans, TE = 2 ms, TR = 5 s). The temperature change during the measurement was estimated at 5 °C/30 s based on an experiment with water in a sample tube, in which the tube with precooled water (20 °C) was inserted in the relaxometer and the temperature was continuously monitored over 1 min.

In Siemens scanners, all subsamples were examined in Eppendorf tubes placed in a polystyrene box inserted in a head coil. The series of 2D images were acquired by a spin echo sequence with three different echo times: 6.7 ms (Avanto) / 8 ms (Trio), 20 ms and 50 ms. The T_2 relaxation times were gathered through an image analysis by integrating the signal over each tube disk in the picture. The temperature was roughly adjusted by a water bath of the desired temperature in the box with the water level bellow the sample tubes. Therefore, only limited temperature control was possible.

In Bruker Biospec experimental scanner, the subsamples were measured one by one employing the CPMG sequence with TE = 6.72 ms and 128 or 256 scans according to the relaxation rate of the corresponding subsample. The experiments in 23 °C were performed in the room temperature without further adjusting; however, for experiments in 40 °C a "home-made" set-up with hot air flow was created, and the temperature was monitored by a laboratory alcohol thermometer before each measurement.

Bruker Avance III spectrometer enables acquisition of high-quality NMR spectra. In order to reduce the radiation damping due to high volume of water present in the suspensions, a small amount of the subsample (70 µl) was pipetted into and spread in the interspace between two sample tubes. The deuterated tetrachloroethane $C_2D_2Cl_4$ was inserted in the inner sample tube to provide the lock signal. A modified CPMG sequence with a variable TE, TR = 15 − 23 s and 8 scans was employed. Spectra were analysed using Bruker TopSpin software, the experimental points used to compute the T_2 values were obtained from the intensity of the water peak in the corresponding series of spectra. The area of the peak was assumed to be less precise due to a peak of $C_2D_2Cl_4$ overlapping with the water peak. A reliable temperature control was achieved via heated airflow and thermocouple in close contact with the sample.

4.3.2 Temperature dependence

The dependence of relaxivities r_2 on temperature was measured merely in Bruker Minispec 20mq relaxometer and Bruker Avance III spectrometer, the two instruments offering a satisfactory level of temperature control. Only the most concentrated subsamples were used since the experiments were highly time-consuming, and in the case of the relaxometer it is also very difficult to achieve exactly the same conditions for measuring all subsamples. The contribution of the relaxation rate of pure water in relation 2.18 was neglected for the experimental error of r_2 is at least

by one or two orders of magnitude greater.

4.4 Cytotoxicity

The cytotoxicity of samples encapsulated in silica was examined through the quantification of viability of cells incubated with nanoparticles. Following Fabryova et al. (2014), fat tissue derived mesenchymal stem cells isolated from transgenic luciferase expressing Lewis rats were seeded in a tissue flask and passaged to reach sufficient amount. Then the cells were re-distributed to flasks ($2 \cdot 10^6$ cells per 75 cm^2 flask) and labelled by addition of 0.2 mM of f.u. suspensions of nanoparticles. After 48 hours of incubation (37 °C, 5% CO_2 atmosphere), the cells were washed with phosphate-buffered saline and detached from the flask by addition of 5 ml of trypsin (0.05%, Thermo Fisher Scientific, Waltham, MA, USA). Trypsinization was stopped by 10 ml of 10% fetal bovine serum after 5 minutes of incubation. The cells were then washed out of the tissue flasks and centrifuged at 1500 rpm for 5 min. The pellet was re-suspended in 5 ml of PBS and centrifuged once more to remove the rest of the contrast agent from the buffer. The final cell pellet was re-suspended in 0.5 ml PBS, and the cells "harvested" this way were counted in the Burker chamber under a light microscope. Cell viability was assessed by using the Trypan blue (Sigma Aldrich, USA) exclusion test. Trypan blue does not traverse an intact cell membrane; therefore, only dead cells are stained. Cell viability was calculated as a ratio of viable (uncoloured) to all cells. Nevertheless, the calculated viability is related to adhered cells only and does not take into account differences in proliferation or non-adhered cells lost by washing the flasks before detaching the cells. For this reason, another more accurate parameter is provided:

$$\text{gain} = \frac{\text{number of "harvested" cells incubated with particles}}{\text{number of "harvested" cells in control sample}} \cdot (\text{viability}). \quad (4.3)$$

Considering the differences in cell proliferation and adhesion between the labelled cells and the control, the gain enables thus a more realistic assessment of the cytotoxicity.

Moreover, the viability was verified also by bioluminiscence. Since living cells used in the experiment express luciferase, adding luciferin into the medium results in a biochemical reaction producing light solely in viable cells.

5. Results and discussion

5.1 Characterisation of the samples

5.1.1 X-ray fluorescence spectroscopy

The chemical composition of bare particles of $Fe_{2-x}Al_xO_3$ was determined from XRF spectra to be $2-x = 1.77(1)$ of Fe, $x = 0.23(1)$ of Al, a representative spectrum is shown in figure 5.1 (top). XRF was performed also for samples encapsulated in silica; however, due to overlapping peaks of Al (K_α at 1.486 keV) and Si (K_α at 1.740 keV) in the XRF spectrum, the composition cannot be determined accurately. Therefore, the formula obtained for bare nanoparticles was assumed to be the same for magnetic cores of all examined samples and was used for all calculations related to the relaxometric experiments. The overview of atomic percents of Fe, Al and Si in the samples determined from XRF analysis is given in table 5.1. The overlapping peaks of Si and Al in coated samples are demonstrated for ε-FeAl-s21 in figure 5.1 (bottom), where also the decrease in intensity of Fe peaks is observable due to augmented photon scattering in the silica coating. Furthermore, 2 % of Si was found also in the bare sample, as apparent from figure 5.1, which might be attributed to residual silica admixtures from the original silica template (the possibility of incorporation of Si into the crystal structure of the phase is tentatively disregarded).

Table 5.1: Atomic percent of Fe, Al and Si in the samples determined from XRF spectra

	atomic percent [%]		
	Fe	Al	Si
ε-FeAl-bare	86.7(7)	11.4(1)	1.9(7)
ε-FeAl-s06	45.4(5)	6.2(4)	48.4(4)
ε-FeAl-s10	29.1(3)	5(1)	66.4(8)
ε-FeAl-s17	17.4(4)	3(1)	79(1)
ε-FeAl-s21	9.0(1)	2.5(3)	88.4(2)

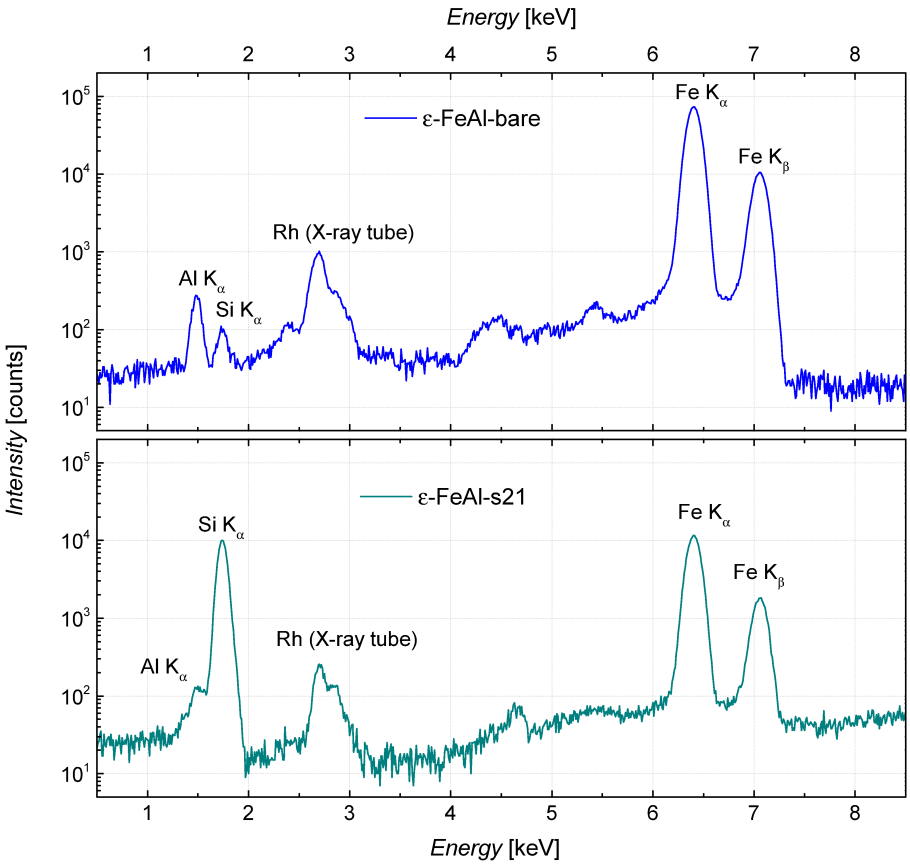

Figure 5.1: XRF spectra of bare nanoparticles (top) and nanoparticles coated with the thickest layer of silica - sample ε-FeAl-s21. The intensity is given in the logarithmic scale. The increase in intensity of Si K_α peak in the coated sample is obvious; concurrently, the intensity of Fe peaks decreases.

5.1.2 X-ray powder diffraction

The phase purity of the bare sample was confirmed by XRPD, where the major phase with $Pna2_1$ symmetry was derived from the ε-Fe_2O_3 structure; no convincing contribution of other crystalline phases of Fe_2O_3 or any other admixtures was found. In the Rietveld analysis, aluminium atoms were presumed to occupy exclusively tetrahedral sites; this presumption was later confirmed by Mössbauer spectroscopy. Figure 5.2 depicts the diffractograms of the sample of bare nanoparticles before any coating methods were introduced, and of samples encapsulated in silica. Apparently, a broad peak of amorphous silica expands in the range of $2\Theta \approx 15-40°$ with increasing thickness of the silica coating (see table 1). Lattice parameters, volume of the elementary cell and the volume per formula unit are summarised in table 5.2.

No verifiable influence of silica coating on lattice parameters or the volume of elementary cell was observed, which is in agreement with our previous study on ε-Fe_2O_3 (Kubíčková et al., 2016).

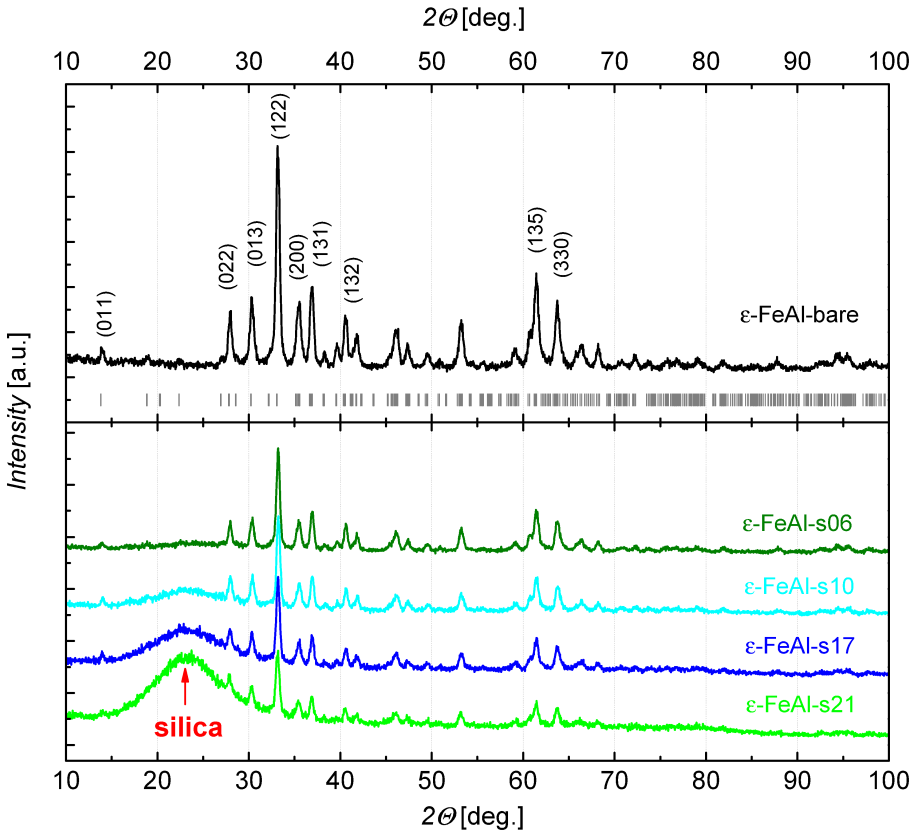

Figure 5.2: Top: XRPD pattern of bare nanoparticles with Miller indices assigned to selected peaks, grey vertical lines indicate peak positions of refined structure; bottom: XRPD patterns of silica-coated samples ordered according to the thickness of silica coating — the amount of silica increases from top to bottom.

Table 5.2: Lattice parameters, volume of the elementary cell and volume rescaled to the formula unit (number of formula units per elementary cell $Z = 6$) refined from XRPD patterns for samples of bare nanoparticles and those encapsulated in silica.

Sample	a [Å]	b [Å]	c [Å]	V [Å^3]	V/Z [Å^3]
ε-FeAl-bare	5.0757(4)	8.7444(7)	9.4243(6)	418.29(5)	52.286(6)
ε-FeAl-s06	5.0767(4)	8.7427(8)	9.4245(7)	418.30(6)	52.287(8)
ε-FeAl-s10	5.0763(5)	8.7468(8)	9.4278(8)	418.61(6)	52.326(8)
ε-FeAl-s17	5.0761(6)	8.746(1)	9.4268(9)	418.51(8)	52.31(1)
ε-FeAl-s21	5.0740(9)	8.747(2)	9.427(1)	418.4(1)	52.30(2)

5.1.3 Mössbauer spectroscopy

The information on hyperfine fields and orientations of the local magnetic moments were derived from the ^{57}Fe Mössbauer spectra of uncoated bare nanoparticles by considering the *core-shell model* (Bødker et al., 1994; Coey, 1971), which assumes

an essentially collinear ordering of the moments in the core and a high level of disorder in the surface shell of the particles. The same isomer shifts for the corresponding components in the shell and in the core were supposed, along with a noncollinear canting of the spins in the shell.

Mössbauer spectra of both ε-Fe_2O_3 and ε-$Fe_{1.77}Al_{0.23}O_3$ with the decomposition to the contributions of core and shell for all non-equivalent cation sites is depicted in figure 5.3; the results of isomer shift, quadrupole splitting and hyperfine magnetic field on ^{57}Fe nuclei are given in table 5.4.

When compared to the Mössbauer spectra of ε-Fe_2O_3 nanoparticles, the spectra of ε-$Fe_{1.77}Al_{0.23}O_3$ evince broadening of spectral lines due to wider hyperfine field distribution caused by the presence of aluminium atoms in the immediate surroundings of the ^{57}Fe nuclei. From the decrease in intensity of the Fe_T component it is apparent that Al atoms occupy preferably tetrahedral sites. The ratio of intensities of individual site components $Fe_{D01} : Fe_{D02} : Fe_{RO} : Fe_T$ is $1 : 1 : 1 : 0.51(3)$, implying the concentration of Al in the tetrahedral site $x = 0.24(1)$ per formula unit ε-$Fe_{2-x}Al_xO_3$ (when the same value of f-factor for all sites is assumed) and verifying thus the results of the XRF analysis. Quadrupole shifts in the core Fe_{D01}, Fe_{D02} and Fe_T sites were slightly influenced by the difference in ionic radii of Al with respect to Fe (ionic radii $Fe^{3+} \sim 0.645$ Å vs $Al^{3+} \sim 0.535$ Å at octahedral sites, and $Fe^{3+} \sim 0.49$ Å vs $Al^{3+} \sim 0.39$ Å at the tetrahedral site; Shannon, 1976). Presently no impact on quadrupole shifts of Fe_{RO} was observed. Furthermore, the substitution led to the lower mean hyperfine magnetic field in the core of ε-$Fe_{1.77}Al_{0.23}O_3$ by 1.0–1.7 T in comparison to ε-Fe_2O_3, which can be interpreted in relation to breaking the superexchange interaction at Fe – O – Fe bonds owing to the introduction of Al into the crystal lattice. However, no change in the mean hyperfine magnetic field of the tetrahedral site was observed. Table 5.3 provides an overview of the nearest tetrahedral sites for each cation site up to 4.000 Å, indicating the extent of how much the aluminium substitution influences the individual sites. An interesting result is that the closest sites to Fe_T are another two Fe_T sites.

Moreover, the occurence of a sextet with great hyperfine splitting in the ε-$Fe_{1.77}Al_{0.23}O_3$ spectrum suggests the presence of 0.8(2) % α-Fe_2O_3 in the sample. The presence of α-Fe_2O_3 was not indicated by the XRPD diffractogram with rather low signal-to-noise ratio, which confirms the higher sensitivity of Mössbauer spectroscopy to minor admixtures of iron compounds. The asymmetric doublet originates from Fe present in the rolled aluminium foil covering the detector of γ radiation.

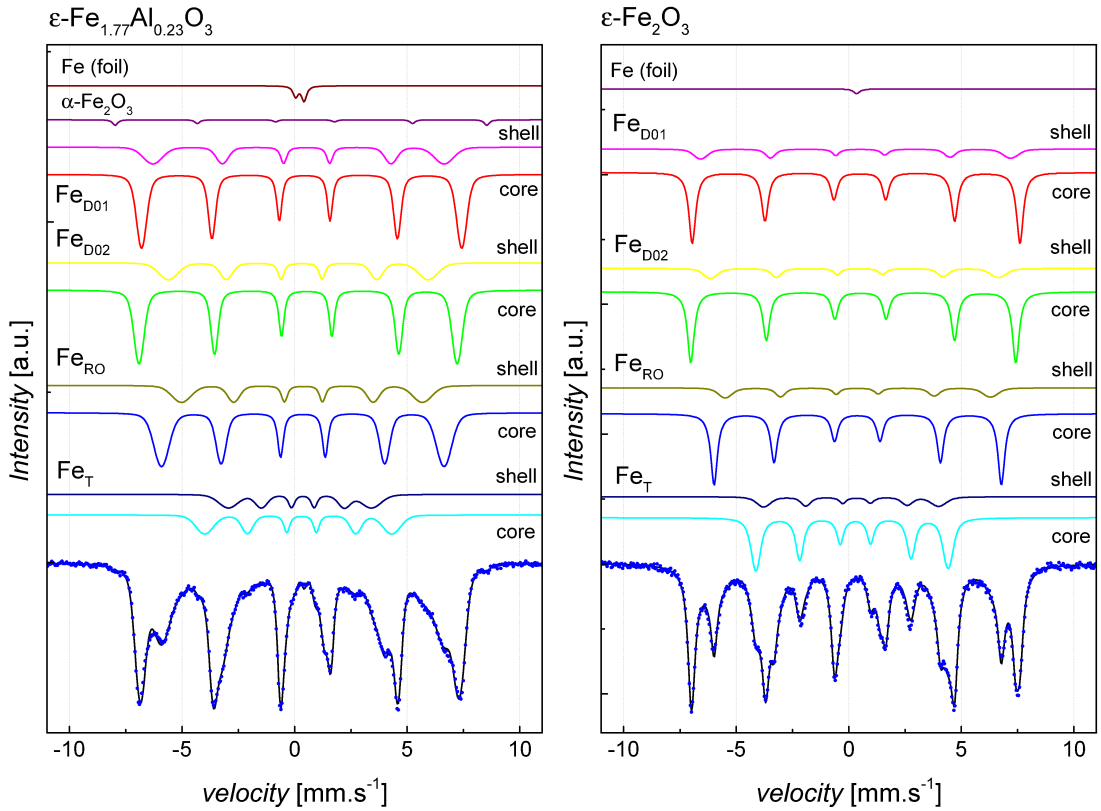

Figure 5.3: Mössbauer spectra of bare ε-$Fe_{1.77}Al_{0.23}O_3$ (left) and ε-Fe_2O_3 (right) nanoparticles, showing the decomposition to the contributions of core and shell for all non-equivalent cation sites. Broader spectral lines, decrease in the intensity of tetrahedral site Fe_T and the presence of α-Fe_2O_3 are apparent in the ε-$Fe_{1.77}Al_{0.23}O_3$ spectrum.

Table 5.3: The distance from the nearest tetrahedral sites Fe_T along with their order (when the neighbouring Fe-sites are sorted by distance from the given site) calculated up to 4.000 Å for each cation site from the structure of ε-Fe_2O_3 published in Gich et al. (2006b).

sites	distance [Å]	order	sites	distance [Å]	order
Fe_T — Fe_T	3.073	1	Fe_{D02} — Fe_T	3.240	4
	3.073	1		3.393	7
Fe_{RO} — Fe_T	3.277	7		3.420	8
	3.413	8		3.438	9
	3.480	10	Fe_{D01} — Fe_T	3.369	6

Table 5.4: Overview of hyperfine parameters obtained from the Mössbauer spectra compared to the parameters of ε-Fe_2O_3 for non-equivalent cation positions of ^{57}Fe in the core and in the shell. The same isomer shifts for the corresponding components in the shell and in the core were supposed, along with a disordered canting of the spins in the shell.

	core				**shell**		
	Isomer shift [mm/s]	**Quadr. shift [mm/s]**	**Hyperf. field [T]**	**Distr. width [mm/s]**	**Isomer shift [mm/s]**	**Quadr. shift [mm/s]**	**Hyperf. field [T]**
ε-FeAl-bare (ε-$Fe_{1.77}Al_{0.23}O_3$)							
Fe_{D01}	0.36(2)	–0.23(3)	44.6(2)	0.18(3)	0.36(2)	–0.23(6)	40.2(6)
Fe_{D02}	0.37(2)	–0.29(3)	43.1(3)	0.38(4)	0.37(2)	–0.22(5)	35.6(5)
Fe_{RO}	0.34(2)	0.01(3)	38.7(3)	0.52(4)	0.34(2)	–0.04(5)	33.0(5)
Fe_T	0.22(2)	–0.17(4)	26.5(3)	0.42(6)	0.22(2)	–0.23(4)	20.3(4)
α-Fe_2O_3 [a]	0.37(5)	–0.18(8)	51.3(5)				
ε-Fe_2O_3							
Fe_{D01}	0.41(3)	-0.17(4)	45.2(2)		0.41(3)	–0.23(7)	42.6(4)
Fe_{D02}	0.36(3)	-0.31(4)	44.8(2)		0.36(3)	–0.08(8)	38.7(4)
Fe_{RO}	0.39(2)	0.01(3)	39.7(2)		0.39(2)	0.06(7)	35.9(4)
Fe_T	0.23(2)	-0.14(3)	26.6(2)		0.23(2)	–0.24(7)	23.1(4)

[a] The admixture of 0.8(2) % α-Fe_2O_3 was present in the examined sample ε-FeAl-bare .

5.1.4 Transmission electron microscopy

Representative bright field transmission electron microscopy (TEM) images of examined samples are shown in figure 5.5. The distribution of nanoparticle sizes in spherical approximation and the thickness of silica coating were determined by statistical analysis described in section 4.2.2 in more detail. Magnetic cores and coated particles as a whole were analysed separately. However, only analysis of samples encapsulated in silica was conducted — in the first approximation, a monomolecular layer of citrate is assumed; moreover, no difference in the size of magnetic cores derived from the same parental suspension as for all other samples was expected.

Parameters derived from log-normal fit 1.6 of the distribution of particle equivalent diameters and from normal fit 4.1 of silica thickness are summarised in table 5.5 along with arithmetic average or volume-weighted average to provide quantitative comparison between both approaches to data on the nanoparticle size presented in literature. Representative histograms of particle equivalent diameters are demonstrated in figure 5.6, the histograms of thickness of silica coating are shown in 5.4.

Both magnetic core and coated particle sizes were well described by log-normal distribution. In line with expectations, no significant difference between the sizes of magnetic cores among all examined samples was found. Both arithmetic mean and median were in good agreement with the mean and median from log-normal fit, the difference between the methods is smaller than the error arisen by approx-

imating the real distribution by log-normal estimate. Nevertheless, the log-normal description provides more precise idea of the shape of particle size distribution in studied ensembles. As can be seen in figure 5.5, the silica shell is very uniform with only limited variation in the thickness, exhibiting smooth surface. Broadened "necks" bridging the gaps between particles visible in some of presented images originate from the character of amorphous silica and most likely emerge during evaporation of suspension on the grid prior to TEM imaging. For all samples, the size of coated particles exceeds the size of magnetic cores enlarged by twice the respective thickness of silica coating. This effect can be ascribed to the fact, that not all clusters formed by magnetic ε-$Fe_{1.77}Al_{0.23}O_3$ nanoparticles in suspension during the encapsulation were successfully disrupted by ultrasound treatment. Consequently, these clusters were embedded in silica as a whole (see figure 5.5), increasing thus the apparent size of coated particles.

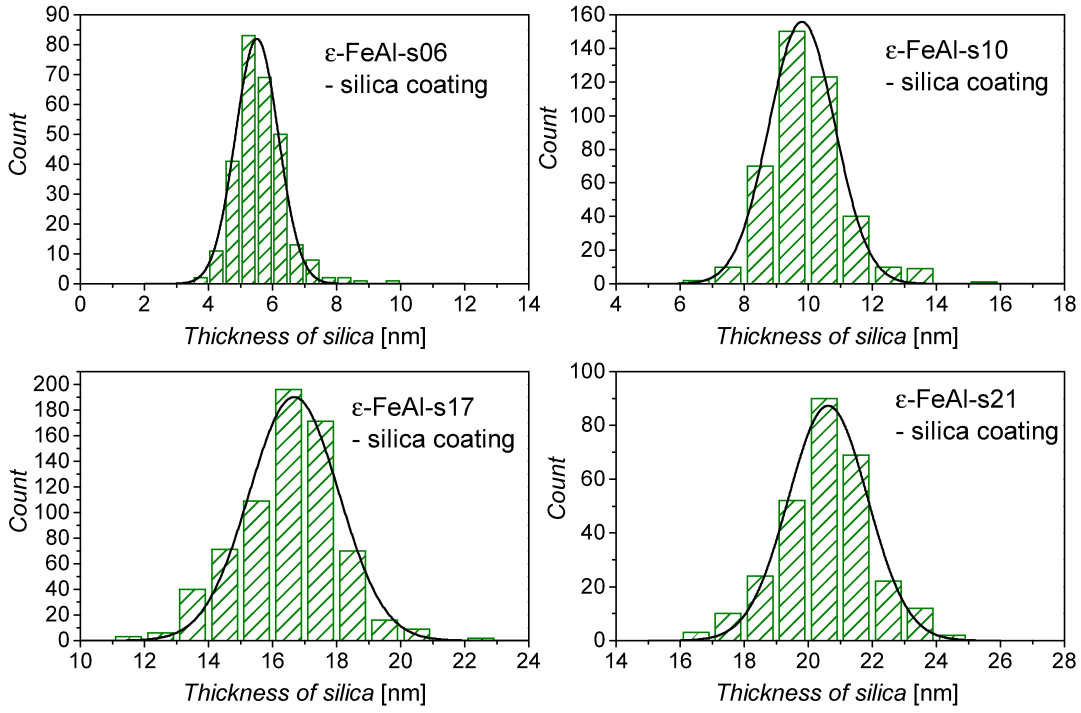

Figure 5.4: Histograms showing the distribution of the thickness of silica coating in encapsulated samples obtained from the analysis of TEM images, fitted by the normal distribution 4.1.

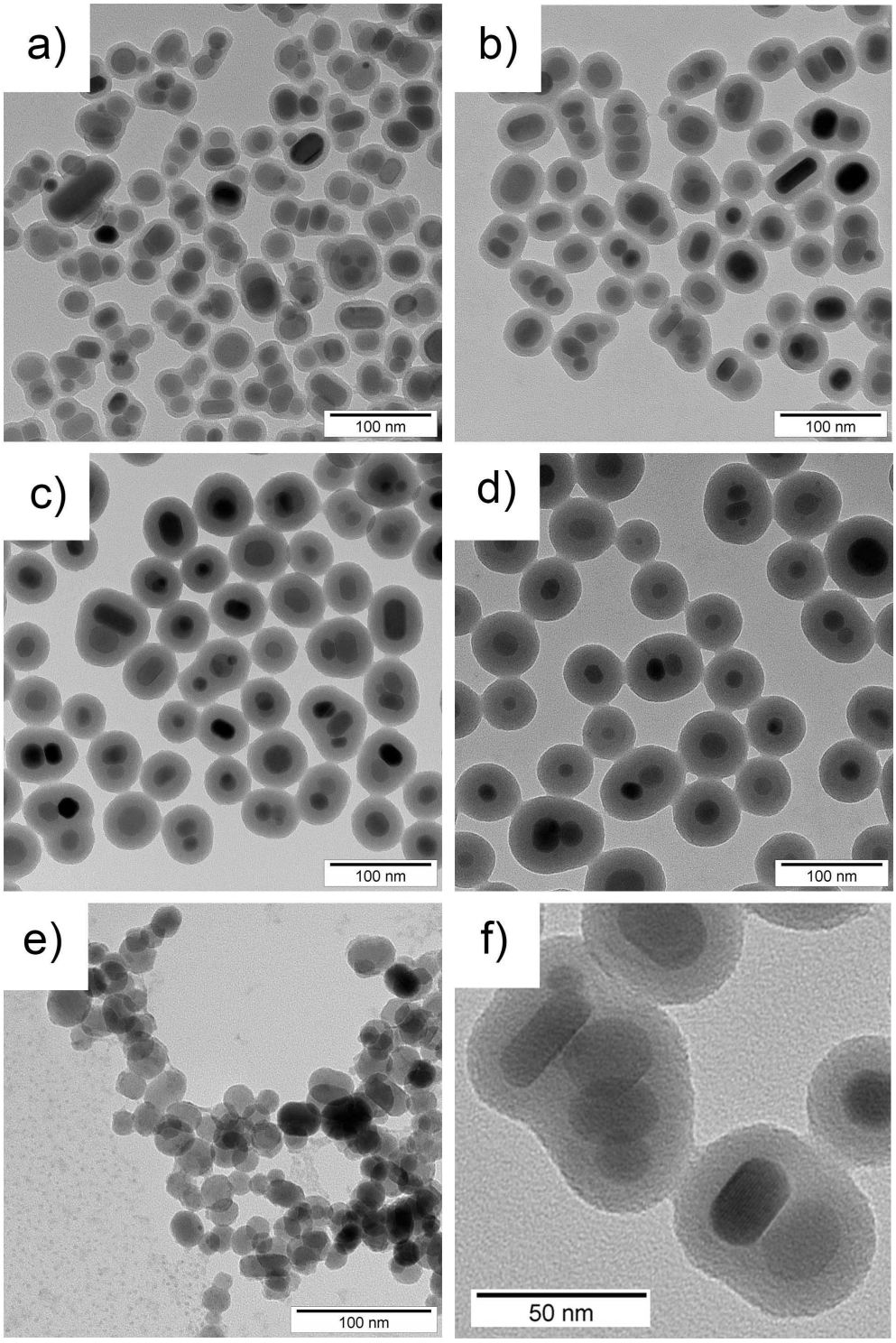

Figure 5.5: TEM bright field images of samples coated with silica and citrate: a) ε-FeAl-s06, b) ε-FeAl-s10, c) ε-FeAl-s17, d) ε-FeAl-s21, e) ε-FeAl-cit, f) detail of particle clusters (ε-FeAl-s10).

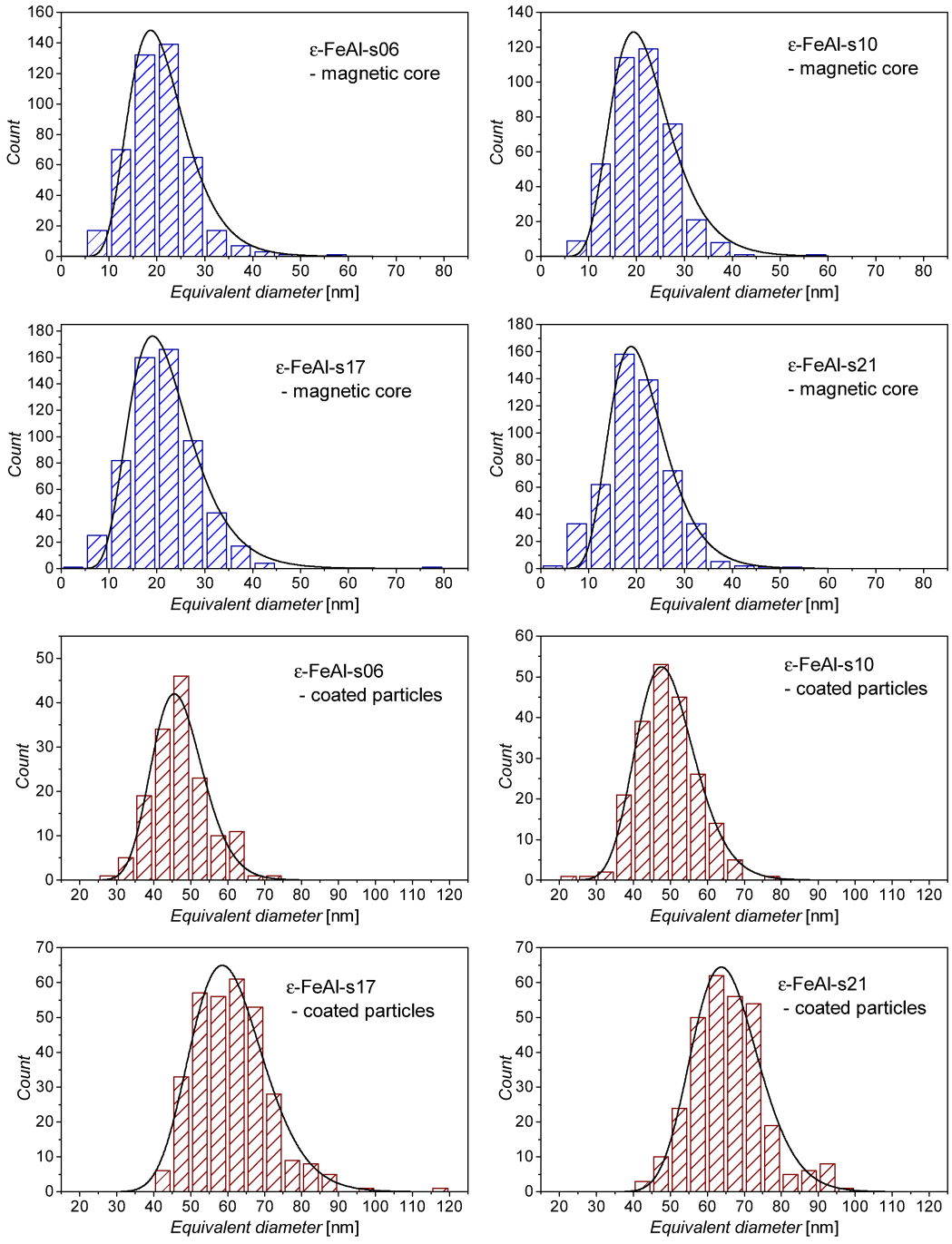

Figure 5.6: Histograms showing the distribution of sizes in the spherical approximation of magnetic cores of the particles (blue) and coated particles as a whole including the clusters (wine red) obtained from the analysis of TEM images of encapsulated samples. The distribution of equivalent diameters was fitted by the log-normal distribution 1.6.

Table 5.5: Various size parameters obtained from TEM image analysis, for more details on the calculation see table 4.1. Log-normal distribution fit: d_0 – median eq. diam., $\overline{d}$ – mean eq. diam., SD – standard deviation of mean, RSD – relative SD, PDI – polydispersity index, $\hat{d}$ – mode eq. diam., $\overline{d}_V$ – volume-weighted mean eq. diam. Arithmetic mean: $\overline{d}_{ar}$ – ar. mean eq. diam., SD_{ar} – SD of ar. mean, $\overline{d}_{V,ar}$ – volume-weighted ar. mean, WD_{ar} – volume-weighted deviation of mean, $d_{0,ar}$ – ar. median eq. diam. Silica thickness: l_0 and σ_g – mean and SD from normal distr., $l_{0,ar}$ and $SD_{l,ar}$ – ar. mean and SD.

	magnetic cores			
	ε-FeAl-s06	ε-FeAl-s10	ε-FeAl-s17	ε-FeAl-s21
log-normal distribution				
d_0 [nm]	21	21	21	21
$\overline{d}$ [nm]	22	22	22	22
SD [nm]	7	7	8	7
RSD	0.31	0.32	0.34	0.30
PDI	0.10	0.10	0.12	0.09
$\hat{d}$ [nm]	23	23	24	23
$\overline{d}_V$ [nm]	29	30	31	28
arithmetic mean				
$\overline{d}_{ar}$ [nm]	21	20	21	21
SD_{ar} [nm]	7	7	6	7
$\overline{d}_{V,ar}$ [nm]	30	27	27	27
WD_{ar} [nm]	14	8	8	9
$d_{0,ar}$ [nm]	19.9	20.0	21.0	20.2
silica thickness				
l_0 [nm]	6	10	17	21
σ_g [nm]	1	2	3	2
$l_{0,ar}$ [nm]	6	10	16	21
$SD_{l,ar}$ [nm]	1	1	2	1
	coated particles			
	ε-FeAl-s06	ε-FeAl-s10	ε-FeAl-s17	ε-FeAl-s21
log-normal distribution				
d_0 [nm]	47	49	60	65
$\overline{d}$ [nm]	47	50	61	66
SD [nm]	7	8	10	9
RSD	0.15	0.17	0.17	0.14
PDI	0.02	0.03	0.03	0.02
$\hat{d}$ [nm]	48	50	62	66
$\overline{d}_V$ [nm]	50	54	66	70
arithmetic mean				
$\overline{d}_{ar}$ [nm]	47	49	61	66
SD_{ar} [nm]	8	8	10	10
$\overline{d}_{V,ar}$ [nm]	51	53	66	70
WD_{ar} [nm]	8	8	12	11
$d_{0,ar}$ [nm]	47.1	48.8	60.6	64.8

5.1.5 Dynamic light scattering

DLS was measured for all coated samples and compared to the equivalent diameters of coated particles obtained from TEM. The main objective was to determine the hydrodynamic diameter of the particles and therethrough to assess the thickness of water layer carried with the particle in the suspension. Results of DLS analysis are summarised in table 5.6.

DLS evidences the colloidal stability of aqueous suspensions of nanoparticles encapsulated in silica and those stabilized by citrate. The mean obtained from DLS is intensity-weighted, and number and volume means are acquired by its recalculation with some presumptions (sphericity of particles, known optical properties), therefore are determined with lower precision. Bearing that in mind, the comparison of number and volume means of coated particles from DLS and TEM is arguable. Nevertheless, number means approximately correspond with each other, suggesting that the water layer carried with the particles counts up to a few molecular layers (the size of water molecule $\approx 0.28\,\mathrm{nm}$; D'Arrigo, 1978).

Table 5.6: Hydrodynamic diameter of particles obtained from DLS and the thickness of water layer from comparison of DLS and TEM volume-weighted and number means. d_Z – Z-average (intensity-weighted harmonic mean), PDI_{DLS} – polydispersity index given by Zeta Sizer software (rescaled coefficient of quadratic term of a polynomial fit to the time dependence of logarithm of correlation function $\ln G_{DLS}(t)$), $\overline{d}_{V,DLS}$ – volume-weighted mean size, $\overline{d}_{DLS}$ – number-weighted mean size

Sample	d_Z [nm]	PDI_{DLS}	$\overline{d}_{V,DLS}$ [nm]	$\overline{d}_{DLS}$ [nm]	$\frac{\overline{d}_{V,DLS}-\overline{d}_{V,TEM}}{2}$ [nm]	$\frac{\overline{d}_{DLS}-\overline{d}_{TEM}}{2}$ [nm]
ε-FeAl-s06	72.0	0.10	60.1	47.2	4.8	0.03
ε-FeAl-s10	79.0	0.12	65.1	50.5	5.7	0.44
ε-FeAl-s17	85.8	0.08	75.4	61.1	4.5	0.02
ε-FeAl-s21	102.8	0.08	92.0	74.1	11.1	4.2
ε-FeAl-cit	44.8	0.22	39.1	24.6	4.6	1.3

5.1.6 Magnetic properties

The hysteresis loops of bare nanoparticles and the ones encapsulated in silica measured at 300 K are depicted in figure 5.7. The specific magnetization of the coated samples is substantially lower in comparison to the specific magnetization of bare particles due to the presence of large amount of diamagnetic component. The values of specific magnetization at 5 T were used to plot the dependence of relative magnetization, i.e. the magnetization of the sample divided by magnetization of bare cores, on the thickness of silica coating, which also denotes the mass fraction of magnetic component in the samples (see figure 5.10 left).

The hysteresis loops of ε-$Fe_{1.77}Al_{0.23}O_3$ and ε-Fe_2O_3 bare nanoparticles are depicted in figure 5.8. The assumption that substituting diamagnetic Al^{3+} cations for a fraction of Fe^{3+} cations would lead to the increase in magnetization of the particles with respect to ε-Fe_2O_3, was hereby verified. Nonetheless, the coercive field was reduced by almost 30 % (1.48 T vs. 2.1 T in ε-Fe_2O_3).

From the comparison of zero-field cooled (ZFC)/field cooled (FC) curves of ε-$Fe_{1.77}Al_{0.23}O_3$ and ε-Fe_2O_3 nanoparticles in figure 5.9, it is apparent that the magnetization transitions typical for ε-Fe_2O_3 are suppressed by introducing Al atoms into the crystal lattice. The difference in magnitude of magnetization originates in diverse conditions during measurement — the sample ε-FeAl-bare was demagnetized prior to the measurement and examined in magnetic field 2 mT, while the sample of ε-Fe_2O_3 was already magnetized and examined in 10 mT.

The temperature dependence of specific magnetization of bare particles obtained in 0.5 T is shown in the right panel of figure 5.10, to demonstrate the behaviour of magnetization in one of the examined fields and in the range of temperatures used for relaxometric experiments.

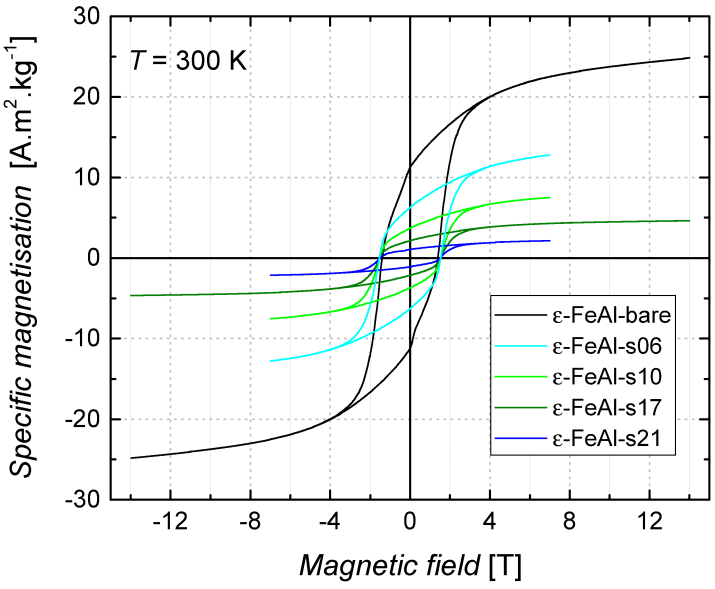

Figure 5.7: Hysteresis loops of ε-$Fe_{1.77}Al_{0.23}O_3$ nanoparticles (bare and encapsulated in silica) at 300 K. The values of specific magnetization at 5 T were further used to plot the graph of dependence of magnetization on the thickness of silica coating, see figure 5.10 left.

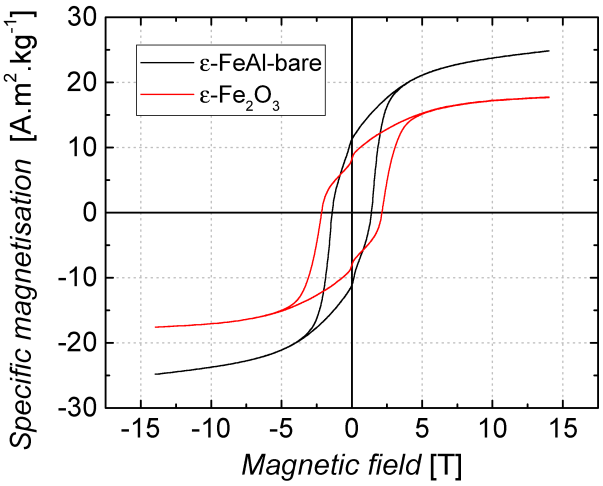

Figure 5.8: Comparison of hysteresis loops of ε-FeAl-bare and ε-Fe_2O_3 nanoparticles at 300 K. The magnetization increased due to the substitution of Al for a fraction of Fe atoms; moreover, the coercive field decreased.

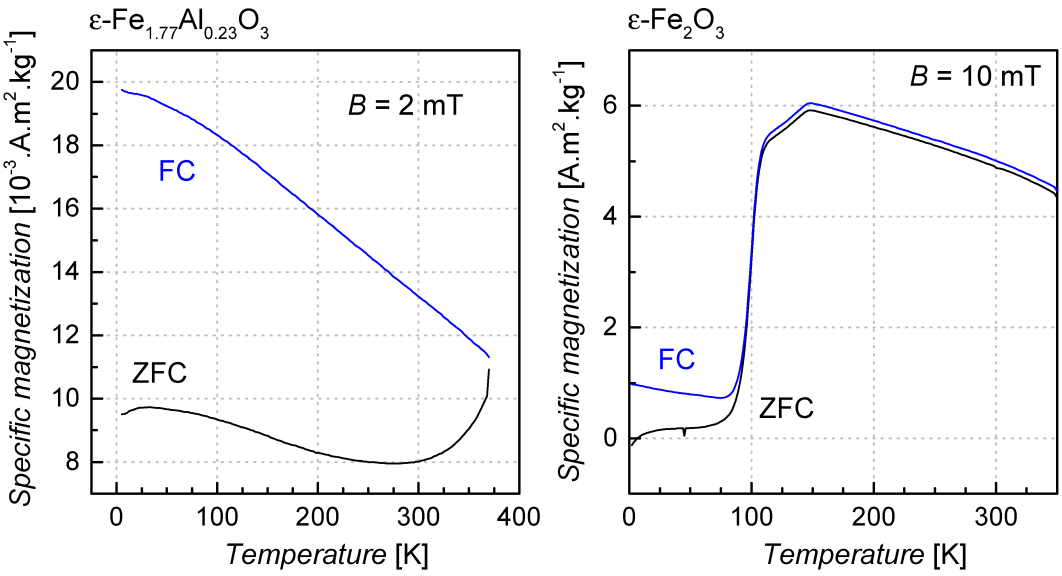

Figure 5.9: ZFC/FC curves of ε-$Fe_{1.77}Al_{0.23}O_3$ (sample ε-FeAl-bare ; left) and ε-Fe_2O_3 (right) nanoparticles. Note the different magnetization scales for left and right graph: the difference in magnetization magnitude originates in different measurement conditions. Apparently, the magnetization transitions typical for ε-Fe_2O_3 are suppressed by introducing Al atoms into the crystal lattice.

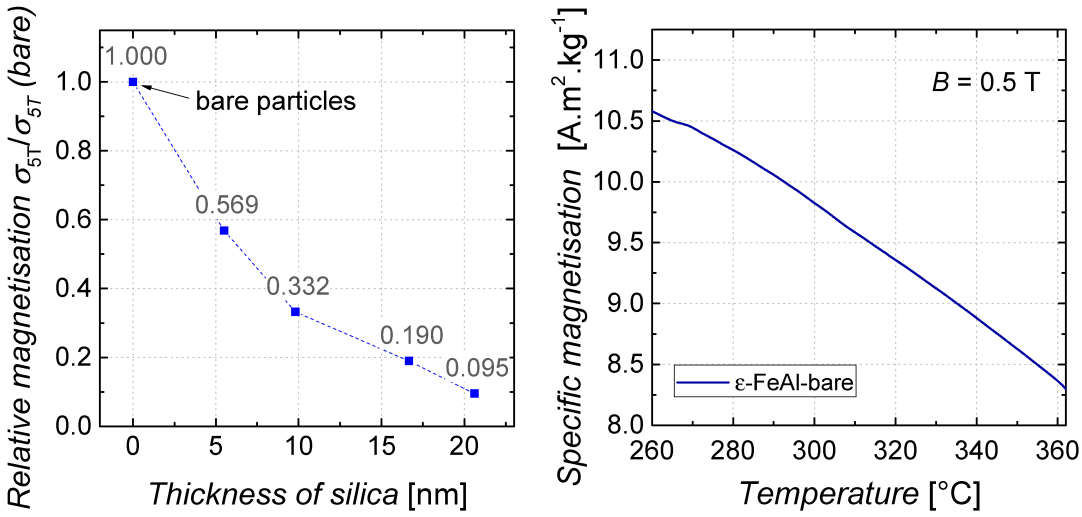

Figure 5.10: Left: Specific magnetization values of encapsulated samples at 5 T related to the specific magnetization of the bare sample, as depending on the respective thickness of silica coating. The numbers above data points denote the mass fraction w of the magnetic component ε-$Fe_{1.77}Al_{0.23}O_3$ in each sample; the value $1-w$ would then denote the mass fraction of the diamagnetic component $SiO_x(OH)_y$. Right: Temperature dependence of specific magnetization of the bare sample in 0.5 T.

5.2 Relaxivity

Five samples in suspensions were used for relaxometric studies: nanoparticles encapsulated in silica (ε-FeAl-s06, ε-FeAl-s10, ε-FeAl-s17, ε-FeAl-s21) and coated with citrate (ε-FeAl-cit).

5.2.1 Concentration of suspensions

The concentration of suspensions of nanoparticles prepared as described in section 4.1.2 was determined by the ICP-MS, the results are summarised in table 5.7. The relative error in determination the concentration η_c was included in the relaxivity error calculation. These suspensions were used to prepare 5 subsamples for further relaxometric experiments. The most concentrated subsample (denoted as SS1 in tab. 5.7) of each suspension of silica coated nanoparticles was intended to be diluted to 0.60 mM concentration of ε-$Fe_{1.77}Al_{0.23}O_3$, i.e. 1.06 mM concentration of iron atoms according to preliminary chemical analysis; however, the concentration was later determined with higher precision by ICP-MS giving slightly different values, see the final concentrations in tab. 5.7. The citrated sample was diluted in "suspension : water" ratio as 1 : 9 to obtain SS1 since the relaxometric measurements were performed prior to the ICP-MS. The other subsamples were then prepared by diluting in "SS1 : water" ratios 2 : 1 (Fe ∼ 0.71 mM), 1 : 2 (Fe ∼ 0.35 mM), 1 : 5 (Fe ∼ 0.18 mM) and 1 : 11 (Fe ∼ 0.09 mM). All plots of the transversal relaxivity in the thesis are related to the concentration of Fe, not ε-$Fe_{1.77}Al_{0.23}O_3$.

Table 5.7: Concentration of Fe in suspensions prepared by the method described in section 4.1.2 and its relative deviation η_c, which were determined from ICP-MS. The molar concentration c of Fe and ε-$Fe_{1.77}Al_{0.23}O_3$ (denoted "f.u.") was then calculated and used to prepare subsample SS1 of given molar concentration c_{SS1}.

Sample	Fe [mg.g^{-1}]	η_c	c(Fe) [mM]	c(f.u.) [mM]	c_{SS1}(Fe) [mM]	c_{SS1}(f.u.) [mM]
ε-FeAl-cit	0.272(6)	0.021	4.871	11.065	0.487	0.275
ε-FeAl-s06	0.712(5)	0.007	12.756	2.752	1.026	0.580
ε-FeAl-s10	0.81(2)	0.026	14.461	7.207	0.914	0.516
ε-FeAl-s17	1.09(4)	0.034	19.586	12.076	0.947	0.557
ε-FeAl-s21	1.194(4)	0.003	21.375	8.170	0.938	0.530

5.2.2 Magnetic field dependence

The results of the transversal relaxivity r_2 measured at 23 °C and 40 °C for various magnetic fields are summarised in figures 5.11 and 5.13. The error bars were calculated according to error propagation rules to include the following sources: the relative deviation of sample concentration, the error of temperature determination (rough estimate differing among the instruments and temperatures taking the respective hardship of the temperature stabilisation into consideration) recalculated relatively from the temperature dependence of r_2, and the error of linear regression when calculating r_2 from concentration dependence of the relaxation rate R_2.

When excluding the experimental points for 0.94 T at 23 °C and 1.5 T at 40 °C, which were highly influenced by the difficulties in temperature control (for more details see section 4.3.1), exponential rise to maximum $r_2 = \alpha - \beta e^{-\xi B}$ provides a satisfactory fit of the experimental data. Therefore, this formula was applied to provide a guideline for the eye in figures 5.11 and 5.13. The instrumental weighting was employed in the fitting procedure. The exponential factor ξ roughly approaches the value $\sim 0.3\,\mathrm{T}^{-1}$ for silica coated samples, while it is lower for the citrated sample ($\sim 0.2\,\mathrm{T}^{-1}$) for both examined temperatures.

To provide comparison with literature on relaxometry which employs field cycling methods of measuring relaxivities r_1, the dependence of relaxivity on Larmor frequency of ^{1}H in the logarithmic scale is plotted in figures 5.12 and 5.14.

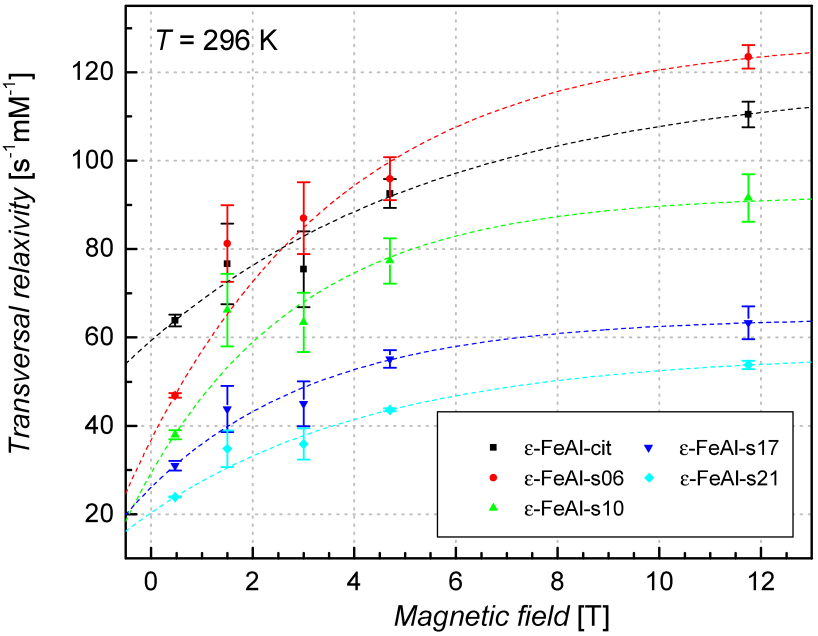

Figure 5.11: Magnetic field dependence of r_2 relaxivity at 23 °C (296.15 K). The data were fitted by equation $r_2 = \alpha - \beta e^{-\xi B}$, the fit was plotted as a dashed line to provide a guideline to the eye.

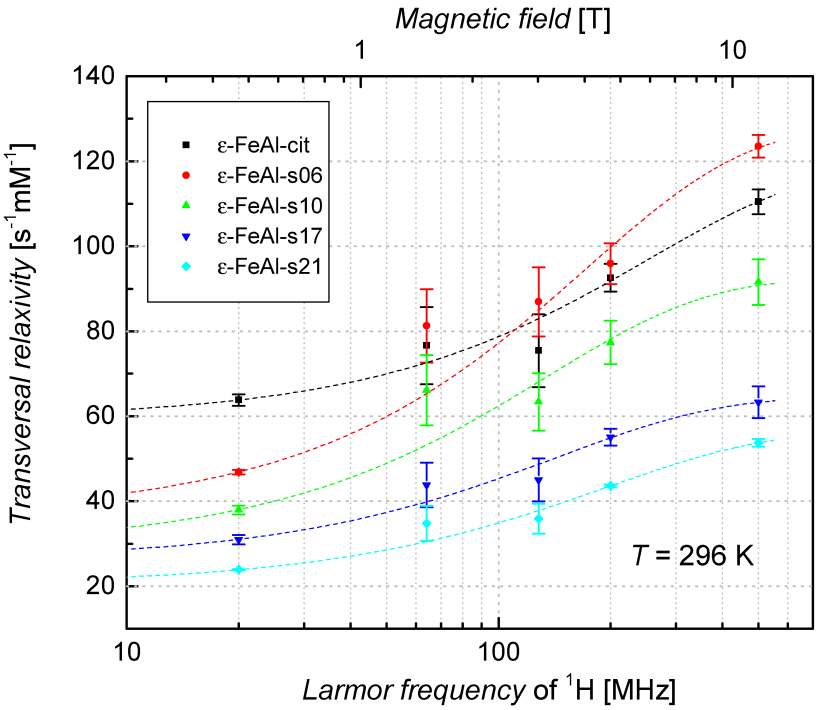

Figure 5.12: Dependence of r_2 relaxivity on Larmor frequency of ^{1}H in respective magnetic fields at 23 °C (296.15 K). The frequency axis is in the logarithmic scale according to the convention used widely in literature on relaxometry to facilitate comparison.

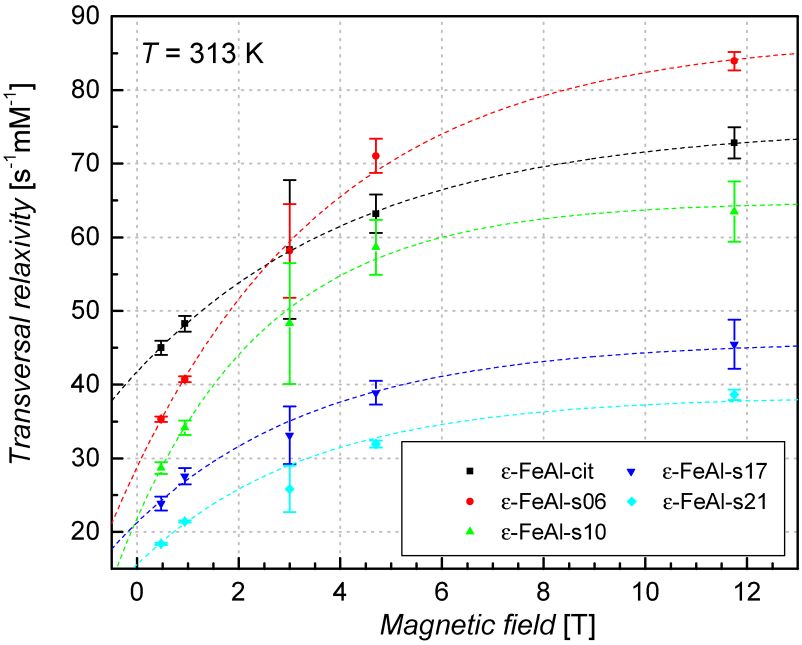

Figure 5.13: Magnetic field dependence of r_2 relaxivity at 40 °C (313.15 K). The data were fitted by equation $r_2 = \alpha - \beta e^{-\xi B}$, the fit was plotted as a dashed line to provide a guideline to the eye.

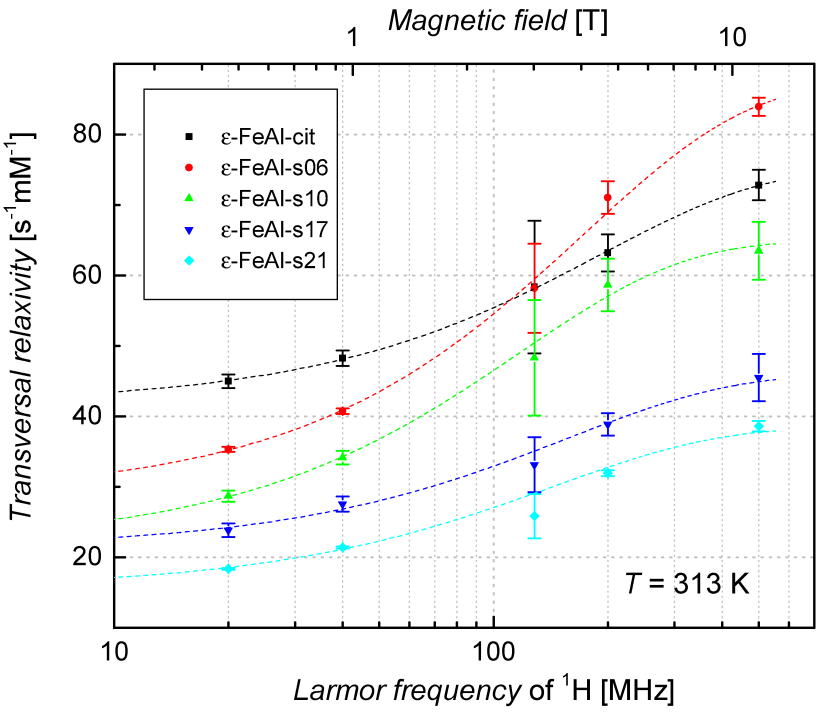

Figure 5.14: Dependence of r_2 relaxivity on Larmor frequency of ^{1}H in respective magnetic fields at 40 °C (313.15 K). The frequency axis is in the logarithmic scale according to the convention used widely in literature on relaxometry to facilitate comparison.

Interestingly, the relaxivity of the citrated sample ε-FeAl-cit is not solely rescaled in relation to silica coated samples, as one would expect simply considering the increase of distance of water protons from the magnetic core of the particles with the increase in thickness of the coating. In contrast, its behaviour considerably differs — even though both silica and citrate coated samples follow approximately the relation $r_2 = \alpha - \beta e^{-\xi B}$, the relaxivity of ε-FeAl-cit is lower in lower magnetic fields than the one of ε-FeAl-s06 and higher in higher fields, both curves intercept at $\sim$ 2.5 T for both examined temperatures. This result suggests that the mechanism of interaction of water protons varies with the type of coating/stabilization and that there is probably another contribution to relaxivity related to the silica coating in lower magnetic fields, which is for higher fields outweighed by smaller distance from the magnetic cores in the case of citrated particles. Nevertheless, it is obvious that the surface modification of particles affects their transversal relaxivity and has to be considered while comparing different contrast agents.

5.2.3 Temperature dependence

The temperature dependence of r_2 relaxivity was measured at subsamples SS1s in two magnetic fields: 0.47 T and 11.75 T, the results are shown in figures 5.15 and 5.17. The error bars were calculated according to error propagation rules to include the following sources: the relative deviation of sample concentration, the error of temperature determination (from the difference in temperature right before and after the measurement) and the error of the fit by equation 4.2 when calculating

the T_2 relaxation time. However, the error bars were relatively small and worsened the lucidity of the figures so they were excluded from the plots.

Under the assumption of the Arrhenius-type of behaviour of the self-diffusion coefficient of water, the dependence of r_2 on temperature can be described by the following expression

$$r_2 = r_{20}^{*} e^{\frac{E_a}{RT}}, \tag{5.1}$$

with E_a being the activation energy related to diffusion. The natural logarithm of r_2 was plotted as a function of $1/RT$ to verify the assumption, alternatively to find out whether any other process activated by temperature occurs. The plots are shown in figures 5.16 and 5.18. Apparently, the temperature dependence of r_2 of citrated sample can be rationalized by the Arrhenius behaviour of water diffusion in the examined range of temperatures. However, this is not the case for nanoparticles encapsulated in silica, where the Arrhenius type of behaviour observed at lower temperatures is distorted at higher temperatures, suggesting that another process related to the silica coating is manifested. The lines provided as guidelines to the eye in the graphs 5.15 – 5.18 were obtained by fitting the data as described in section 5.2.4.

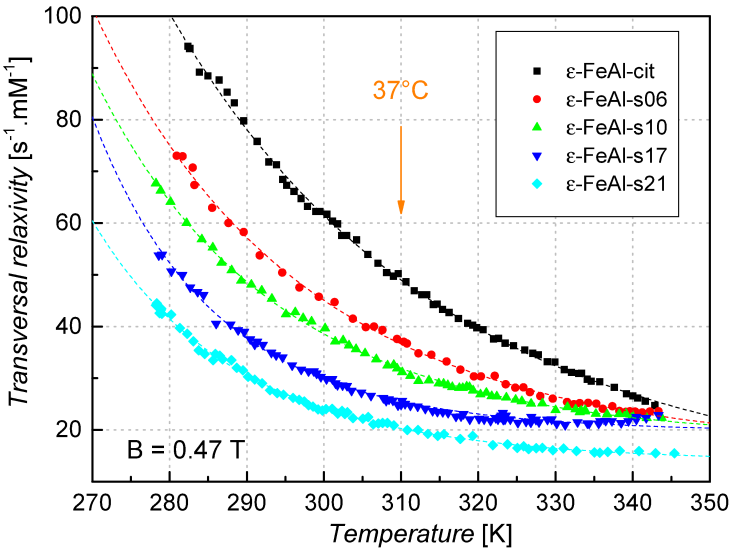

Figure 5.15: The temperature dependence of transversal relaxivity r_2 at 0.47 T. The data were fitted with regard to the temperature dependence of magnetization and the Arrhenius-type of behaviour of the self-diffusion coefficient in the MAR. However, the dashed curves of the fit are provided rather to be guidelines for the eye due to troublesome interpretation of parameters of the fit. The temperature of the human body 37 °C is highlighted in the graph.

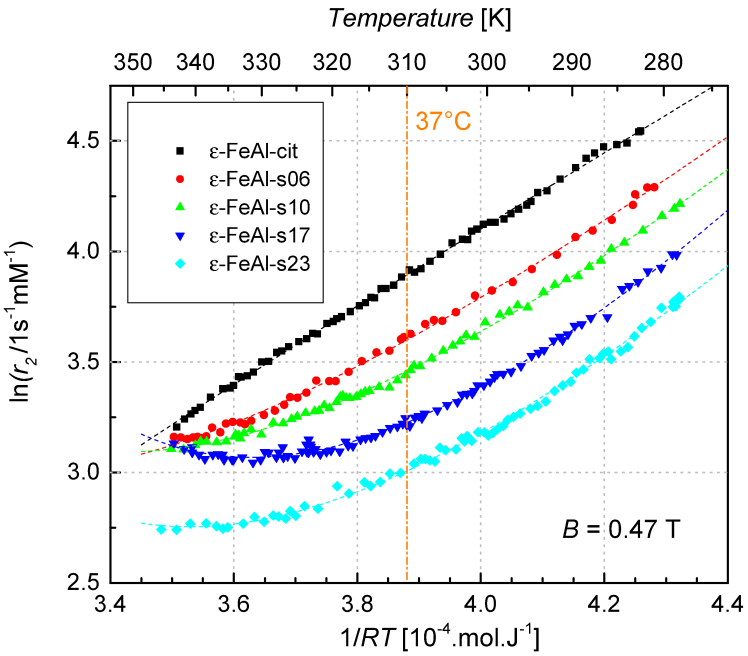

Figure 5.16: Graph showing the dependence of $\ln r_2$ on $1/RT$ at 0.47 T. The data were fitted with regard to the temperature dependence of magnetization and the Arrhenius-type of behaviour of the self-diffusion coefficient in the MAR. However, the dashed curves of the fit are provided rather to be guidelines for the eye due to troublesome interpretation of parameters of the fit. The temperature of the human body 37 °C is highlighted in the graph.

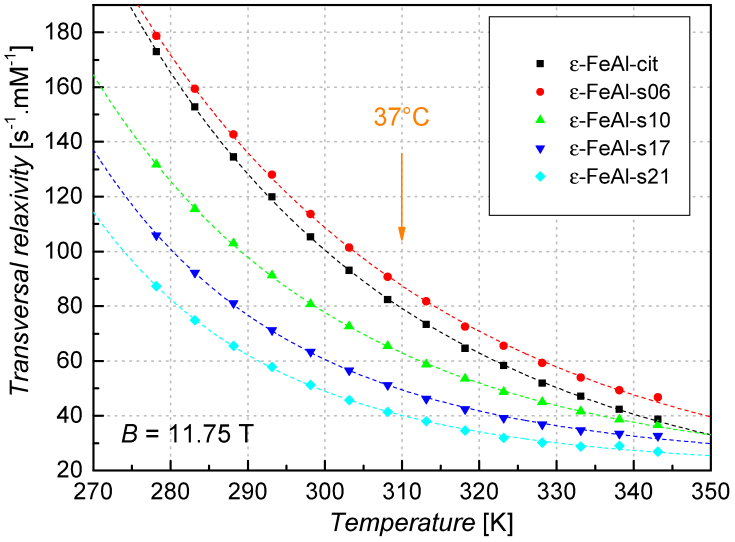

Figure 5.17: The temperature dependence of transversal relaxivity r_2 at 11.75 T. The data were fitted with regard to the temperature dependence of magnetization and the Arrhenius-type of behaviour of the self-diffusion coefficient in the MAR. However, the dashed curves of the fit are provided rather to be guidelines for the eye due to troublesome interpretation of parameters of the fit. The temperature of the human body 37 °C is highlighted in the graph.

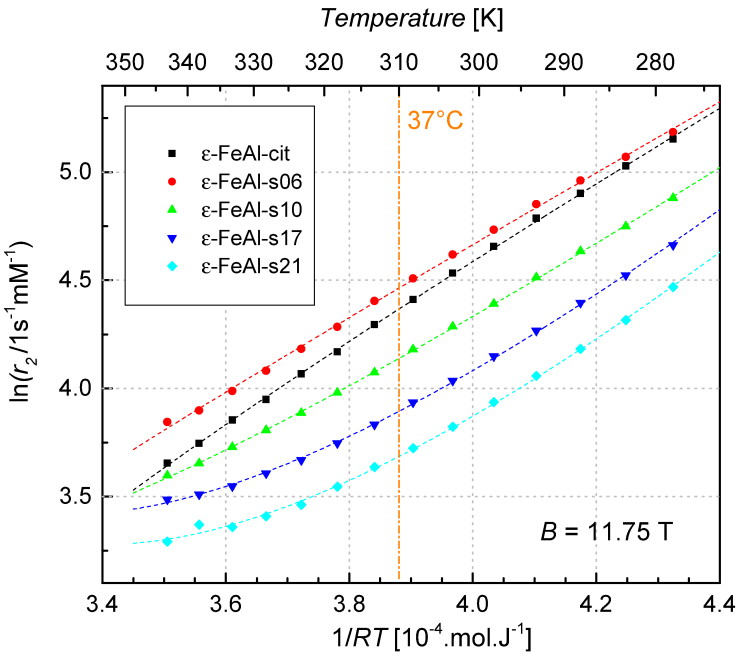

Figure 5.18: Graph showing the dependence of $\ln r_2$ on $1/RT$ at 11.75 T. The data were fitted with regard to the temperature dependence of magnetization and the Arrhenius-type of behaviour of the self-diffusion coefficient in the MAR. However, the dashed curves of the fit are provided rather to be guidelines for the eye due to troublesome interpretation of parameters of the fit. The temperature of the human body 37 °C is highlighted in the graph.

To ascertain whether the process manifesting in silica coated samples at higher temperatures is reversible, the temperature dependence of r_2 was then measured not only during heating, but also during subsequent cooling. The irreversibility of the process was confirmed for all checked samples and both magnetic fields, as demonstrated on sample ε-FeAl-s17 in figures 5.19 and 5.20. Moreover, no effect of subsequent ultrasound treatment was found, indicating that the aggregation of particles can be excluded from presumed causes of this unexpected behaviour. Nonetheless, a trial short ultrasound treatment after measurement at 343 K, after heating and before cooling the sample ε-FeAl-s17 at 11.75 T affected considerably the relaxivity – see figure 5.20. Some of the suspensions that underwent the temperature dependence measurement were examined again by means of DLS, and a significant decrease in hydrodynamic diameter of the particles was found (decrease in Z-average for ε-FeAl-s10 from 79 nm to 54 nm, for ε-FeAl-s17 from 86 nm to 76 nm). Finally, the same suspension of ε-FeAl-s10 after heating was inspected by TEM, for representative images see figure 5.21. Surprisingly, the silica coating was almost dissolved, which explains the increase of relaxivity due to considerable decrease of the distance of closest approach for water protons. The dissolution of silica is probably the result of the shift in chemical equilibria in reaction cascade triggered by heating a diluted suspension of nanoparticles in pure deionized water, which favours the dissolution processes. Moreover, it is facilitated by the huge surface of nanoparticles. The precipitates of amorphous silica present in TEM images precipitated probably during preparation of the sample for TEM, no component of this size was observed in suspensions by DLS. The dissolution of silica can explain

the leap in relaxivity at 343 K after the ultrasound treatment depicted in figure 5.20, since the ultrasound might facilitate the desintegration of silica shell of coated particles.

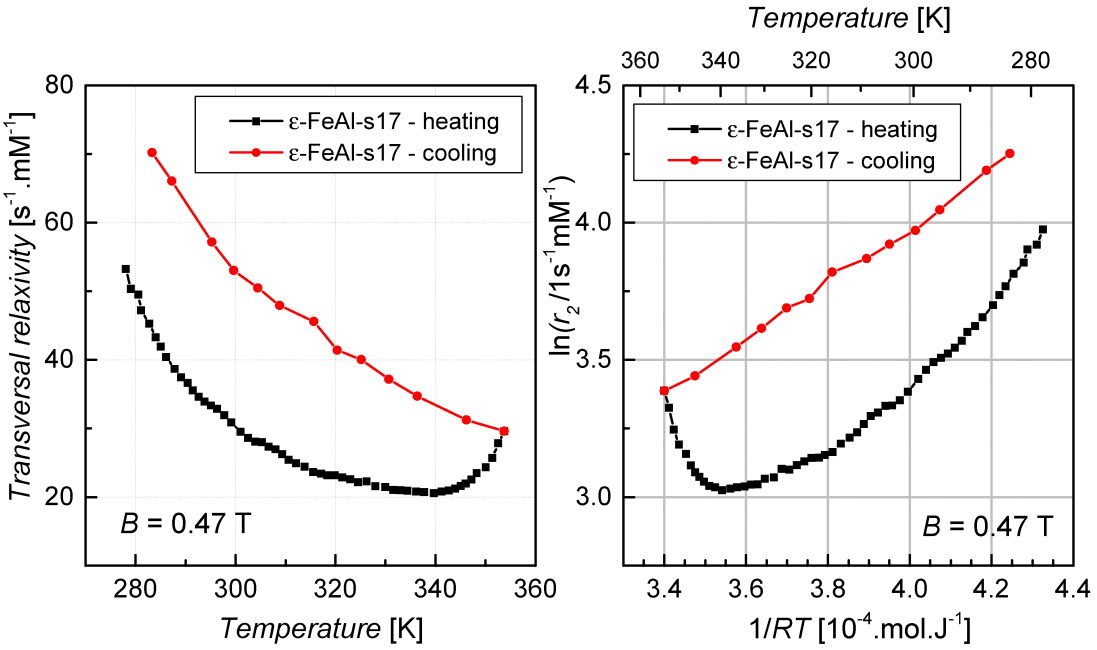

Figure 5.19: Demonstration of the irreversibility of the heat-activated process affecting the relaxivity of the samples encapsulated in silica - shown for ε-FeAl-s17 at 0.47 T.

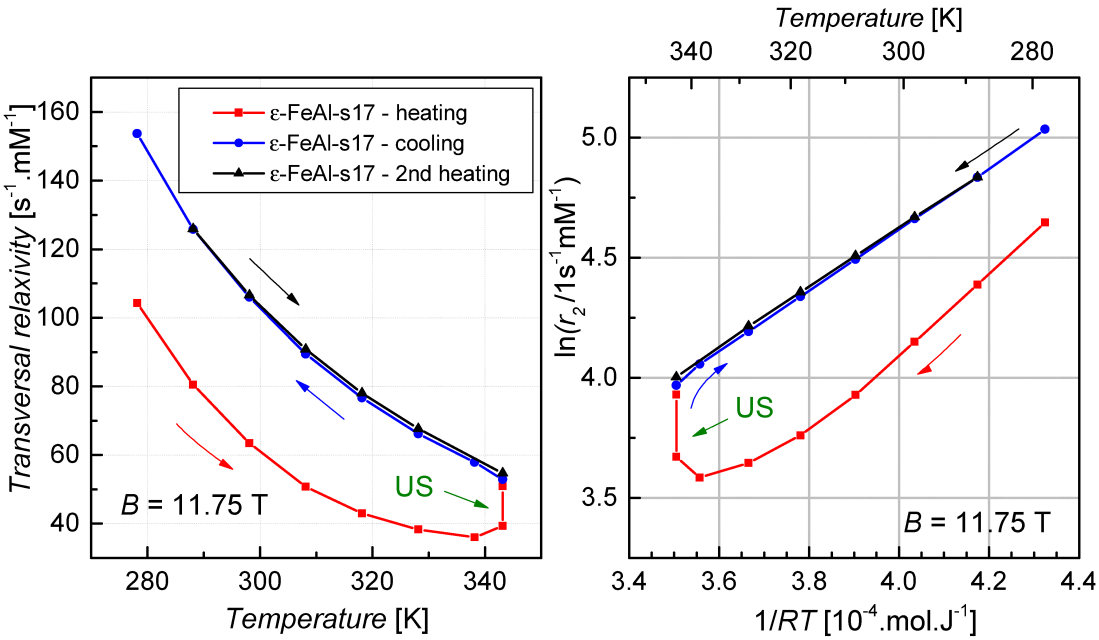

Figure 5.20: Demonstration of the irreversibility of the heat-activated process affecting the relaxivity of the samples encapsulated in silica - shown for ε-FeAl-s17 at 11.75 T. The sample was heated, then cooled down and heated again; after measurement at 343 K before cooling, the sample was treated shortly in the ultrasound bath (green arrow with caption "US").

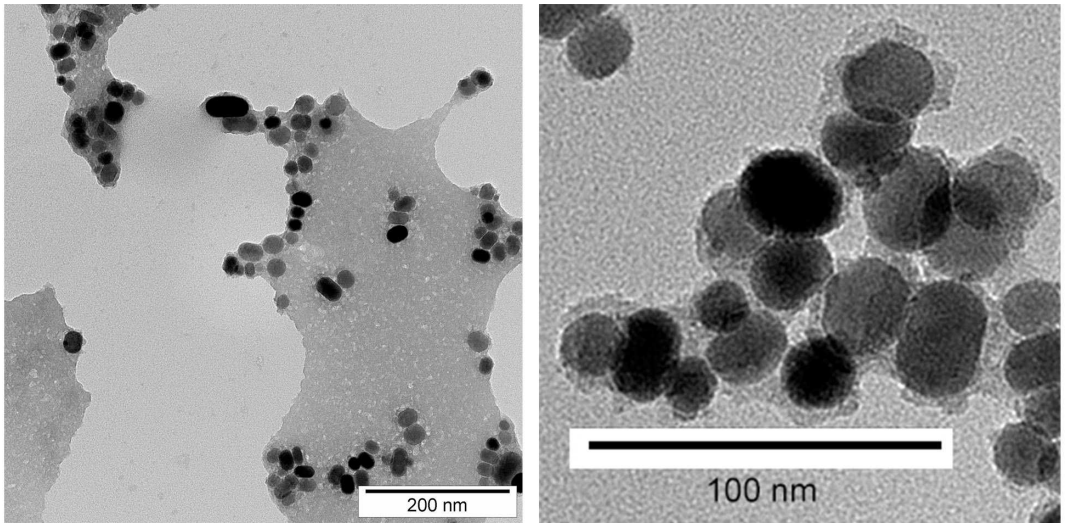

Figure 5.21: The TEM images of ε-FeAl-s10 after the measurement of temperature dependence at 0.47 T - precipitated silica (left) and detail of uncoated particles (right).

5.2.4 Comparison to theoretical models

The experimental results of transversal relaxivity, i.e. the trends and dependence on selected quantities were compared to the teoretical models outlined in section 2.4.2. Following plots are indicative for chosen parameters and available experimental data, not aimed to be comprehensive.

Firstly, to determine the relaxation regime that should be used to interpret the data, the diffusion correlation time τ_D (eq. 2.19) and the Larmor frequency shift at the equator of the particle $\Delta\omega$ (eq. 2.21) were calculated. The median diameter of the coated particles obtained from the log-normal fit and the self-diffusion coefficient of water D were used to obtain τ_D (figure 5.22 left). D was calculated from empirical relation $1/D = 1/(D_0[(T/T_S)-1]^{\zeta})$ used to fit experimental data from literature (Holz et al., 2000), where $D_0 = (15.4 \pm 0.3).10^{-9}\,\mathrm{m^2.s}$, $T_S = (211 \pm 1)\,\mathrm{K}$ and $\zeta = 2.14 \pm 0.03$. The molar mass of ε-$Fe_{1.77}Al_{0.23}O_3$ $M_{\mathrm{mat}} = 153.051\,\mathrm{g.mol^{-1}}$ and the volume per formula unit $52.3\,\text{Å}^3$ ($\nu_{\mathrm{mat}} = 31.50\,\mathrm{cm^3.mol^{-1}}$) were used to detemine the density of the material $\rho_{\mathrm{mat}} = 4.86\,\mathrm{g.cm^{-3}}$ necessary to calculate volume magnetization M.

The Larmor frequency shift for coated nanoparticles was determined by rescaling the shift for bare particles by factor r_c^3/R^3 as it follows from the relation for the dipolar field of particle 2.20, where r_c is the median radius of bare particles and $R = r_c + l$, l being the thickness of silica shell according to TEM (figure 5.22 right).

The condition $\Delta\omega < \frac{1}{\tau_D}$ was fulfilled for all samples in all magnetic fields (figure 5.23 left) (calculated at 300 K), hence the relevant regime of r_2 for examined nanoparticles is the motional averaging regime (MAR) characterised by relation 2.24.

The critical diameter of transition to the static dephasing regime d_{SDR} was calculated according to equation 2.28 (figure 5.23 right).

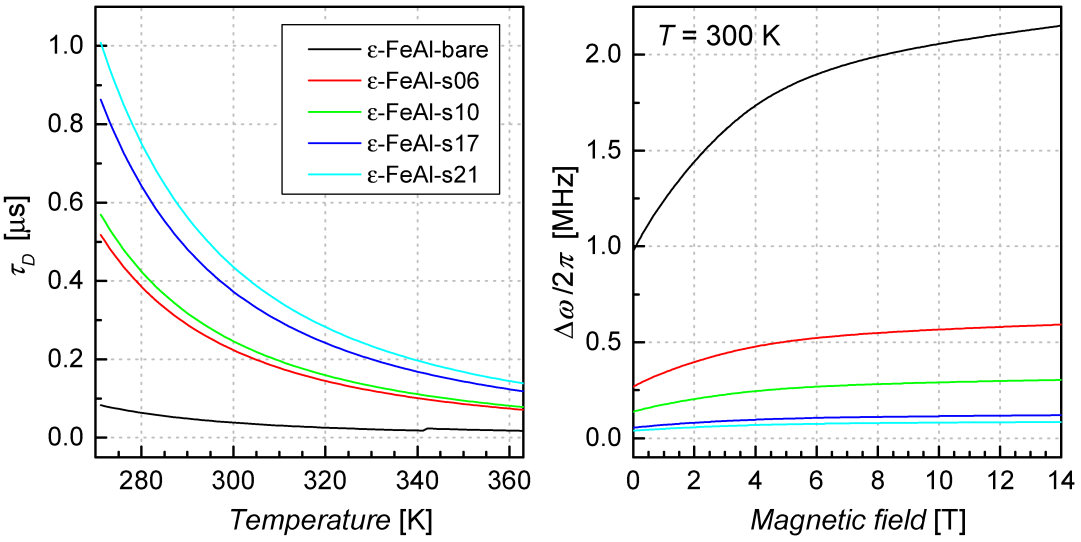

Figure 5.22: The diffusion correlation time τ_D as a function of temperature (left) calculated for median diameters of coated particles d_0 using relation 2.19, and the Larmor frequency shift $\Delta\omega/2\pi$ at the equator of the particle from relations 2.21 and 2.20 as a function of magnetic field at 300 K (right).

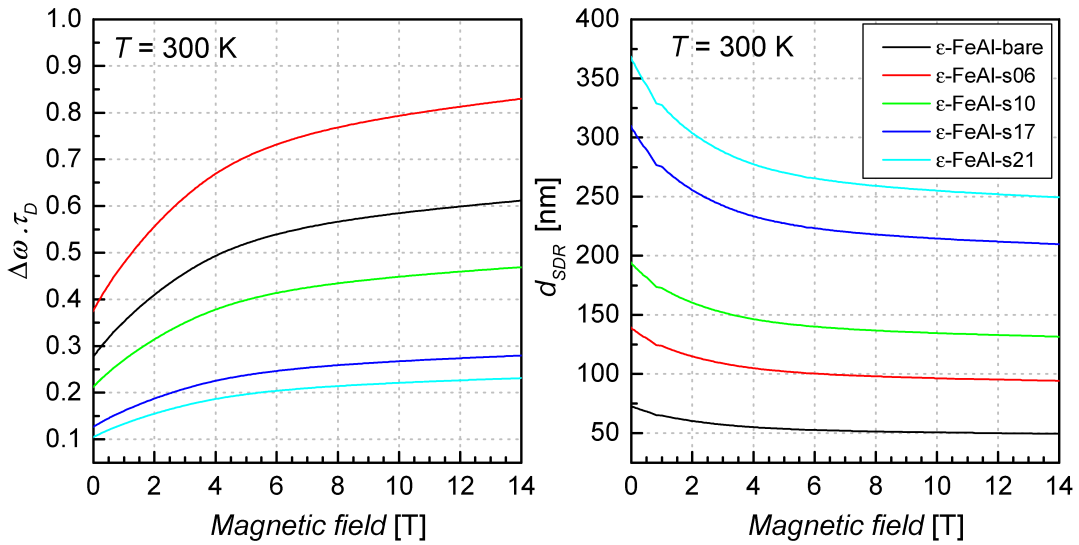

Figure 5.23: Graphical representation of the Redfield condition $\Delta\omega < \frac{1}{\tau_D}$, i.e. $\Delta\omega\tau_D < 1$ (left) and the critical diameter of transition from MAR to SDR d_{SDR} (right), both of them as a function of the magnetic field at 300 K.

Let us now compare the experimental data with the prediction of MAR theory:

- **Dependence of r_2 on the distance from the magnetic core of the particle.** Owing to the rescaling of the Larmor frequency shift by r_c^3/R^3, the relation 2.24 implies the proportionality of r_2 to the size of the magnetic core d_c as

$$r_{2,\mathrm{MAR}} \propto (d_c + 2l)^2(\Delta\omega)^2 \propto \frac{(d_c + 2l)^2 d_c^6}{(d_c + 2l)^6} = \frac{d_c^2}{(1 + \frac{2l}{d_c})^4}. \qquad (5.2)$$

If we consider that a fraction of water molecules may be quasistatic, the Static dephasing regime (SDR) would be of relevance, with the proportionality

$$r_{2,\mathrm{SDR}} \propto \Delta\omega \propto \frac{d_c^3}{(d_c+2l)^3} = \frac{1}{(1+\frac{2l}{d_c})^3}. \tag{5.3}$$

Two representative plots of dependence of experimental r_2 relaxivity and the theoretical one for MAR and SDR in coherence with the proportionalities 5.2 and 5.3 obtained by rescaling on relaxivity of bare particles are shown in figure 5.24. The Partial refocusing model (PRM) predicts for the $\tau_{CP} \sim 1\,\mathrm{ms}$ used in our experiment the same values after rescaling as SDR. Apparently, the predicted relaxivity decreases rapidly with the increasing distance from the magnetic particle, while the experimental decrease was virtually linear. This result indicates that another mechanism which enhances the transversal relaxivity might be involved. Possible explanation can be suggested based on water molecules bound to the silica coating, i.e. molecules either present inside the pores of silica or physisorbed to the silica surface, whose exchange with molecules in bulk water will be governed by a different dependence on temperature than the self-diffusion of water. Alternatively, the thermally activated exchange of $^1H^+$ between silanol groups (Si – OH) on the silica surface and water molecules should be considered. The silanol groups participate in acidobasic equilibrium with water described by the chemical equation $\mathrm{Si-OH} + \mathrm{H_2O} \rightleftarrows \mathrm{Si-O^-} + \mathrm{H_3O^+}$.

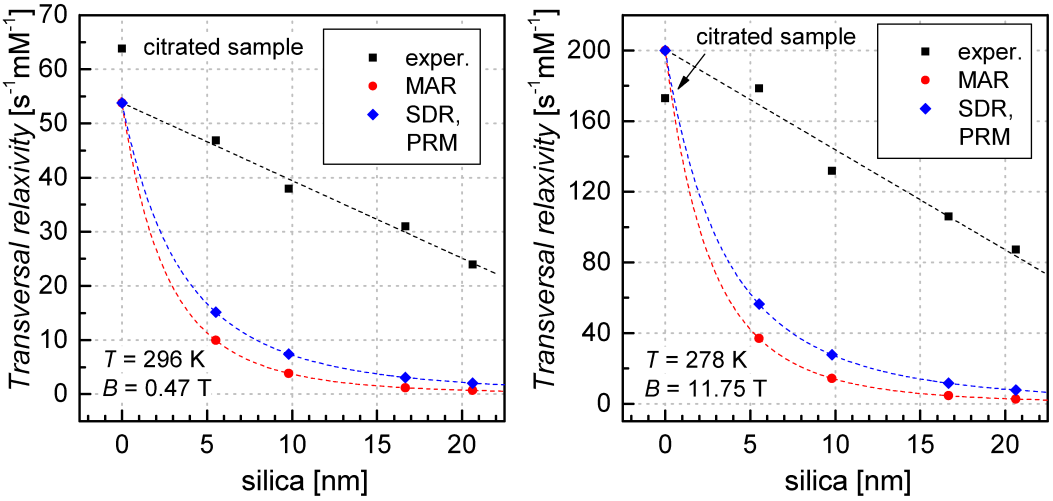

Figure 5.24: Dependence of r_2 relaxivity on the thickness of silica coating; plots for 23 °C and 0.47 T (left), 5 °C and 11.75 T (right). Linear regression was employed to extrapolate from experimental points (black) for nanoparticles encapsulated in silica to the presumed relaxivity of bare nanoparticles used for recalculation of theoretical points (red). There is a considerable difference between the theoretical dependence 5.2 in the MAR and experiment.

- **Dependence of r_2 on external magnetic field.** The only quantity in relation 2.24 dependent on magnetic field is $\Delta\omega \propto M$. The increase of magnetization with increasing magnetic field is depicted in figure 5.7 showing the hysteresis loops. Nevertheless, it is impossible to reach satisfactory concordance

by fitting the experimental data as proportional to M^2. As it was already mentioned in section 5.2.2, the data follow approximately the exponential rise to maximum as in equation $r_2 = \alpha - \beta e^{-\xi B}$. A representative comparison of the experimental data and their exponential fit with a curve showing the second power of the magnetization dependence on external magnetic field rescaled to experimental relaxivity at 0.47 T is depicted in figure 5.25 for sample ε-FeAl-s06 and figure 5.26 for sample ε-FeAl-s17 . Obviously, the predicted relaxivity increases steeper with the magnetic field than the measured one.

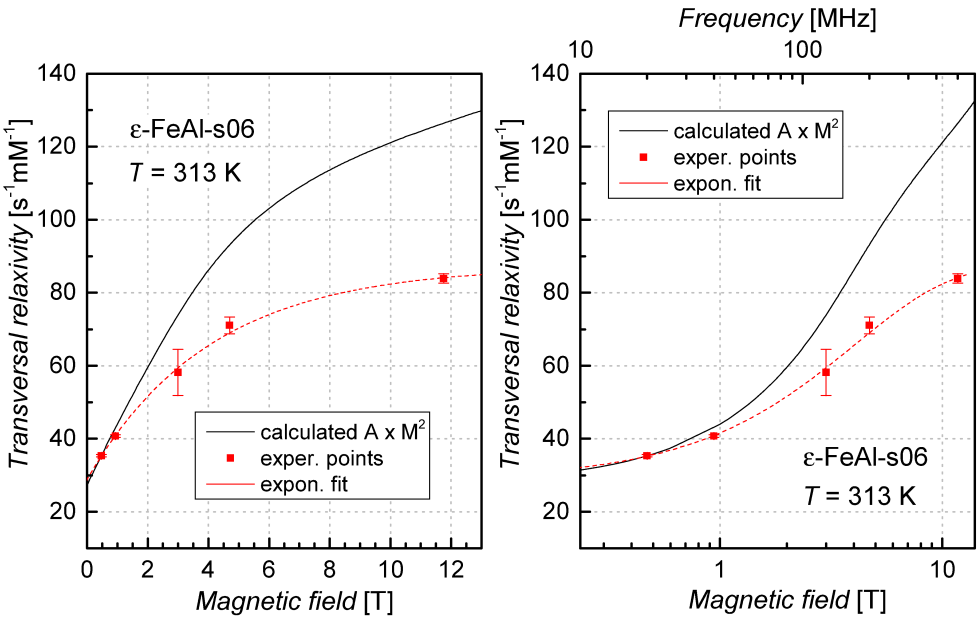

Figure 5.25: Dependence of r_2 relaxivity on the external magnetic field — comparison of experimental data fitted by exponential curve $r_2 = \alpha - \beta e^{-\xi B}$ with theoretical prediction $r_2 \propto M^2$. Demonstrated on the sample ε-FeAl-s06 at 313 K. The magnetic field dependence of M^2 at 300 K was rescaled to the experimental value of relaxivity at 0.47 T.

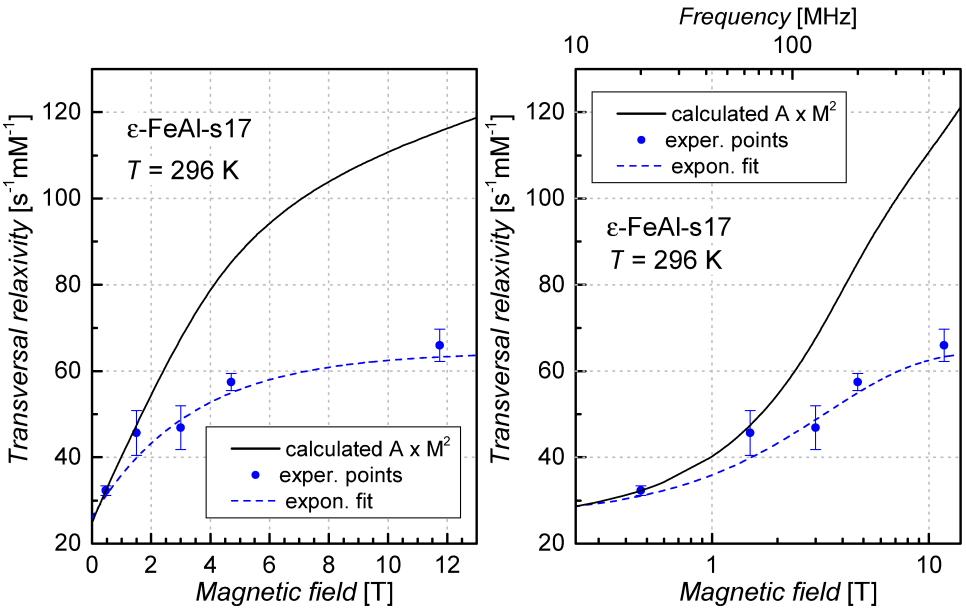

Figure 5.26: Dependence of r_2 relaxivity on the external magnetic field — comparison of experimental data fitted by exponential curve $r_2 = \alpha - \beta e^{-\xi B}$ with theoretical prediction $r_2 \propto M^2$. Demonstrated on the sample ε-FeAl-s17 at 296 K. The magnetic field dependence of M^2 was rescaled to the experimental value of relaxivity at 0.47 T.

- **Dependence of r_2 on temperature.** Multiple quantities in relation 2.24 depend on temperature. The self-diffusion coefficient follows approximately the Arrhenius law in the examined range of temperatures, the magnetization of particles decreases with increasing temperature as depicted in figure 5.10 (can be used for other magnetic fields than 0.5 T after rescaling). The increase in molar volume ν_{mat} of ε-$Fe_{1.77}Al_{0.23}O_3$ with temperature can be neglected being a few orders of magnitude smaller than other contributions. It is also probable that more than one heat-activated process is present — not only the diffusion of water in the vicinity of the particle, but also exchange of water molecules in the pores and surface layer of the silica coating.

  In principle, it is possible to fit the data by relation considering the temperature dependence of both magnetization and self-diffusion coefficient $r_2(T) = A + CM^2(T)\exp(E_a/RT)$ with $M(T) = \alpha - \beta T, \alpha = (50\,740 \pm 10)\,\text{A.m}^{-1}$, $\beta = (112.7 \pm 0.4)\text{A.m}^{-1}.\text{K}^{-1}$, obtained by linear fit of volume magnetization recalculated from data in figure 5.10. However, the interpretation of parameters obtained from the fit is precarious because of the unknown contribution of the dissolving silica coating at higher temperatures. Therefore, the fits considering the influence of magnetization decrease are introduced into graphs 5.15 – 5.18 rather to provide guidelines for the eye. Nevertheless, even though the physical interpretation of the coefficients is troublesome, the temperature dependence can be qualitatively described by the MAR model.

5.2.5 Comparison to ε-Fe_2O_3 nanoparticles

The transversal relaxivity of examined samples was compared to previous results of the relaxivity of ε-Fe_2O_3 nanoparticles encapsulated in silica (for more details see ref. Kubíčková, 2015). Three samples of ε-Fe_2O_3 nanoparticles were available with thickness of silica coating 8(1), 12(1) and 19(1) nm. To be able to compare the respective relaxivities of these two sets of samples, the relaxivity recalculated to the iron content was plotted as a function of the thickness of silica coating for measurements meeting the same conditions; representative graphs are shown in figure 5.27. Surprisingly, the relaxivities of ε-Fe_2O_3 and ε-$Fe_{1.77}Al_{0.23}O_3$ are similar in magnitude. One might assume that standard uncertainties of the determined concentrations are rather high, considering the complicated nature of the samples (dilute suspensions of silica coated particles). However, the analytical procedures employed (the analysis in triplicates and the ICP-MS method) provide reliable results that should enable precise comparison of the concentrations and thus the relaxivities. Therefore, the results are not distorted by imprecise chemical analysis. The increase in relaxivity by almost 40 % was observed for particles with the thickness of silica coating lower than 10 nm, which may suggest that the influence of the magnitude of the particle magnetic moment becomes less significant at larger distance from the magnetic core of the particle. Nonetheless, our assumption that increase in magnetization of the particles by $\sim$ 30 % would lead to the appropriate increase in relaxivity by $\sim$ 70 % as predicted by the MAR theory (relation 2.24), was not confirmed. The fact that our assumption originated from the MAR theory, and that the enhancement of magnetization had no considerable effect on the relaxivity provide another reason to work towards improvement of theoretical models available at present. It is also possible that the influence of the structure of the silica coating is highly underestimated.

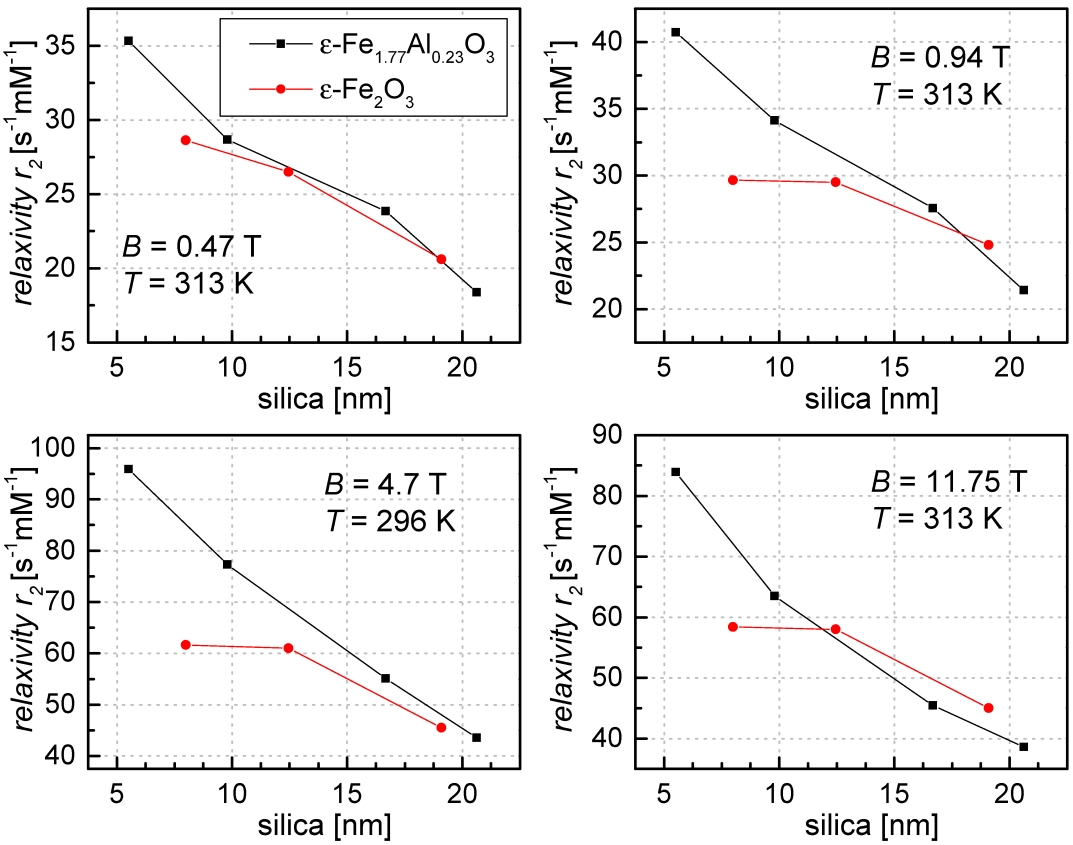

Figure 5.27: Graphical comparison of transversal relaxivity of ε-$Fe_{1.77}Al_{0.23}O_3$ and ε-Fe_2O_3 nanoparticles for representative temperatures and external magnetic fields.

5.3 Cytotoxicity

5.3.1 Viability of cells

The results of cytotoxic study of cell viability after exposure to nanoparticles coated in silica are summarised in table 5.8. Although the viability of cells is relatively high for all examined samples (over 78 %), the lower gain for samples with greater thickness of silica coating suggests that the presence of silica either reduces the proliferation of cells or impairs their adhesion abilities. The dependence of the gain on the thickness of silica coating is depicted in figure 5.28. Linear regression of the data indicates the average decrease in cell gain $\sim 3\,\%$ per 1 nm of silica coating.

Table 5.8: Comparison of the viability and gain of cells incubated with silica coated samples of nanoparticles

Sample	**Viability [%]**	**Gain [%]**
ε-FeAl-s21	85	47
ε-FeAl-s17	92	43
ε-FeAl-s10	91	74
ε-FeAl-s06	78	84
Negative control	90	100

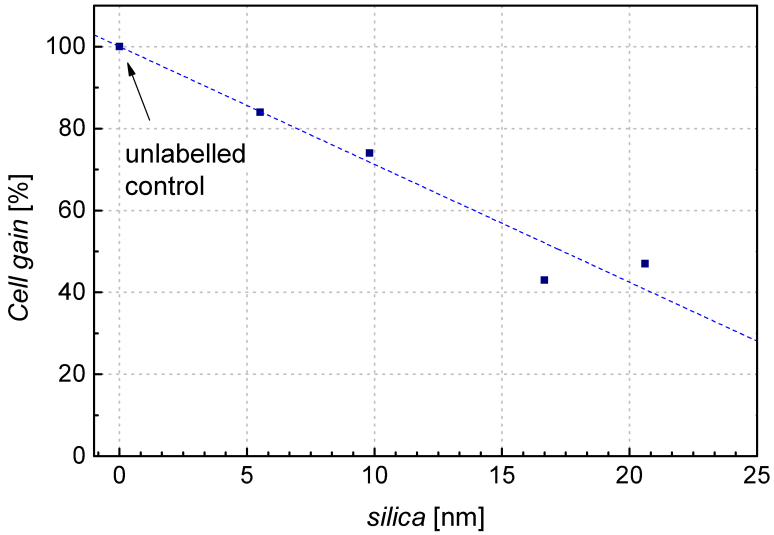

Figure 5.28: Dependence of the cell gain on the thickness of the shell for silica coated ε-$Fe_{1.77}Al_{0.23}O_3$ nanoparticles. The linear regression with fixed intercept at gain = 100 % was added to visualise the trend, yielding the average decrease in gain ∼ 3 % per 1 nm of silica coating.

To verify the trend in viability, the level of bioluminescence of luciferase expressing cells incubated with nanoparticles was measured after addition of luciferin to the medium. Due to the lack of cells available for experiments, only three samples (ε-FeAl-s17, ε-FeAl-s10 and ε-FeAl-s06) were examined. Figure 5.29 shows Petri dishes containing 100 000 labelled and control cells. Lower signal from samples containing labelled cells may correspond to lower viability; however, possible quenching of the bioluminiscence by the iron-containing nanoparticles cannot be excluded.

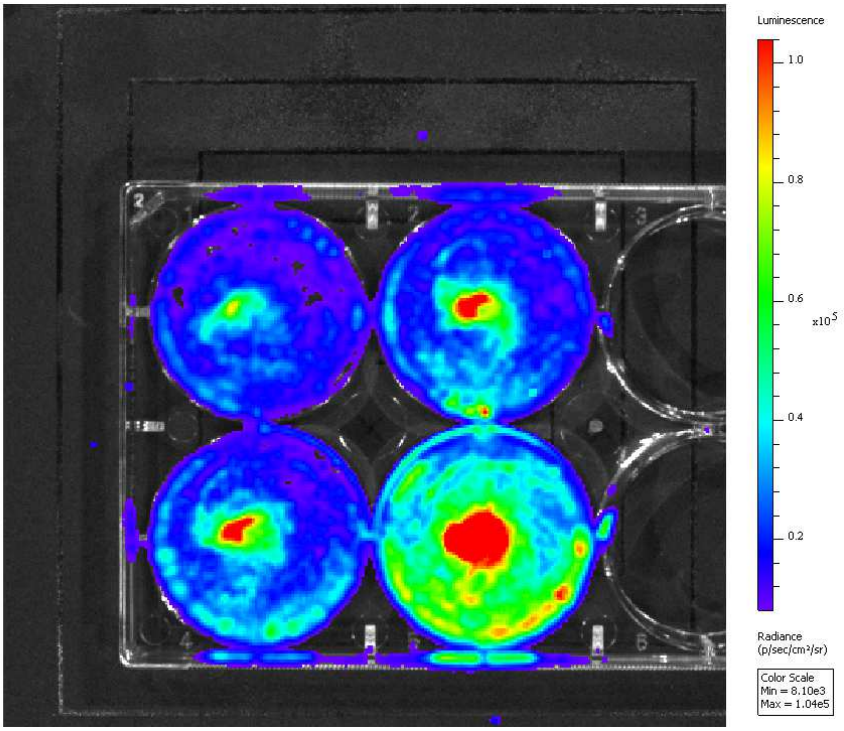

Figure 5.29: Bioluminiscence of cells labelled by examined nanoparticles. Petri dishes containing 100 000 cells labelled by 0.2 mM suspension of ε-FeAl-s17 (upper left), ε-FeAl-s10 (upper right), ε-FeAl-s06 (bottom left); a non-labelled control is depicted on the bottom right.

Conclusion

The transversal relaxivity of ε-$Fe_{2-x}Al_xO_3$ nanoparticles encapsulated in silica was thoroughly investigated by means of nuclear magnetic resonance with regard to the potential application as contrast agents in magnetic resonance imaging. In comparison to ε-Fe_2O_3 nanoparticles, this material prepared by substituting aluminium atoms for a fraction of iron atoms in ε-Fe_2O_3 was expected to exhibit higher magnetization and thus higher relaxivity.

The nanoparticles were synthesised by impregnation of mesoporous silica template with $Fe(NO_3)_3$ and $Al(NO_3)_3$ and coated by amorphous silica ($SiO_x(OH)_y$); one of the samples was stabilized by citrate. The chemical composition of bare particles of $Fe_{2-x}Al_xO_3$ was determined from XRF spectra to be $2-x = 1.77(1)$ of Fe and $x = 0.23(1)$ of Al; this result was used in all calculations regarding the relaxivity. XRPD analysis confirmed the same structure as ε-Fe_2O_3 — orthorhombic crystal system with $Pna2_1$ space group and lattice parameters $a = 5.0757(4)$ Å, $b = 8.7444(7)$ Å and $c = 9.4243(6)$ Å, the volume per formula unit $\sim 52.286(6)$ Å^3 (bare sample). Hyperfine parameters of iron sites were obtained by Mössbauer spectroscopy, which also showed that Al atoms occupy preferably tetrahedral sites in the crystal lattice. The content of aluminium was deduced from the intensity of lines in the Mössbauer spectrum to be $x = 0.24(1)$, confirming thus the composition obtained by XRF. For samples coated with silica, the size of magnetic cores of the particles, the size of coated particles including the clusters and the thickness of silica coating were determined by means of TEM image analysis.The size of magnetic cores (i.e. bare particles) was $\sim$ 21 nm, the thickness of silica coating $\sim 6, 10, 17$ and 21 nm. The stability of aqueous suspensions was confirmed by DLS.Magnetization of the ε-$Fe_{2-x}Al_xO_3$ nanoparticles increased by $\sim$ 30 % when compared to ε-Fe_2O_3, confirming thus our assumption about the influence of Al. ZFC/FC curves indicate that magnetic transitions characteristic to ε-Fe_2O_3 are suppressed by the substitution. The magnetization evinced an approximately linear decrease with temperature in the temperature range examined in our relaxometric study.

The transversal relaxivity r_2 was measured on suspensions of four samples encapsulated in silica and one stabilized by citrate. Considering the size and magnetic moment of the nanoparticles, the theoretical model describing the relaxivity is the motional averaging regime (MAR) yielding the relation 2.24. Magnetic field dependence followed approximately the exponential rise to maximum, for which the MAR model is not applicable. The different slope of relaxivity of the citrated sample in comparison to samples coated with silica suggests different mechanism of interaction of ^{1}H with the coating material. The temperature dependence of relaxivity of samples coated with silica demonstrated a significant deviation from a simple model based on the Arrhenius behaviour of water self-diffusion, which resulted in higher values of relaxivity than predicted by this simple model. Based on measurements during cooling after preceding heating, it was ascertained that the increase in relaxivity is irreversible; from subsequent examination by TEM and DLS, dissolution of silica coating was evidenced. The experimentally found linear decrease of relaxivity with increasing thickness of the silica coating (i.e. the respective shift in Larmor frequency of ^{1}H at the surface of the nanoparticle) is also

in contrast with the prediction of the MAR model. Our results indicate that another mechanism which enhances the transversal relaxivity might be involved. Possible explanation can be suggested based on water molecules bound to the silica coating, i.e. molecules either present inside the pores of silica or physisorbed to the silica surface. Nevertheless, the curve of the temperature dependence can be qualitatively described by MAR relation with regard to the linear dependence of magnetization on temperature, even though the physical interpretation of fitting parameters is not so straightforward due to the unknown contribution of the gradual dissolution of the silica coating. The relaxivity of examined samples was also compared to the relaxivity of ε-Fe_2O_3 nanoparticles from previous study; the increase by almost 40 % for particles coated with silica thickness lower than 10 nm was found, while there was no considerable difference in relaxivity for thicker coatings. Consequently, the magnitude of the increase did not meet our expectation and was in contradiction to the prediction of MAR (increase in magnetization by $\sim$ 30 % was supposed to enhance relaxivity by $\sim$ 70 % for any thickness of silica coating).

The transversal relaxivity of the examined samples is comparable to or exceeds commercial superparamagnetic iron oxide nanoparticle contrast agents (SPIOs and USPIOs) or those under clinical investigation (Laurent et al., 2008), whose relaxivity ranges between roughly 20 and 200 $s^{-1}.mM^{-1}$ per Fe at 1.5 T and 37 °C.

The study on cytotoxicity of examined nanoparticles revealed that the thickness of silica coating (probably through the size of coated particles) either affects the proliferation of cells or impairs their adherent abilities, reducing the gain of cells by $\sim$ 3 % per each nm of silica thickness when compared to unlabelled control. Despite that, the level of cytotoxicity is very low suggesting that the follow-up use of ε-$Fe_{2-x}Al_xO_3$ nanoparticles even with small thickness of silica coating for *in vivo* studies is safe.

The uniqueness of our results consists in providing experimental data on transversal relaxivity, especially its dependence on external magnetic field, which is difficult to obtain since it is impossible to employ field cycling methods and using various instruments is lengthy. As a consequence, mostly calculated r_2 are presented in literature while experimental data remain rare. Moreover, our results point out the limited validity of theoretical models available at present and call for their improvement. For this reason, the data will be published with dispatch.

Further investigations on transversal relaxivity with prospects for extension of present theoretical models and checking the limits of their validity, together with *in vivo* experiments in laboratory animals in collaboration with the Institute for Clinical and Experimental Medicine in Prague shall be the matter of future studies.

Bibliography

Eric T. Ahrens and Jeff W. M. Bulte. Tracking immune cells in vivo using magnetic resonance imaging. *Nature reviews. Immunology*, 13(10):755–63, 2013. ISSN 1474-1741. doi: 10.1038/nri3531. URL http://dx.doi.org/10.1038/nri3531.

Xavier Batlle and Amílcar Labarta. Finite-size effects in fine particles: magnetic and transport properties. *Journal of Physics D: Applied Physics*, 35(35):15–42, mar 2002. ISSN 0022-3727. doi: 10.1088/0022-3727/35/6/201. URL http://iopscience.iop.org/0022-3727/35/6/201.

Felix Bloch. Nuclear induction. *Physical Review*, 70(7-8):460–474, oct 1946. ISSN 0031899X. doi: 10.1103/PhysRev.70.460. URL http://link.aps.org/doi/10.1103/PhysRev.70.460.

F. Bødker, S. Mørup, and S. Linderoth. Surface effects in metallic iron nanoparticles. *Physical Review Letters*, 72(2):282–285, jan 1994. ISSN 00319007. doi: 10.1103/PhysRevLett.72.282. URL http://link.aps.org/doi/10.1103/PhysRevLett.72.282.

Petr Brázda, Jaroslav Kohout, Petr Bezdička, and Tomáš Kmječ. α-Fe2O3 versus β-Fe2O3 : Controlling the Phase of the Transformation Product of ϵ-Fe2O3 in the Fe2O3/SiO2 System. *Crystal Growth & Design*, 14(3):1039–1046, 2014. ISSN 1528-7483. doi: 10.1021/cg4015114. URL http://dx.doi.org/10.1021/cg4015114.

Robert W. Brown, Yu-Chung N. Cheng, E. Mark Haacke, Michael R. Thompson, and Ramesh Venkatesan, editors. *Magnetic Resonance Imaging: Physical Principles and Sequence Design*. John Wiley & Sons Ltd, Chichester, UK, 2. edition, apr 2014. ISBN 9781118633953. doi: 10.1002/9781118633953. URL http://doi.wiley.com/10.1002/9781118633953.

H. Y. Carr and E. M. Purcell. Effects of diffusion on free precession in nuclear magnetic resonance experiments. *Physical Review*, 94(3):630–638, 1954. ISSN 0031899X. doi: 10.1103/PhysRev.94.630. URL https://journals.aps.org/pr/abstract/10.1103/PhysRev.94.630.

Matthew R. J. Carroll, Robert C. Woodward, Michael J. House, Wey Yang Teoh, Rose Amal, Tracey L. Hanley, and Timothy G. St Pierre. Experimental validation of proton transverse relaxivity models for superparamagnetic nanoparticle MRI contrast agents. *Nanotechnology*, 21(3):035103, 2010. ISSN 0957-4484. doi: 10.1088/0957-4484/21/3/035103. URL http://iopscience.iop.org/article/10.1088/0957-4484/21/3/035103/meta.

J. M. D. Coey. Noncollinear spin arrangement in ultrafine ferrimagnetic crystallites. *Physical Review Letters*, 27(17):1140–1142, 1971. URL https://journals.aps.org/prl/abstract/10.1103/PhysRevLett.27.1140.

J. S. D'Arrigo. Screening of membrane surface charges by divalent cations: an atomic representation. *The American journal of physiology*, 235(3):C109–17,

sep 1978. ISSN 0002-9513. URL http://www.ncbi.nlm.nih.gov/pubmed/696813.

E. Delahaye, V. Escax, N. El Hassan, A. Davidson, R. Aquino, V. Dupuis, R. Perzynski, and Y. L. Raikher. "Nanocasting": using SBA-15 silicas as hard templates to obtain ultrasmall monodispersed γ-Fe_2O_3 nanoparticles. *Journal of Physical Chemistry B*, 110(51):26001–26011, 2006. ISSN 15206106. doi: 10.1021/jp0647075. URL http://pubs.acs.org.ezproxy.is.cuni.cz/doi/abs/10.1021/jp0647075.

J. L. Dormann, D. Fiorani, and E. Tronc. Magnetic relaxation in fine-particle systems. In *Advances in Chemical Physics*, volume 98, pages 282–494. John Wiley & Sons, Ltd., 1997. ISBN 047116285X. doi: 10.1002/9780470141571.ch4. URL http://doi.wiley.com/10.1002/9780470141571.ch4.

Frédéric Dumestre, Bruno Chaudret, Catherine Amiens, Philippe Renaud, and Peter Fejes. Superlattices of Iron Nanocubes Synthesized from $Fe[N(SiMe_3)_2]_2$. *Science*, 303(5659):821–823, 2004. doi: 10.1126/science.1092641. URL http://science.sciencemag.org/content/303/5659/821.

E. Fabryova, D. Jirak, P. Girman, K. Zacharovova, A. Galisova, F. Saudek, and J. Kriz. Effect of mesenchymal stem cells on the vascularization of the artificial site for islet transplantation in rats. In *Transplantation Proceedings*, volume 46, pages 1963–1966, jul 2014. ISBN 0041-1345\r1873-2623. doi: 10.1016/j.transproceed.2014.05.074. URL http://linkinghub.elsevier.com/retrieve/pii/S0041134514004229.

Claus Feldmann and Hans Otto Jungk. Polyol-mediated preparation of nanoscale oxide particles. *Angewandte Chemie - International Edition*, 40(2):359–362, jan 2001. ISSN 14337851. doi: 10.1002/1521-3773(20010119)40:2<359::AID-ANIE359>3.0.CO;2-B. URL http://dx.doi.org/10.1002/1521-3773(20010119)40:2<359::AID-ANIE359>3.0.CO;2-B.

M. Gich, C. Frontera, A. Roig, E. Molins, J. Fontcuberta, N. Bellido, Ch. Simon, and C. Fleta. Magnetoelectric Coupling in ε-Fe_2O_3 Nanoparticles. *Nanotechnology*, 687:17, 2006a. doi: 10.1088/0957-4484/17/3/012. URL http://arxiv.org/abs/cond-mat/0509104.

M. Gich, C. Frontera, A. Roig, E. Taboada, E. Molins, H. R. Rechenberg, J. D. Ardisson, W. A. A. Macedo, C. Ritter, V. Hardy, J. Sort, V. Skumryev, and J. Nogues. High and low-temperature crystal and magnetic structures of ε-Fe_2O_3 and their correlation to its magnetic properties. *Chemistry of Materials*, 18:3889–3897, 2006b. ISSN 08974756. doi: 10.1021/cm0609931. URL http://arxiv.org/abs/cond-mat/0604677.

M. Gich, J. Gazquez, A. Roig, A. Crespi, J. Fontcuberta, J. C. Idrobo, S. J. Pennycook, M. Varela, and V. Skumryev. Epitaxial stabilization of ε-Fe_2O_3 (001) thin films on $SrTiO_3$ (111). *Applied Physics Letters*, 96(11):112508, 2010. ISSN 00036951. doi: 10.1063/1.3360217. URL http://link.aip.org/link/APPLAB/v96/i11/p112508/s1{&}Agg=doi.

Pierre Gillis, Francis Moiny, and Rodney A. Brooks. On T_2-shortening by strongly magnetized spheres: A partial refocusing model. *Magnetic Resonance in Medicine*, 47(2):257–263, 2002. ISSN 07403194. doi: 10.1002/mrm.10059. URL http://onlinelibrary.wiley.com/doi/10.1002/mrm.10059/full.

H. Gleiter. Nanocrystalline materials. *Progress in Materials Science*, 33(4):223–315, 1989. ISSN 00796425. doi: 10.1016/0079-6425(89)90001-7. URL http://www.sciencedirect.com/science/article/pii/0079642589900017.

Y. Gossuin, T. Orlando, M. Basini, D. Henrard, A. Lascialfari, C. Mattea, S. Stapf, and Q. L. Vuong. NMR relaxation induced by iron oxide particles: testing theoretical models. *Nanotechnology*, 27(15):155706, 2016. ISSN 0957-4484. doi: 10.1088/0957-4484/27/15/155706. URL http://stacks.iop.org/0957-4484/27/i=15/a=155706?key=crossref.8976f1ac45ff03665d5bb310f66e68f1.

Ajay Kumar Gupta and Mona Gupta. Synthesis and surface engineering of iron oxide nanoparticles for biomedical applications. *Biomaterials*, 26(18):3995–4021, 2005. ISSN 01429612. doi: 10.1016/j.biomaterials.2004.10.012. URL http://www.sciencedirect.com/science/article/pii/S0142961204009317.

U. Herr, J. Jing, R. Birringer, U. Gonser, and H. Gleiter. Investigation of nanocrystalline iron materials by Mössbauer spectroscopy. *Applied Physics Letters*, 50(8):472–474, feb 1987. ISSN 0003-6951. doi: 10.1063/1.98177. URL http://aip.scitation.org/doi/10.1063/1.98177.

Manfred Holz, Stefan R. Heil, and Antonio Sacco. Temperature-dependent self-diffusion coefficients of water and six selected molecular liquids for calibration in accurate ^{1}H NMR PFG measurements. *Physical Chemistry Chemical Physics*, 2(20):4740–4742, 2000. ISSN 14639076. doi: 10.1039/b005319h. URL http://xlink.rsc.org/?DOI=b005319h.

Dale L. Huber. Synthesis, properties, and applications of iron nanoparticles. *Small*, 1(5):482–501, may 2005. ISSN 16136810. doi: 10.1002/smll.200500006. URL http://doi.wiley.com/10.1002/smll.200500006.

Bashar Issa, Ihab M. Obaidat, Borhan A. Albiss, and Yousef Haik. Magnetic nanoparticles: Surface effects and properties related to biomedicine applications. *International Journal of Molecular Sciences*, 14(11):21266–21305, oct 2013. ISSN 16616596. doi: 10.3390/ijms141121266. URL http://www.ncbi.nlm.nih.gov/pubmed/24232575.

J. Jin, S. Ohkoshi, and K. Hashimoto. Giant Coercive Field of Nanometer- Sized Iron Oxide. *Advanced Materials*, 16(1):48–51, 2004. ISSN 0935-9648. doi: 10.1002/adma.200305297. URL http://doi.wiley.com/10.1002/adma.200305297.

Tomonori Kanda, Toshio Fukusato, Megumi Matsuda, Keiko Toyoda, Hiroshi Oba, Jun'ichi Kotoku, Takahiro Haruyama, Kazuhiro Kitajima, and Shigeru Furui. Gadolinium-based Contrast Agent Accumulates in the Brain Even in Subjects without Severe Renal Dysfunction: Evaluation of Autopsy Brain Specimens with Inductively Coupled Plasma Mass Spectroscopy. *Radiology*, 276(1):228–32, jul

2015. ISSN 1527-1315. doi: 10.1148/radiol.2015142690. URL http://www.ncbi.nlm.nih.gov/pubmed/25942417.

D. K. Kim, Y. Zhang, W. Voit, K. V. Rao, and M. Muhammed. Synthesis and characterization of surfactant-coated superparamagnetic monodispersed iron oxide nanoparticles. *Journal of Magnetism and Magnetic Materials*, 225(1-2):30–36, 2001. ISSN 03048853. doi: 10.1016/S0304-8853(00)01224-5. URL http://www.sciencedirect.com/science/article/pii/S0304885300012245.

Do Kyung Kim, Maria Mikhaylova, Yu Zhang, and Mamoun Muhammed. Protective coating of superparamagnetic iron oxide nanoparticles. *Chemistry of Materials*, 15(8):1617–1627, 2003. ISSN 08974756. doi: 10.1021/cm021349j. URL http://pubs.acs.org/doi/abs/10.1021/cm021349j.

L. B. Kiss, J. Söderlund, G. A. Niklasson, and C. G. Granqvist. New approach to the origin of lognormal size distributions of nanoparticles. *Nanotechnology*, 25(1):25–28, mar 1999. ISSN 0957-4484. doi: 10.1088/0957-4484/10/1/006. URL http://iopscience.iop.org/0957-4484/10/1/006.

R.H Kodama. Magnetic nanoparticles. *Journal of Magnetism and Magnetic Materials*, 200(1):359–372, 1999. ISSN 03048853. doi: 10.1016/S0304-8853(99)00347-9. URL http://www.sciencedirect.com/science/article/pii/S0304885399003479.

Jaroslav Kohout, Petr Brázda, Karel Závěta, Denisa Kubániová, Tomáš Kmječ, Lenka Kubíčková, Mariana Klementová, Eva Šantavá, and Adriana Lančok. The magnetic transition in ε-Fe_2O_3 nanoparticles: Magnetic properties and hyperfine interactions from Mössbauer spectroscopy. *Journal of Applied Physics*, 117(17):17D505, 2015. ISSN 0021-8979. doi: 10.1063/1.4907610. URL http://scitation.aip.org/content/aip/journal/jap/117/17/10.1063/1.4907610.

Lenka Kubíčková. *Relaxivita magnetických nanočástic*. Bachelor thesis, Charles University, 2015. URL https://is.cuni.cz/webapps/zzp/detail/154765/.

Lenka Kubíčková, Jaroslav Kohout, Petr Brázda, Miroslav Veverka, Tomáš Kmječ, Denisa Kubániová, Petr Bezdička, Mariana Klementová, Eva Šantavá, and Karel Závěta. Impact of silica environment on hyperfine interactions in ε-Fe_2O_3 nanoparticles. *Hyperfine Interactions*, 237(1):1–10, 2016. doi: 10.1007/s10751-016-1356-8. URL http://rdcu.be/mFu2.

Serkan Kulaksiz and Michael Bau. Anthropogenic gadolinium as a microcontaminant in tap water used as drinking water in urban areas and megacities. *Applied Geochemistry*, 26(11):1877–1885, 2011. ISSN 08832927. doi: 10.1016/j.apgeochem.2011.06.011. URL http://www.sciencedirect.com/science/article/pii/S0883292711003222.

V. K. LaMer and R. H. Dinegar. Theory, production and mechanism of formation of monodispersed hydrosols. *Journal of the American Chemical Society*, 72(8):4847–4854, nov 1950. ISSN 00027863. doi: 10.1021/ja01167a001. URL http://pubs.acs.org/doi/abs/10.1021/ja01167a001.

Sophie Laurent, Delphine Forge, Marc Port, Alain Roch, Caroline Robic, Luce Vander Elst, and Robert N. Muller. Magnetic Iron Oxide Nanoparticles: Synthesis, Stabilization, Vectorization, Physicochemical Characterizations, and Biological Applications. *Chemical Reviews*, 108(6):2064–2110, 2008. ISSN 1520-6890. doi: 10.1021/cr068445e. URL http://pubs.acs.org/doi/abs/10.1021/cr068445e.

Michael Lévy, Florence Gazeau, Claire Wilhelm, Sophie Neveu, Martin Devaud, and Pierre Levitz. Revisiting MRI contrast properties of nanoparticles: Beyond the superparamagnetic regime. *Journal of Physical Chemistry C*, 117(29):15369–15374, jul 2013. ISSN 19327447. doi: 10.1021/jp404199f. URL http://pubs.acs.org/doi/abs/10.1021/jp404199f.

Angelique Louie. MRI biosensors: A short primer. *Journal of Magnetic Resonance Imaging*, 38(3):530–539, 2013. ISSN 10531807. doi: 10.1002/jmri.24298. URL https://www.ncbi.nlm.nih.gov/pubmed/23996662.

Libor Machala, Jiří Tuček, and Radek Zbořil. Polymorphous transformations of nanometric iron(III) oxide: A review. *Chemistry of Materials*, 23(14):3255–3272, 2011. ISSN 08974756. URL http://pubs.acs.org/doi/abs/10.1021/cm200397g.

B. Martínez, X. Obradors, L. L. Balcells, A. Rouanet, and C. Monty. Low Temperature Surface Spin-Glass Transition in γ-Fe_2O_3 Nanoparticles. *Physical Review Letters*, 80(1):181–184, jan 1998. ISSN 0031-9007. doi: 10.1103/PhysRevLett.80.181. URL http://link.aps.org/doi/10.1103/PhysRevLett.80.181.

Yuri Matsumoto and Alan Jasanoff. T_2 relaxation induced by clusters of superparamagnetic nanoparticles: Monte Carlo simulations. *Magnetic Resonance Imaging*, 26(7):994–998, 2008. ISSN 0730725X. doi: 10.1016/j.mri.2008.01.039. URL http://www.sciencedirect.com/science/article/pii/S0730725X08000945.

S. Meiboom and D. Gill. Modified spin-echo method for measuring nuclear relaxation times. *Review of Scientific Instruments*, 29(8):688–691, 1958. ISSN 00346748. doi: 10.1063/1.1716296. URL http://aip.scitation.org/doi/abs/10.1063/1.1716296.

Pierre Jean Nacher. Magnetic resonance imaging: From spin physics to medical diagnosis. In *The Spin: Poincare Seminar 2007*, volume 55, pages 159–193, Basel, 2009. Birkhäuser Basel. ISBN 9783764387983. doi: 10.1007/978-3-7643-8799-0-6. URL http://www.springerlink.com/index/10.1007/978-3-7643-8799-0{_}6.

Asuka Namai, Shunsuke Sakurai, Makoto Nakajima, Tohru Suemoto, Kazuyuki Matsumoto, Masahiro Goto, Shinya Sasaki, and Shin Ichi Ohkoshi. Synthesis of an electromagnetic wave absorber for high-speed wireless communication. *Journal of the American Chemical Society*, 131(3):1170–1173, 2009. ISSN 00027863. doi: 10.1021/ja807943v. URL http://pubs.acs.org/doi/abs/10.1021/ja807943v.

Asuka Namai, Marie Yoshikiyo, Kana Yamada, Shunsuke Sakurai, Takashi Goto, Takayuki Yoshida, Tatsuro Miyazaki, Makoto Nakajima, Tohru Suemoto, Hiroko Tokoro, and Shin-ichi Ohkoshi. Hard magnetic ferrite with a gigantic coercivity and high frequency millimetre wave rotation. *Nature Communications*, 3:1035, sep 2012. ISSN 2041-1723. doi: 10.1038/ncomms2038. URL http://www.nature.com/doifinder/10.1038/ncomms2038.

Andrew T. Ogielski. Dynamics of three-dimensional Ising spin glasses in thermal equilibrium. *Physical Review B*, 32(11):7384–7398, dec 1985. ISSN 01631829. doi: 10.1103/PhysRevB.32.7384. URL http://link.aps.org/doi/10.1103/PhysRevB.32.7384.

Shin-ichi Ohkoshi, Asuka Namai, Takehiro Yamaoka, Marie Yoshikiyo, Kenta Imoto, Tomomichi Nasu, Shizuka Anan, Yoshikazu Umeta, Kosuke Nakagawa, and Hiroko Tokoro. Mesoscopic bar magnet based on ε-Fe_2O_3 hard ferrite. *Scientific Reports*, 6(1):27212, jul 2016. ISSN 2045-2322. doi: 10.1038/srep27212. URL http://www.nature.com/articles/srep27212.

Shin-ichi Ohkoshi, Marie Yoshikiyo, Yoshikazu Umeta, Masaya Komine, Rei Fujiwara, Hiroko Tokoro, Kouji Chiba, Takeo Soejima, Asuka Namai, Yasuto Miyamoto, and Tomomichi Nasu. Phonon-Mode Calculation, Far- and Mid-Infrared, and Raman Spectra of an ε-$Ga_{0.5}Fe_{1.5}O_3$ Magnet. *The Journal of Physical Chemistry C*, 121(10):5812–5819, mar 2017. ISSN 1932-7447. doi: 10.1021/acs.jpcc.6b12694. URL http://pubs.acs.org/doi/abs/10.1021/acs.jpcc.6b12694.

Georgia C. Papaefthymiou. Nanoparticle magnetism. *Nano Today*, 4(5):438–447, 2009. ISSN 17480132. doi: 10.1016/j.nantod.2009.08.006. URL http://www.sciencedirect.com/science/article/pii/S1748013209000929.

O. Petracic. Superparamagnetic nanoparticle ensembles. *Superlattices and Microstructures*, 47(5):569–578, 2010. ISSN 07496036. doi: 10.1016/j.spmi.2010.01.009. URL https://arxiv.org/abs/0911.4031.

Mihaela Popovici, Marti Gich, Daniel Nižňanský, Anna Roig, Lluis Casas, Cecilia Savii, Elies Molins, Karel Závěta, Corina Enache, Jordi Sort, Sophie de Brion, Gerard Chouteau, and Josep Nogués. Optimized Synthesis of the Elusive ε-Fe_2O_3 Phase via Sol - Gel Chemistry. *Chemistry of Materials*, 25(16):5542–5548, 2004. doi: 10.1021/cm048628m. URL http://pubs.acs.org/doi/abs/10.1021/cm048628m.

Jerry L. Prince and Jonathan M. Links. *Medical Imaging Signals and Systems*. Pearson Prentice Hall, 2006. ISBN 0130653535, 9780130653536.

Yuri L. Raĭkher and Mark I. Shliomis. *The Effective Field Method in the Orientational Kinetics of Magnetic Fluids and Liquid Crystals*, volume 87, pages 595–751. John Wiley and Sons, Inc., 1994. ISBN 9780470141465. doi: 10.1002/9780470141465.ch8. URL http://dx.doi.org/10.1002/9780470141465.ch8.

M. Respaud, J. M. Broto, H. Rakoto, A. R. Fert, L. Thomas, B. Barbara, M. Verelst, E. Snoeck, P. Lecante, A. Mosset, J. Osuna, T. Ould Ely, C. Amiens, and B. Chaudret. Surface effects on the magnetic properties of ultrafine cobalt particles. *Physical Review B*, 57(5):2925–2935, feb 1998. ISSN 0163-1829. doi: 10.1103/PhysRevB.57.2925. URL http://link.aps.org/doi/10.1103/PhysRevB.57.2925.

Alain Roch, Robert N. Muller, and Pierre Gillis. Theory of proton relaxation induced by superparamagnetic particles. *The Journal of Chemical Physics*, 110(11):5403–5411, 1999. ISSN 0021-9606, 1089-7690. doi: 10.1063/1.478435. URL http://aip.scitation.org/doi/abs/10.1063/1.478435.

Alain Roch, Yves Gossuin, Robert N. Muller, and Pierre Gillis. Superparamagnetic colloid suspensions: Water magnetic relaxation and clustering. *Journal of Magnetism and Magnetic Materials*, 293(1):532–539, 2005. ISSN 03048853. doi: 10.1016/j.jmmm.2005.01.070. URL http://linkinghub.elsevier.com/retrieve/pii/S0304885305001290.

Juan Rodríguez-Carvajal. Recent developments for the program FULLPROF. *International Union of Crystallography Newsletter*, December 2(26):12–19, 2001. ISSN 1591-9552. URL https://www.ill.eu/sites/fullprof/php/reference.html.

T. Roisnel and J. Rodríquez-Carvajal. WinPLOTR: A Windows Tool for Powder Diffraction Pattern Analysis. *Materials Science Forum*, 378-381(January 2001):118–123, 2001. ISSN 1662-9752. doi: 10.4028/www.scientific.net/MSF.378-381.118. URL http://citeseerx.ist.psu.edu/viewdoc/summary?doi=10.1.1.561.2063.

Anne-Laure Rollet, Sophie Neveu, Patrice Porion, Vincent Dupuis, Nadine Cherrak, and Pierre Levitz. New approach for understanding experimental NMR relaxivity properties of magnetic nanoparticles: focus on cobalt ferrite. *Physical Chemistry Chemical Physics*, 18(48):32981–32991, 2016. ISSN 1463-9076. doi: 10.1039/C6CP06012A. URL http://xlink.rsc.org/?DOI=C6CP06012Ahttp://xlink.rsc.org/?DOI=C6CP06012A.

Shunsuke Sakurai, Jian Jin, Kazuhito Hashimoto, and Shin Ichi Ohkoshi. Reorientation Phenomenon in a Magnetic Phase of ε-Fe_2O_3 Nanocrystal. *Journal of the Physical Society of Japan*, 74(7):1946–1949, 2005. ISSN 00319015. doi: 10.1143/JPSJ.74.1946. URL http://journals.jps.jp/doi/abs/10.1143/JPSJ.74.1946.

Shunsuke Sakurai, Shiro Kuroki, Hiroko Tokoro, Kazuhito Hashimoto, and Shin-ichi Ohkoshi. Synthesis, Crystal Structure, and Magnetic Properties of ϵ-InxFe2–xO3 Nanorod-Shaped Magnets. *Advanced Functional Materials*, 17(14):2278–2282, sep 2007. ISSN 1616301X. doi: 10.1002/adfm.200600581. URL http://doi.wiley.com/10.1002/adfm.200600581.

Shunsuke Sakurai, Kotaro Tomita, Kazuhito Hashimoto, Hisashi Yashiro, and Shin-ichi Ohkoshi. Preparation of the Nanowire Form of ε-Fe_2O_3 Single Crystal and a Study of the Formation Process. *Journal of Physical Chemistry C*, 112(51):

20212–20216, dec 2008. ISSN 19327447. doi: 10.1021/jp806336f. URL http://pubs.acs.org/doi/abs/10.1021/jp806336f.

M. Sasaki, P. E. Jönsson, H. Takayama, and H. Mamiya. Aging and memory effects in superparamagnets and superspin glasses. *Physical Review B - Condensed Matter and Materials Physics*, 71(10):104405, mar 2005. ISSN 10980121. doi: 10.1103/PhysRevB.71.104405. URL http://link.aps.org/doi/10.1103/PhysRevB.71.104405.

Klaus D. Sattler, editor. *Handbook of nanophysics: Nanoparticles and Quantum Dots*. CRC Press, 2011a. ISBN 978-1-4200-7544-1.

Klaus D. Sattler, editor. *Handbook of Nanophysics: Nanomedicine and Nanorobotics*. CRC Press, 2011b. ISBN 9781420075465.

R. D. Shannon. Revised effective ionic radii and systematic studies of interatomic distances in halides and chalcogenides. *Acta Crystallographica Section A*, 32(5): 751–767, sep 1976. ISSN 16005724. doi: 10.1107/S0567739476001551. URL http://scripts.iucr.org/cgi-bin/paper?S0567739476001551.

S. Shtrikman and E.P. Wohlfarth. The theory of the Vogel-Fulcher law of spin glasses. *Physics Letters A*, 85(8-9):467–470, oct 1981. ISSN 03759601. doi: 10.1016/0375-9601(81)90441-2. URL http://linkinghub.elsevier.com/retrieve/pii/0375960181904412.

Ralph Skomski. Nanomagnetics. *Journal of Physics: Condensed Matter*, 15(20): R841, may 2003. ISSN 0953-8984. doi: 10.1088/0953-8984/15/20/202. URL http://stacks.iop.org/0953-8984/15/i=20/a=202?key=crossref.92b6b725d34a19ec7a83eebdf3a98e74http://iopscience.iop.org/0953-8984/15/20/202.

Charles P. Slichter. *Principles of magnetic resonance*. Springer-Verlag Berlin ; New York, 3rd enl. and updated ed. edition, 1990. ISBN 3540501576 0387501576.

Dimitri Stanicki, Luce Vander Elst, Robert N Muller, and Sophie Laurent. Synthesis and processing of magnetic nanoparticles. *Current Opinion in Chemical Engineering*, 8:7–14, 2015. ISSN 22113398. doi: 10.1016/j.coche.2015.01.003. URL http://www.sciencedirect.com/science/article/pii/S2211339815000040.

Werner Stöber, Arthur Fink, and Ernst Bohn. Controlled growth of monodisperse silica spheres in the micron size range. *Journal of Colloid and Interface Science*, 26(1):62–69, 1968. ISSN 00219797. doi: 10.1016/0021-9797(68)90272-5. URL http://www.sciencedirect.com/science/article/pii/0021979768902725.

Randall Toy, Lisa Bauer, Christopher Hoimes, Ketan B. Ghaghada, and Efstathios Karathanasis. Targeted Nanotechnology for Cancer Imaging. *Advanced Drug Delivery Reviews*, 76(2014):79–97, 2014. ISSN 0169409X. doi: 10.1016/j.addr.2014.08.002. URL http://linkinghub.elsevier.com/retrieve/pii/S0169409X14001677.

Yuan Chieh Tseng, Narcizo M. Souza-Neto, Daniel Haskel, Martí Gich, Carlos Frontera, Anna Roig, Michel Van Veenendaal, and Josep Nogués. Nonzero orbital moment in high coercivity ε-Fe_2O_3 and low-temperature collapse of the magnetocrystalline anisotropy. *Physical Review B - Condensed Matter and Materials Physics*, 79(9):1–6, 2009. ISSN 10980121. doi: 10.1103/PhysRevB.79.094404. URL https://journals.aps.org/prb/abstract/10.1103/PhysRevB.79.094404.

Chuqiao Tu, Elizabeth A. Osborne, and Angelique Y. Louie. Activatable T_1 and T_2 magnetic resonance imaging contrast agents. *Annals of Biomedical Engineering*, 39(4):1335–1348, 2011. ISSN 00906964. doi: 10.1007/s10439-011-0270-0. URL https://www.ncbi.nlm.nih.gov/pmc/articles/PMC3069332/.

Jiří Tuček, Radek Zbořil, Asuka Namai, and Shin-Ichi Ohkoshi. ε-Fe_2O_3: An advanced nanomaterial exhibiting giant coercive field, millimeter-wave ferromagnetic resonance, and magnetoelectric coupling. *Chemistry of Materials*, 22 (24):6483–6505, 2010. ISSN 08974756. doi: 10.1021/cm101967h. URL http://pubs.acs.org/doi/abs/10.1021/cm101967h.

Jiří Tuček, Libor Machala, Shigeaki Ono, Asuka Namai, Marie Yoshikiyo, Kenta Imoto, Hiroko Tokoro, Shin-ichi Ohkoshi, and Radek Zbořil. ζ-Fe_2O_3 – A new stable polymorph in iron(III) oxide family. *Scientific Reports*, 5(III):15091, oct 2015. ISSN 2045-2322. doi: 10.1038/srep15091. URL http://www.nature.com/articles/srep15091.

Quoc L. Vuong, Jean François Berret, Jérôme Fresnais, Yves Gossuin, and Olivier Sandre. A universal scaling law to predict the efficiency of magnetic nanoparticles as MRI T_2-contrast agents. *Advanced Healthcare Materials*, 1(4):502–512, 2012. URL http://onlinelibrary.wiley.com/doi/10.1002/adhm.201200078/ful.

Quoc Lam Vuong, Pierre Gillis, and Yves Gossuin. Monte Carlo simulation and theory of proton NMR transverse relaxation induced by aggregation of magnetic particles used as MRI contrast agents. *Journal of Magnetic Resonance*, 212(1): 139–148, 2011. ISSN 10907807. doi: 10.1016/j.jmr.2011.06.024. URL http://dx.doi.org/10.1016/j.jmr.2011.06.024.

Yan Xiao, Yi-Jie Wu, Wen-Jun Zhang, Xiao-Jing Li, and Feng-Kui Pei. Research Progress of Magnetic Resonance Imaging Contrast Agents. *Chinese Journal of Analytical Chemistry*, 39(5):757–764, 2011. ISSN 18722040. doi: 10.1016/S1872-2040(10)60438-0. URL http://dx.doi.org/10.1016/S1872-2040(10)60438-0.

Dmitriy A. Yablonskiy and E. Mark Haacke. Theory of NMR signal behavior in magnetically inhomogeneous tissues: The static dephasing regime. *Magnetic Resonance in Medicine*, 32(6):749–763, dec 1994. ISSN 15222594. doi: 10.1002/mrm.1910320610. URL http://doi.wiley.com/10.1002/mrm.1910320610.

Marie Yoshikiyo, Asuka Namai, Makoto Nakajima, Tohru Suemoto, and Shin Ichi Ohkoshi. Anomalous behavior of high-frequency zero-field ferromagnetic resonance in aluminum-substituted ε-Fe_2O_3. In *Journal of Applied Physics*, volume

111, pages 7–726, 2012. doi: 10.1063/1.3677763. URL http://dx.doi.org/10.1063/1.3677763.

Tomáš Žák and Yvonna Jirásková. CONFIT: Mössbauer spectra fitting program. *Surface and Interface Analysis*, 38:710–714, 2006. doi: 10.1002/sia2285. URL http://onlinelibrary.wiley.com/doi/10.1002/sia.2285/full.

Charlie Zender. Particle size distributions: Theory and application to aerosols, clouds, and soils. *Online: http://dust. ess. uci. edu/facts, Updated: Mon 30th Aug*, 2015. URL http://dust.ess.uci.edu/facts/psd/psd.pdf.

Dongyuan Zhao, Qisheng Huo, Jianglin Feng, Bradley F. Chmelka, and Galen D. Stucky. Nonionic triblock and star diblock copolymer and oligomeric sufactant syntheses of highly ordered, hydrothermally stable, mesoporous silica structures. *Journal of the American Chemical Society*, 120(24):6024–6036, 1998. ISSN 00027863. doi: 10.1021/ja974025i. URL http://pubs.acs.org/doi/abs/10.1021/ja974025i.

List of Figures

List of Tables

List of Abbreviations

AAS atomic absorption spectroscopy.

AFM antiferromagnetic.

CPMG Carr-Purcell-Meiboom-Gill.

DLS dynamic light scattering.

ELR echo limited regime.

FC field cooled.

FID free induction decay.

FIM ferrimagnetic.

FM ferromagnetic.

ICP-MS inductively coupled plasma mass spectrometry.

MAR motional averaging regime.

MNP magnetic nanoparticle.

MRI magnetic resonance imaging.

NMR nuclear magnetic resonance.

NMRD nucear magnetic relaxation dispersion.

NP nanoparticle.

P123 PEG-PPG-PEG triblock co-polymer consisting of poly(ethylene oxide) – PEO and poly(propylene oxide) – PPO.

PD proton density.

PRM partial refocusing model.

SDR static dephasing regime.

TE echo time.

TEM transmission electron microscopy.

TEOS tetraethoxysilane.

TR repetition time.

UHV ultra high vacuum.

XRF X-ray fluorescence spectroscopy.

XRPD X-ray powder diffraction.

ZFC zero-field cooled.